UNIVERSITY OF
LIVERPOOL

Spin correlations and orbital physics in vanadates

Thesis submitted in accordance with the requirements of
the University of Liverpool for the degree of Doctor in Philosophy by

Markos Skoulatos

Oliver Lodge Laboratory,
Department of Physics, University of Liverpool

March 2008

Στους γονείς μου Βασίλη και Νίκη,

στα αδέρφια μου Θόδωρο και Κατερίνα

και στη Βένια μου, με αγάπη!

Abstract

Magnetic model systems Li_2VOSiO_4, $Pb_2VO(PO_4)_2$ and $SrZnVO(PO_4)_2$ were studied using polarised neutron scattering. The vanadium $S = 1/2$ ions form two-dimensional square lattices, where the cross-bond exchange, J_2, along the diagonal can compete with the nearest-neighbour (NN) exchange, J_1, along the sides of the square. The magnetic ground state for all these compounds is a collinear antiferromagnet (CAF), i.e. ferromagnetic (FM) lines arranged in an antiferromagnetic (AF) way. This is in contrast to the more usual Néel antiferromagnet (NAF), characteristic of spin systems dominated by AF NN exchange. The ordered moment is reduced in all cases, especially for $Pb_2VO(PO_4)_2$ and $SrZnVO(PO_4)_2$, and at the same time a considerable diffuse background appears, due to quantum zero-point fluctuations. This quantum disordered state was also studied in the paramagnetic phase using polarised diffuse scattering techniques, as a way of extracting the magnetic exchanges in the absence of large single crystals. The $S(Q)$ measurements of powdered $Pb_2VO(PO_4)_2$ and $SrZnVO(PO_4)_2$ samples revealed a completely new area of the so-called $J_1 - J_2$ phase diagram, being the first materials with FM J_1 and AF J_2 interactions.

Single crystals of the transition metal oxides $GdVO_3$ and $LuVO_3$ were studied with neutrons and resonant x-rays. In this case, the vanadium lattice has an almost cubic symmetry, resulting in degenerate many-body orbital states that compete. A combination of the above techniques on $GdVO_3$ yielded a spin structure consisting of FM chains with AF order between them (C-type), while the orbitals were found to order with orientations staggered in all three directions (G-type). The orbital ordering x-ray energy spectra have been modeled with *ab initio* calculations. Spinwave dispersions were investigated in inelastic neutron studies of $LuVO_3$, which has both C- and G-spin (and orbital) phases at different temperatures. The exotic gapped C-spin phase is explained in terms of a recently developed theory with orbital fluctuations and an orbital Peierls effect.

Acknowledgements

First and foremost, I would like to especially thank my supervisor Jon Goff for giving me the opportunity to carry out this work with him. His continued support and guidance ranged from thermal physics tutorials to orbital and magnetic experiments throughout both my undergraduate as well as graduate degrees in Liverpool.

This work would not of course be possible without any samples to measure. Cristoph Geibel, Enrique Kaul and Ramesh Nath from the Max-Planck Institute for Chemical Physics of Solids in Dresden did an amazing job in discovering and growing huge quantities of new 2D frustrated magnetic systems. I should also thank L.D. Tung for the high-quality single crystals he provided. Mike Thomas, an extremely nice man, seemed to be around when strange physics questions came to my mind. Thank you for listening and explaining, as well as delivering beautiful lectures. My friends Christos and Eutyxia Touramanis are always there for advice and barbeques; I could always relax and get a little bit of Greece with them. Chris Lucas introduced me to experiments in large scale facilities, as well as went into the trouble of reading this work. I also thank Des McMorrow for the very useful comments and expert suggestions.

A variety of characters have been instrumental in the completion of all the neutron and x-ray experiments, and I would like to thank them all. In particular, my friend Amir Murani has always been trying to push my knowledge and make me think more critically. Thank you for your hospitality and a very cool weekend in the Alps too! I also thank Garry McIntyre for very carefully analysing the structural data of this work, even though towards the end I had illusions of seeing him everywhere! I am very grateful to have met Mechthild Enderle and wish to thank her for showing interest in our systems as well as explaining spin-wave theory. I would like to also thank everyone at XMaS, and particularly Laurence for being so nice and helpful, as well as Simon and Paul whom I respect. Thanks go to Yves Joly, Nic Shannon and G. Khaliullin, responsible for the theory input.

Keith Williams was the person that gave me the keys to the CMP bridge on the first day and I probably spoke the most with everyday. Thank you for many many things, including helping me to refret my guitar and also introducing me to the workshop. This brings us to my very good friend Peter Cooke, who has always something positive to say, and has supplied me with plenty of advices, knowledge and musical sounds! Special thanks go to everyone else at the workshop for welcoming me at all times. Sam Haq is responsible for, and even put his work aside in doing all the nice crystal structure pictures in this thesis. Jose Angel was one of the first people I met in the CMP bridge and explained to me magnetism theory, SQUID measurements and how to turn the board. Vamos snowboard man! Special thanks go to Peter Normile for explaining basic physics clearly to me, including interrupting an experiment in describing Bragg's law.

I take this opportunity to thank Giorgos Zesimopoulos who gave me my first experiences with measuring physical quantities and extracting meaningful results out of them. I also owe a lot to Kyriakos Stratakos, for opening up my horizons in thinking about problem solving; he was possibly the greatest thinker I have met.

Ben Fowler, Jon and Simon have been continuously helping me - particularly with computing - throughout the whole 3 years. Sometimes though, I was told to read the manual. I also thank the rest of the CMP students, Mick, Alex B., Ray, Dave (without him fixing the mighty micra I would have never been on time to work) and especially Andrea for turning my guitar into a beautiful piece of art! Craig, Alex G., Laura, Carl, Matt, Stefanos and Marina from the nuclear structure group were always up for a friendly chat. I particularly thank Dave Scraggo, the man, for sharing his ideas with me. We were writing up in the same time so had plenty of chances for after-midnight breaks in the lab.

I had the luck to be good friends with Ben Pietras, an amazing guy who I can always trust. I will never forget the laughs we had, especially in 10 Garrick street, and all the things and ideas communicated. Thanks to Richard too, for showing me a different aspect of life and being such a good friend. He has also helped me numerous times with computers. My welsh friend Danial, who looks more like a Greek, has sorted out so many practicalities of my everyday life and always gives the lesson of taking life as it comes. I would like to thank Paul for all the jamming sessions and interesting ideas, as well as Kosmas for relaxing evenings full of music. A special thank you goes to old friends Dave and Shahid, and I wish you all the best Julios! My stay in Liverpool has been made much more interesting and enjoyable by my friends Maria and Andry, they are people that care about me and I can always count on. Extra special thanks go to the Zebra 3 boys Kevin, Dave and John who kept me entertained at the Cavern and fully energised me with their music; they are definitely the best funky-rock pub band around! I would like to take this opportunity and sincerely thank my colleagues Kirrily, Katia and Klaus for being so supportive and showing understanding in my new environment. Werner Ch. and Maria helped me stand on my feet quickly; I could have never imagined such a warm welcome and company. I would also like to thank everyone else that I forgot, and there might be plenty.

This thesis and more importantly reality, would not exist without my family. There are no words to describe my feelings. My dad gave me the basis for all knowledge I acquired and my mum was so successful in growing all of us up, the most difficult task of life. Katerina, my "little" sister, is always helping and supporting me - without thinking about it - and makes sure I have the best time. My brother Theodore, who always tries new things out, has been there making things simple for me; I will always be learning a lot from you. During the last two years, my girl Trisevgeni has done so much for me and I feel so lucky to be with her. Thank you for your love and support and mainly for all of your efforts! Finally I thank I. Myron for showing the way...

Contents

Glossary

2DQHAF	-	2-Dimensional Quantum Heisenberg Antiferromagnet
ABS	-	Automatic Background Subtraction
AF	-	Antiferromagnet
ASF	-	Anomalous Scattering Factor
CAF	-	Collinear Antiferromagnet, see fig. 3.3(b)
CW	-	Curie - Weiss
DAFS	-	Diffraction Anomalous Fine Structure
DANES	-	Diffraction Anomalous Near-Edge Structure
DOS	-	Density of States
ESRF	-	European Synchrotron Radiation Facility
EXAFS	-	Extended X-Ray Absorption Fine Structure
FDM	-	Finite Difference Method
FM	-	Ferromagnet
GS	-	Ground State
HTSC	-	High-Temperature Superconductor
HTSE	-	High-Temperature Series Expansion
ILL	-	Institut Laue-Langevin
JT	-	Jahn-Teller
LDA	-	Local Density Approximation
LRO	-	Long Range Order
MFT	-	Mean-Field Theory
NAF	-	Néel Antiferromagnet
ND	-	Neutron Diffraction
NN	-	Nearest Neighbour
NNN	-	Next-Nearest Neighbour

NSF	-	Non-Spin-Flip
OO	-	Orbital Order
OVB	-	Orbital Valence Bond
PA	-	Polarisation Analysis
PG	-	Pyrolytic Graphite
RT	-	Room Temperature, which room?
RVB	-	Resonating Valence Bond
RXS	-	Resonant X-Ray Scattering
SF	-	Spin-Flip
SL	-	Spin Liquid
SO	-	Spin Order
TM	-	Transition Metal
TMO	-	Transition-Metal Oxide
VBC	-	Valence-Bond Crystal
XANES	-	X-Ray Absorption Near-Edge Structure
XAS	-	X-Ray Absorption Spectroscopy
XRD	-	X-Ray Diffraction

Chapter 1

Introduction

The fact that magnetite (Fe_3O_4) was already known in the Greek era as a peculiar mineral is indicative of the long history of transition metal compounds as useful and interesting materials. Early experiments on magnetism described by theories based on classical effects had only limited success. A full quantum mechanical treatment of the evolving problem is necessary, taking into account the electron's orbital wavefunctions. Since the discovery of high-temperature superconductivity in layered cuprates in 1986, particular emphasis has been drawn to transition metal oxides, as well as two-dimensional spin-half magnets. Manganites have also received special attention recently, because of their colossal magnetoresistance.

In many transition metal (TM) oxide crystals, the TM ions are surrounded by six oxygen ions, making octahedra. The perovskite ($CaTiO_3$) crystal structure, shown in figure 1.1(a), is very commonly found in such oxides. The TM ion M is placed, to a first approximation, equidistant from six oxygen ions. In this case, M is in a crystal field potential with cubic symmetry. High symmetries in nature, are often associated with highly degenerate wavefunctions. However, the system will often try to lift this degeneracy in order to minimise its energy. This may lead to many unexpected phenomena and, in particular, to frustration due to the competition between different mechanisms (quantified as energy terms in the

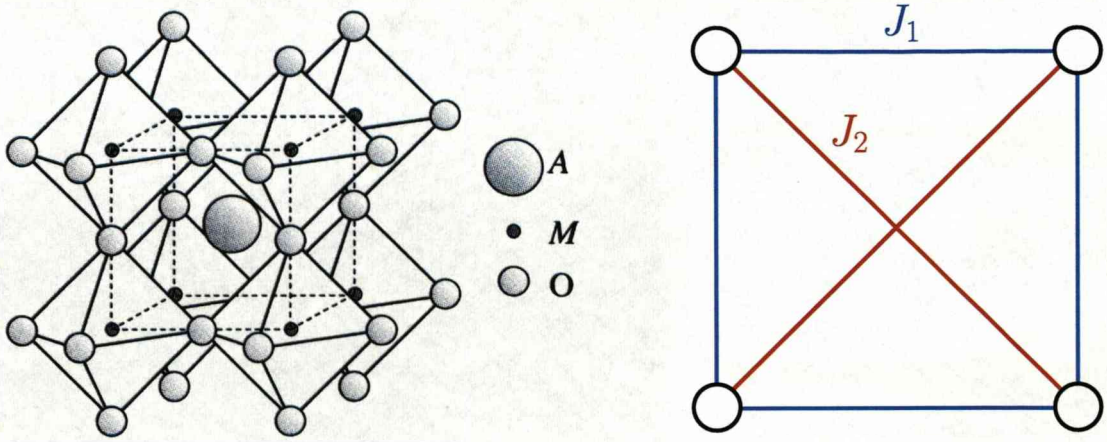

(a) (b)

Figure 1.1: Lattice examples in which degeneracy can lead to frustration. (a) Crystal structure of perovskite AMO_3, after [1]. The high cubic symmetry can lead to degeneracy in the orbital sector. (b) Model of a magnetic two-dimensional square lattice, where magnetic interactions J_1 and J_2 can compete. A large number of classical spin configurations with the same energy is possible.

system Hamiltonian $\mathscr{H}$).

In order to investigate fundamental properties of condensed matter systems and test theory, it is often helpful to design model systems. This enables scientists to separate physical parameters and try and address questions on nature in a less chaotic (or more controlled) way. One particular example is the two-dimensional square lattice of magnetic ions shown in figure 1.1(b), where the magnetic interactions J_1 and J_2 between ions can under certain circumstances also lead to degeneracy and *frustration*. Another example is the competition between orbital and spin degrees of freedom on a cubic lattice. Frustrated and low-spin systems are of particular interest since they enhance quantum fluctuations.

The strongly correlated electron systems studied here and, in particular, the TM oxides, exhibit an enormous range of ground states. They can be ferromagnets, antiferromagnets, metals, insulators, and they can display colossal magnetoresistance or metal-insulator phase transitions. The underlying reasons behind

these phenomena are the different degrees of freedom that are all active: spin, charge, lattice and orbital effects are on similar energy scales, with a fine balance existing between them. In order to study their interplay and interrogate these systems further, newly developed techniques and different ways of tackling problems are needed.

All of the compounds investigated in this thesis contain vanadium (V), named after the Scandinavian goddess *Vanadis*. This TM element plays the key role in the magnetic and orbital properties that were measured. It was discovered in 1801 by A.M. del Rio in Mexico City and was rediscovered in 1831 by N.G. Selfström in Falun, Sweden. Vanadium is a shiny, greyish silvery metal, which is soft when pure. It is found as patronite VS_4 but can be obtained as a by-product from other ores and Venezuelan oils. V is used mainly in alloys and in steel. Biologically, it is an essential trace element - although some compounds are quite toxic - and it is stimulatory [2]. The important property concerning us is its oxidation state: 4+ for the $S = 1/2$ frustrated square lattices $Pb_2VO(PO_4)_2$, $SrZnVO(PO_4)_2$, Li_2VOSiO_4, and 3+ for the $S = 1$ TM oxides $GdVO_3$, $LuVO_3$ studied here.

1.1 Frustration

Geometrical spin frustration

The most common form of frustration is found in electronic magnetic spin systems, due to some special symmetry of the magnetic ions in the crystal lattice. If the spin interactions are of the same form for all the bonds, a special lattice geometry may bring about spin frustration. Typical examples are Heisenberg models on triangular or pyrochlore lattices. Let us take the case of a two-dimensional triangular lattice, shown in fig. 1.2, and consider all nearest-neighbour interactions to be antiferromagnetic (AF) and of the same magnitude. The two spins shown (connected by the solid line) satisfy the AF exchange interaction, however the third one cannot fulfill both bonds simultaneously (indicated by dashed lines). In such a frustrated lattice, degeneracy arises from the large number of classical spin configurations which have the same energy.

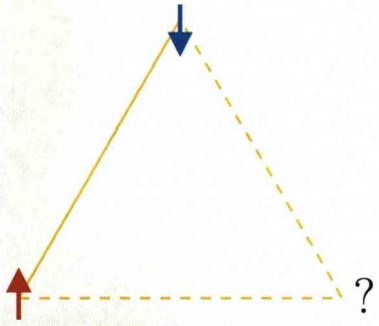

Figure 1.2: In a triangular antiferromagnetic lattice, geometrical spin frustration can occur, since not all exchange couplings can be simultaneously satisfied.

Spin frustration due to higher order exchange terms

Magnetic spin frustration can also occur in square lattices, if one takes into account the next-nearest neighbours. This is not a geometric effect, but a consequence of competition between nearest-neighbour (NN) and next-nearest-neighbour (NNN) magnetic interactions (termed J_1 and J_2 respectively). Consider the square lattice model of fig. 1.3, with ferromagnetic (FM) NN and antiferromagnetic NNN interactions. By satisfying both bonds indicated with the solid yellow lines, one is left with a frustrated spin pair (dashed line). This is the form of spin frustration encountered in this study. It is a slightly newer topic than geometrical frustration, since it turns out to be so hard to discover and grow experimental realisations of these systems, mainly because superexchange usually leads to the dominance of the nearest neighbour term. However, by constructing systems with more complicated exchange pathways, FM and AF interactions with comparable magnitudes for J_1 and J_2 can be achieved yielding, for example, the so-called $J_1 - J_2$ magnetic phase diagram. Various ground states are possible, including spin-liquid regimes as we shall see. These prototypical magnetic systems have fundamental properties that may help in understanding superexchange and high-temperature superconductivity.

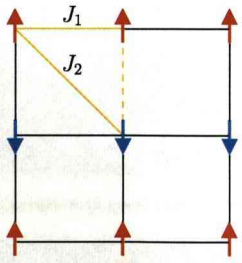

Figure 1.3: The square magnetic lattices studied here can be frustrated, as in this example with FM J_1 and AF J_2 interactions. The frustrated bond is shown with a dashed line. This seemingly simple model exhibits a variety of ground states, as a result of spin degeneracy.

Orbital frustration in simple cubic lattices

The origin of orbital frustration is quite different from that in conventional geometrically frustrated spin systems. The distinct feature of orbitally degenerate models is that frustration occurs for simple lattices and does not require a special crystal geometry or reduced dimensionality. The reason is that the very form of the orbital interaction depends on the bond direction in the crystal. Because of the spatial anisotropy of the orbital wavefunctions, interactions on different bonds require the population of different orbital states and hence compete. A bond directionality of the interactions is a special feature of orbital models which leads to a large degeneracy and pronounced quantum effects. In this way, the orbital degeneracy provides a new root for frustrated quantum models in three dimensions [1]. In TM oxides, the electrons relevant to the superexchange are in the $3d$ states. For vanadates (and titanates), the orbitals occupied (t_{2g}) have the xy, yz and zx symmetries shown in fig. 4.1. It turns out that only 2 out of 3 orbitals for each crystal direction are relevant in the superexchange process, with orbital fluctuations arising between them, as shown in fig. 1.4 [1,3].

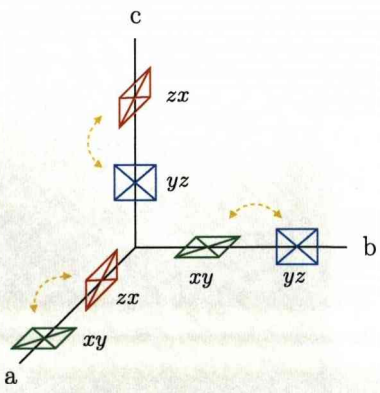

Figure 1.4: On every bond of a cubic crystal, two out of three t_{2g} orbitals are equally involved in the superexchange and may resonate. The same two orbitals also select a particular component of angular momentum (reproduced from [3]).

1.2 Novel experimental approaches

For the systems studied throughout this work, the other important factor - apart from the physics itself - was the experimental way of investigating them. In all cases, newly developed techniques or different ways of applying them was necessary.

Usually, magnetic exchange constants are determined with single-crystal inelastic scattering measurements, via the excitations from the ordered phase. However, it was impossible to grow the large singe crystals required for inelastic neutron experiments of the frustrated square lattices under investigation. The novelty in our approach, was to study the magnetic interactions by using quasielastic diffuse scattering of polarised neutrons. We were able to use polycrystalline samples, i.e. powders, which were much easier for our collaborators to grow. The exchange constants were determined, as we shall see, by using high-temperature series expansion of the static susceptibility $\chi(\boldsymbol{Q})$ in the paramagnetic phase.

TM oxides are strongly correlated electronic systems with lattice, spin, orbital and charge degrees of freedom. X-ray diffraction and neutron scattering are ideally suited to study the first two, via structural and magnetic diffraction respectively. Only recently, however, was resonant x-ray scattering recognised as a good probe for the charge and orbital parameters [4]. This technique allowed us to study the "hidden" orbital order parameter in the perovskite-like $GdVO_3$ compound. The nature of the transitions in a resonant x-ray experiment is not easy to establish [5–10], hence comparison with powerful *ab initio* theoretical calculations was necessary [11]. Orbital excitations have not yet been observed (in these systems), however it is possible to study their effects on spinwave dispersions. Spin-orbital models are essential in understanding basic properties of TM oxides [1].

1.3 Synopsis

In chapter 2, basic neutron and x-ray scattering theory is given, together with a description of the five instruments employed. Emphasis is such that the reader gains insight into the theory (and particular by polarisation analysis for both techniques) rather than writing down complex scattering expressions.

Chapter 3 concerns the frustrated square lattice magnets $Pb_2VO(PO_4)_2$, $SrZnVO(PO_4)_2$ and Li_2VOSiO_4. First, the $J_1 - J_2$ model is presented, and this is followed by our experimental findings. These are then discussed in terms of the $J_1 - J_2$ phase diagram.

The topic of chapter 4 is orbital ordering in $GdVO_3$, where neutron and resonant x-ray results follow the orbital physics. One has to be careful and critical in the interpretation/discussion of the results.

In chapter 5, a simplified view of the spin-orbital superexchange model for cubic vanadates is followed by spinwave dispersions in $LuVO_3$. The measured properties of $LuVO_3$ seem to be accounted very well by this complex theory.

Conclusions and future prospects for all compounds are given in chapter 6.

Chapter 2

Neutron and x-ray scattering

Bulk thermodynamic techniques, such as heat capacity and magnetic susceptibility measurements, identify structural, orbital and magnetic phase transitions. However, the only way to obtain microscopic information on the crystal structures and the ordering of spins and orbitals is by using diffraction techniques, where spatial information is retained. Scattering techniques give some of the most detailed information available on the solid state, and the results provide a rigorous test of theory.

2.1 Scattering theory

2.1.1 Elastic scattering principles

Both neutron and x-ray diffraction techniques involve coherent*, elastic† scattering (termed as *Bragg scattering*) from single-crystal or powdered samples. Figure 2.1 shows a schematic of a general neutron diffraction (ND) or x-ray diffraction (XRD) experiment. Here, the neutrons or x-ray photons are incident on the

*coherent scattering is the one arising from a regular array of atoms in a crystalline material due to interference effects and can be long or short ranged

†elastic scattering is the term used in a situation when there is no energy exchange between the system and the probe (*zero energy transfer*)

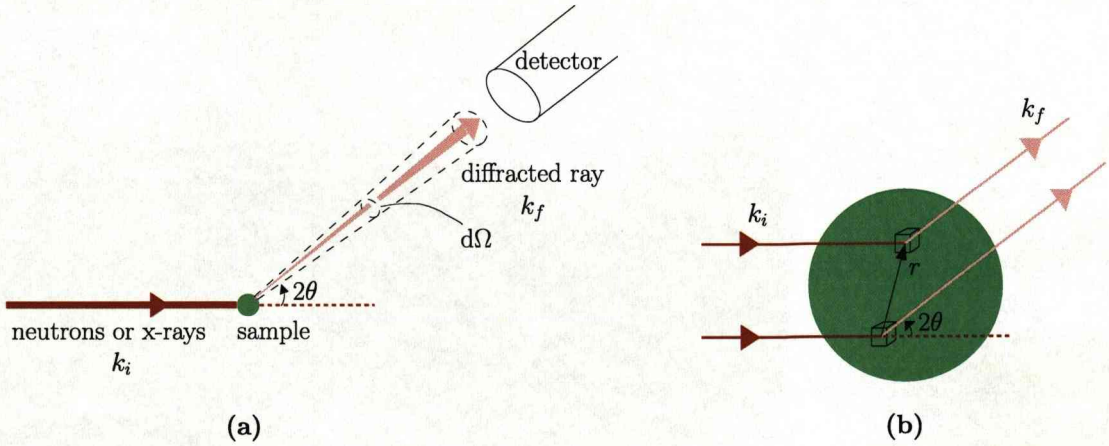

Figure 2.1: General scattering process, after P. Normile [14]. (a) A monochromatic beam of neutrons or x-ray photons is incident on a sample and a diffracted ray emerges, (due to scattering processes) within the solid angle $d\Omega$, at the scattering angle 2θ. (b) A close up of the sample *scattering volume*, showing two rays of the beam scattered by elemental volumes dV separated by a displacement vector $\boldsymbol{r}$.

sample; $\boldsymbol{k_i}$ and $\boldsymbol{k_f}$ are the incident and final wave vectors. The figure also defines the scattering angle 2θ. Details of the production of neutrons and x-rays can be found in [12, 13]. What is of importance here is that they have wavelengths λ of the order of magnitude of lattice parameters ($\sim$ Å). This facilitates the use of these radiations as probes of the crystallographic and magnetic structure [14]. Diffraction occurs when the *scattering vector*

$$\boldsymbol{Q}\ (=\boldsymbol{k_i}-\boldsymbol{k_f})=\boldsymbol{\tau}, \tag{2.1}$$

where $\boldsymbol{\tau}$ is a reciprocal lattice vector of either the crystallographic ($\boldsymbol{\tau}_{xtal}$) or magnetic ($\boldsymbol{\tau}_{mag}$) structures. This above equation is known as the Laue condition for the observation of diffraction. In general

$$\boldsymbol{\tau}=h\mathbf{a}^*+k\mathbf{b}^*+l\mathbf{c}^*, \tag{2.2}$$

where h, k and l are Miller indices, and $\mathbf{a}^*$, $\mathbf{b}^*$ and $\mathbf{c}^*$ are basis vectors of the reciprocal lattice [15]. The result in equation (2.1) can be derived from a classical treatment, involving the summation of the amplitudes of the scattered waves (with their phase-factors) from all the elemental regions of the sample *scattering*-volume (with reference to fig. 2.1(b)). At a diffraction condition, the magnitude of $\boldsymbol{Q}$, since the scattering is elastic ($k_i = k_f = k$), is given by

$$Q = 2k \sin\theta = \frac{4\pi}{\lambda} \sin\theta, \tag{2.3}$$

which is equivalent to Bragg's Law [16].

Any reciprocal lattice vector of the magnetic structure, $\boldsymbol{\tau}_{mag}$, can be decomposed in terms of a reciprocal lattice vector of the crystal-lattice, $\boldsymbol{\tau}_{xtal}$, and a *magnetic wave-vector*, $\mathbf{k}$ (the symbol for this wave vector should not be confused with that of the probe, $\boldsymbol{k}$). It follows that the magnetic reflections are located in reciprocal space at positions given by

$$\boldsymbol{Q} = \boldsymbol{\tau}_{xtal} + \mathbf{k}. \tag{2.4}$$

The symbol $\mathbf{k}$ denotes a *general* magnetic wave vector. The *principal* (or first-order) magnetic wave vectors of a structure are denoted by $\boldsymbol{q}$. As a simple example, a ferromagnetic one-dimensional structure (all spins having the same direction) has $q = 0$.

In both a ND and XRD experiment, the quantity measured at a diffraction (elastic) condition is a *differential cross-section*. This quantity is defined as the intensity of particles entering the detector per unit incident flux and solid angle (refer to figure 2.1(a)). In the kinematic approximation of [13, 17], it has the general form of

$$\frac{\mathrm{d}\sigma}{\mathrm{d}\Omega}(\boldsymbol{Q}) = N\frac{(2\pi)^3}{\nu_{xtal}} \sum_{\boldsymbol{\tau}} |F(\boldsymbol{Q})|^2 \delta(\boldsymbol{Q} - \boldsymbol{\tau}) \tag{2.5}$$

where N is the number of crystallographic unit cells in the sample scattering volume, and ν_{xtal} is the volume of each cell. $F(\boldsymbol{Q})$ is a *unit cell structure factor*, and has the general form

$$F(\boldsymbol{Q}) = \sum_j f_j(\boldsymbol{Q}) e^{i\boldsymbol{Q}\cdot\boldsymbol{r}_j} \tag{2.6}$$

where $f_j(\boldsymbol{Q})$ is a (coherent) *scattering amplitude* of the isotope, atom or magnetic moment (depending upon the type of scattering being considered) at position vector $\boldsymbol{r}_j$ in the crystallographic unit cell. The δ-function in equation (2.5) expresses the Laue condition (eq. 2.1), and is associated with a summation over the lattice points of the crystal as a whole* (in contrast to the $F(\boldsymbol{Q})$ summation carried out within the unit cell)†.

2.1.2 Neutron cross section

Nuclear scattering - coherent and incoherent

The value of the neutron mass results in typical de Broglie wavelengths of the order of interatomic distances in solids for neutrons with thermal energies (i.e. with energies corresponding to temperatures ~ 300 K). Thus, as mentioned before, interference effects occur which yield information on the structure of the scattering system.

Further to that, the fact that the neutron is uncharged means that not only does it penetrate deeply into the target, but also comes close to the nuclei since there is no Coulomb barrier to be overcome. Neutrons are thus scattered by

*This is the concept of the Bravais lattice: an infinite array of discrete points with an arrangement and orientation that looks *exactly* the same, from whichever of the points the array is viewed. Here, it is natural to define the previously mentioned *reciprocal lattice*, as the set of all wave vectors $\boldsymbol{Q}$ that yield plane waves with the periodicity of a given *Bravais lattice*; this could be a chapter and not a footnote.

†Note that Laue's condition gives the positions of the so-called *Bragg peaks* in $\boldsymbol{Q}$ while the structure factor gives their relative intensities. In real space, one can equivalently speak of a general **structure** as being the convolution of a Bravais **lattice** with a **basis** respectively.

nuclear forces, and for certain nuclides the scattering is large. An understanding of the strong nuclear force is lacking, but the scattering of *thermal neutrons* can be modelled by very short-ranged *pseudo*-potentials [18]. These potentials relate to empirically determined values called *neutron scattering lengths*, which are a measure of the neutron-nucleus interaction and are denoted by b. In other words, b is the scattering amplitude f_j of equation (2.6). For thermal neutron scattering, it is independent of $\boldsymbol{Q}$ and has a constant value for each atom. The scattering cross section for a single nucleus is equal to $4\pi b^2$. The general expression for the partial differential cross section from a system of nuclei, defined as the fraction of neutrons scattered into an element of solid angle $\mathrm{d}\Omega$ with a a final energy between E_f and $E_f + \mathrm{d}E_f$, is given by [18]

$$\frac{\mathrm{d}^2\sigma}{\mathrm{d}\Omega\,\mathrm{d}E_f} = \frac{k_f}{k_i}\frac{1}{2\pi\hbar}\int_{-\infty}^{\infty}\langle\sum_{j,j'} b_j b_{j'} e^{-\mathrm{i}\boldsymbol{Q}\cdot\boldsymbol{R}_{j'}(0)} e^{\mathrm{i}\boldsymbol{Q}\cdot\boldsymbol{R}_j(t)}\rangle e^{-\mathrm{i}\omega t}\mathrm{d}t \tag{2.7}$$

where $\boldsymbol{R}_j(t)$ denotes the Heisenberg operator of the nuclear positions and $\langle ...\rangle$ is an ensemble average of the enclosed operator. The summation $\sum_{j,j'}$ extends over all pairs of nuclei. For a single element system at temperatures above a few mK, the nuclear spins and isotopes* are randomly distributed (or completely disordered - like a paramagnet), hence the scattering length b will vary from one nucleus to another. In this case, the nuclear parameters can be decoupled as follows:

$$\frac{\mathrm{d}^2\sigma}{\mathrm{d}\Omega\,\mathrm{d}E_f} = \frac{k_f}{k_i}\frac{1}{2\pi\hbar}\sum_{j,j'}\langle b_j b_{j'}\rangle\int_{-\infty}^{\infty}\langle e^{-\mathrm{i}\boldsymbol{Q}\cdot\boldsymbol{R}_{j'}(0)} e^{\mathrm{i}\boldsymbol{Q}\cdot\boldsymbol{R}_j(t)}\rangle e^{-\mathrm{i}\omega t}\mathrm{d}t. \tag{2.8}$$

This cross section is averaged over all the nuclei with different scattering lengths ($\langle b_j b_{j'}\rangle$ term). On the assumption of no correlation between these b values of different nuclei,

$$\begin{aligned} \langle b_j b_{j'}\rangle &= \langle b\rangle^2, \quad j' \neq j, \\ \langle b_j b_{j'}\rangle &= \langle b^2\rangle, \quad j' = j. \end{aligned} \tag{2.9}$$

*the distribution of different isotopes in a crystal is independent of temperature

Equation (2.8) can be written as

$$\frac{\mathrm{d}^2\sigma}{\mathrm{d}\Omega\,\mathrm{d}E_f} = \langle b\rangle^2 \sum_{j,j'}\langle j',j\rangle + \left(\langle b^2\rangle - \langle b\rangle^2\right)\sum_{j}\langle j,j\rangle \tag{2.10}$$

where $\langle j',j\rangle$, $\langle j,j\rangle$ are written for the prefactor and integral. The first term in eq. (2.10) is known as the *coherent* and the second term as the *incoherent* scattering cross section, with

$$\sigma_{coh} = 4\pi\langle b\rangle^2 \quad \text{and} \tag{2.11}$$

$$\sigma_{incoh} = 4\pi\left(\langle b^2\rangle - \langle b\rangle^2\right). \tag{2.12}$$

The coherent term gives the scattering intensity one would obtain from the same system if all of the nuclei had scattering length $\langle b\rangle$. From equation (2.10) we see that this wave-interference effect arises from correlations between the *same* or *different* nuclei at different times. The remainder of the scattering intensity comes from incoherent scattering, physically arising from the random distribution of the deviations of the scattering lengths from their mean value. We stress again that this random distribution of scattering lengths generally has 2 contributions: a) the random variation of the nuclear spin states above a few mK, and b) the presence of different isotopes in the sample. Incoherent scattering only depends on correlation effects between the *same* nucleus at different times. The scattered waves from different nuclei have random, or indeterminate, relative phases and thus cannot interfere with each other. For a system consisting of a single isotope with zero nuclear spin, the scattering is purely coherent.

Magnetic scattering

Neutrons, having a magnetic moment, also interact with the unpaired electron spins (i.e. electronic charge clouds/densities) in magnetic atoms (dipole-dipole

interaction) with a strength comparable to that of the nuclear interaction. Elastic scattering from this interaction gives information on the arrangement of electron spins and the density distribution of unpaired electrons. The neutron is, therefore, a powerful probe of magnetic properties of solids and has contributed enormously to our understanding of magnetism [18, 19]. The treatment of the magnetic scattering of neutrons is based on the interaction potential, $-\boldsymbol{\mu}_n \cdot \boldsymbol{B}$, between the neutron, of magnetic moment $\boldsymbol{\mu}_n$, and the magnetic field $\boldsymbol{B}$ within the solid, arising from the atomic magnetic moments. This field is determined by the total magnetisation, i.e. the magnetic moments due to spin and orbital motion [14, 17, 18].

For neutrons, the dipolar nature of the magnetic interaction means that only the component of an atom's net magnetic moment perpendicular to the scattering vector $\boldsymbol{Q}$ is effective in scattering neutrons and hence contibutes to the scattering amplitude [18]. Neutron scattering is therefore sensitive to the direction of magnetisation in a material as well as to its spatial distibution.

Magnetic scattering can be coherent (arising e.g. from the magnetic structure or spin excitations of a crystal), or incoherent (e.g. spin fluctuations in a paramagnet).

Inelastic scattering

So far, in describing scattering of neutrons, we have assumed elastic scattering, where incident and final neutron wave vectors are equal: $|\boldsymbol{k_i}| = |\boldsymbol{k_f}|$*. When neutrons are scattered inelastically, $|\boldsymbol{k_i}| \neq |\boldsymbol{k_f}|$ and energy is transferred to the sample:

$$\hbar\omega = E_i - E_f \tag{2.13}$$

where E_i and E_f denote the incident and final neutron energies respectively. For $\hbar\omega > 0$, energy is transferred from the incident neutron to the sample and an

*the scattering vector is defined by $\boldsymbol{Q} = \boldsymbol{k_i} - \boldsymbol{k_f}$, see section 2.1.1

excitation of energy $\hbar\omega$ is created. When $\hbar\omega < 0$, the sample gives up this quantum of energy to the neutron beam and an excitation is annihilated (the neutron gains energy). The kinetic energy of thermal neutrons (0.01-0.1 eV), given by $E = \hbar^2 k^2/2\mathrm{m}$, where m is the neutron mass, is of the same order as that of many excitations in condensed matter. Hence, the associated fractional change in the energy (or velocity) of a neutron is big and relatively easy to measure in such dynamical processes. On the other hand, since the energy of an x-ray is about 10000 eV, very accurate (high-resolution) experiments are required to measure such relatively small effects.

As an example of inelastic scattering, we discuss the case of magnetic materials, with two main possible interactions. First, there will be a component because of the thermal displacement of the magnetic atoms from their equilibrium positions as a result of which the array of magnetic spins is distorted: at the same time the peaks of coherent magnetic reflections will be reduced in intensity. This contribution to the inelastic scattering is termed *magneto-vibrational* scattering [20] (cf. *electron-vibrational* interaction in sec. 4.1). Secondly, changes may be produced in the alignment of the magnetic spin system. Thermal energy and quantum zero-point fluctuations cause the relative orientation of individual magnetic moments in an ordered structure to fluctuate. Because the spins are coupled to one another by exchange interactions, the normal modes of these fluctuations are collective excitations, called *spin waves*. The original idea of these magnetic spin waves came from Bloch (1930) and the energy transmitted by them is quantised in 'magnons'*. The neutrons are then considered to undergo inelastic scattering with either annihilation or production of magnons. The relation between the energy of spin waves, $\hbar\omega$, and the wave vector $\boldsymbol{Q}$ is known as the dispersion law and can be experimentally determined by setting up suitable experiments (see sec. 2.3) [19, 20].

*this is analogous to 'phonons', the quanta of vibrational energy from a system of nuclei in a solid

Diffuse scattering

For atoms completely ordered in a crystalline structure, only sharp 'Bragg' peaks are observed in the diffraction pattern. When the atoms are not fully ordered though, the intensity of Bragg peaks is diminished and some of the scattered intensity appears as *diffuse scattering*. These deviations from a perfectly ordered structure can be static or dynamical, and occupational or displacive. Their correlation functions give rise to the diffuse scattering. The particular kind of disorder studied here is magnetic short-range order, i.e. the spatial fluctuations of magnetic moments.

When examining quasielactic diffuse scattering, it is often useful to integrate over energy transfer so that one obtains the static structure factor $S(\boldsymbol{Q})$. This provides a convenient link to theory, since it is simply related to the static susceptibility $\chi(\boldsymbol{Q})$, which can readily be calculated if the Hamiltonian is known. In fact, by Fourier transformation one sees that the integration over energy transfer relates to information on the pair correlation functions at $T = 0$. Thus, one obtains a "snapshot picture" of the instantaneous correlations [21].

Diffuse magnetic scattering is usually very small in amplitude, and coexists with strong nuclear and magnetic Bragg scattering contributions. In order to separate these components, polarised neutron techniques are necessary.

Polarised neutrons

Each individual neutron has spin $S = \frac{1}{2}$ and an angular momentum of $\pm\frac{1}{2}\hbar$. This can give spin-dependent terms in the cross section, with interesting polarisation effects providing additional details about the scattering system. Polarised neutron beams are often used for determining magnetic correlations, for distinguishing between collective and single particle excitations, and for high resolution spetroscopy [22].

The spin vector of a neutron, $\boldsymbol{S}_n$, defines the polarisation of a neutron beam as

the ensemble average over all neutron spin vectors, normalised to their modulus:

$$\boldsymbol{P} = \langle \boldsymbol{S}_n \rangle / \frac{1}{2} = 2\langle \boldsymbol{S}_n \rangle \tag{2.14}$$

Under the application of an external magnetic field, a quantisation direction is defined, and the neutron can have two possible orientations: parallel or antiparallel to the field. The polarisation can be then expressed as a scalar:

$$P = \frac{N_+ - N_-}{N_+ + N_-} = \frac{F-1}{F+1} \tag{2.15}$$

where N_+ (N_-) is the number of neutrons with spin-up* (spin-down) and $F = \frac{N_+}{N_-}$ is known as the *Flipping Ratio*, a measurable quantity in a scattering experiment. For an unpolarised beam (random neutron spins $\therefore N_+ = N_-$), $P = 0$. For a completely polarised beam, $P = 1$ if all the spins are up, and $P = -1$ if all the spins are down. A neutron's magnetic dipole moment is $\mu_\mathrm{n} = -1.913\mu_\mathrm{N}$, where μ_N is the nuclear magneton and the negative sign indicates that there is a tendency for the neutron to align antiparallel to a magnetic field.

Practically, there are three principal (passive) methods for producing a polarised beam, each with specific advantages in particular experimental situations:

(a) polarising filters (e.g. preferential absorption by polarised ^{3}He nuclei),

(b) polarising mirrors and supermirrors (using preferential reflection) and,

(c) polarising crystals (e.g. $CO_{92}Fe_8$ or Cu_2MnAl Heusler crystal) using preferential Bragg reflection.

The beam, once produced, needs external constant (in the neutron's rest frame) magnetic fields to prevent it from depolarising. The polarisation can also be guided (rotated) or completely flipped by suitably varying magnetic fields or devices called *spin flippers* [23]. This has found extensive application and forms

*Spin can be thought of as an extra degree of freedom for a neutron/electron/nucleus/atom... and better not as an arrow pointing "up" or "down". If this is confusing, just think about it as abstractly as possible, or not at all.

the basis of polarised neutron scattering. From the point of view of magnetism, polarisation analysis (PA) techniques are extremely useful in separating the magnetic scattering from other sorts of scattering (nuclear coherent (Bragg) , nuclear spin incoherent, nuclear isotope incoherent, multiple Bragg, phonon, other background...).

The magnetic cross sections for polarised neutrons are more complicated than the ones previously given, and can generally have spin-flip (SF) and non-spin-flip (NSF) components in all x, y and z axes. They can be qualitatively understood by the following rules of thumb, which are stated here - and sometimes briefly justified - for elastic scattering [24]:

(a) For magnetic* scattering, neutrons are only sensitive to the component of the atomic (electronic) spin $\perp$ to the scattering wavevector $\boldsymbol{Q}$. This is because the dipole-dipole interaction is a non-central force, and is valid independently of the neutron-polarisation direction.

(b) Nuclear coherent scattering (arising from the mean scattering length and giving structural Bragg peaks) only comes in the non-spin-flip cross section. In other words, nuclear scattering from the (infinite) Bravais lattice cannot flip neutron polarisations. This is a consequence of the orthogonality of the wavefunctions of the up and down spin states: $\langle\uparrow \mid \uparrow\rangle = \langle\downarrow \mid \downarrow\rangle = 1$, $\langle\uparrow \mid \downarrow\rangle = \langle\downarrow \mid \uparrow\rangle = 0$.

(c) Isotopic (nuclear) incoherent scattering results from a random disorder in the nuclear amplitudes b_i. Hence, it appears only in the non-spin-flip cross section - like nuclear coherent.

(d) The effective magnetic spin components $\perp$ to the neutron-polarisation direction cause only spin-flip scattering, whereas those $\parallel$ to the polarisation direction give only non-spin-flip scattering.

(e) Nuclear-spin incoherent scattering appears uniformly along all directions (1/3 per direction), since nuclear spin states vary randomly, like a paramagnet.

*the term magnetic scattering is used in this context for the electronic (i.e. atomic) scattering, as opposed to the nuclear-spin incoherent scattering

Hence, 1/3 (2/3) of the total cross section will be along the neutron-polarisation direction ($\perp$ to it) and non-flipped (flipped) according to (d).

For magnetic scattering, point (d), in combination with the fact that only those spin components $\perp$ to $\boldsymbol{Q}$ are effective in neutron scattering (a), gives an important special case. *If the neutron polarisation is along the scattering vector* ($\boldsymbol{P} \parallel \boldsymbol{Q}$), *then all magnetic scattering is spin-flip scattering.* This statement is true for all types of scattering: incoherent, coherent, elastic or inelastic, and is a very useful tool for separating magnetic from nuclear scattering. Note that for $\boldsymbol{P} \perp \boldsymbol{Q}$, the magnetic scattering is split in half between the SF and NSF channels.

Let us now describe two PA methods used here, and give their cross sections.

- ***Parallel - perpendicular difference method***

This technique owes its name to the fact that the neutron beam polarisation $\boldsymbol{P}$ is rotated successively parallel and perpendicular to the scattering vector $\boldsymbol{Q}$. By taking the difference of these two measurements one can separate the purely magnetic scattering. The partial cross sections are given by:

$$\frac{\partial^2\sigma^{\uparrow\downarrow}_{\boldsymbol{P}\parallel\boldsymbol{Q}}}{\partial\Omega\partial E} = \frac{\partial^2\sigma_{mag}}{\partial\Omega\partial E} + \frac{2}{3}\frac{\partial^2\sigma^{spin}_{incoh}}{\partial\Omega\partial E} \tag{2.16}$$

$$\frac{\partial^2\sigma^{\uparrow\downarrow}_{\boldsymbol{P}\perp\boldsymbol{Q}}}{\partial\Omega\partial E} = \frac{1}{2}\frac{\partial^2\sigma_{mag}}{\partial\Omega\partial E} + \frac{2}{3}\frac{\partial^2\sigma^{spin}_{incoh}}{\partial\Omega\partial E} \tag{2.17}$$

$$\frac{\partial^2\sigma^{\uparrow\uparrow}_{\boldsymbol{P}\parallel\boldsymbol{Q}}}{\partial\Omega\partial E} = \frac{1}{3}\frac{\partial^2\sigma^{spin}_{incoh}}{\partial\Omega\partial E} + \frac{\partial^2\sigma^{isotope}_{incoh}}{\partial\Omega\partial E} + \frac{\partial^2\sigma_{coh}}{\partial\Omega\partial E} \tag{2.18}$$

$$\frac{\partial^2\sigma^{\uparrow\uparrow}_{\boldsymbol{P}\perp\boldsymbol{Q}}}{\partial\Omega\partial E} = \frac{1}{2}\frac{\partial^2\sigma_{mag}}{\partial\Omega\partial E} + \frac{1}{3}\frac{\partial^2\sigma^{spin}_{incoh}}{\partial\Omega\partial E} + \frac{\partial^2\sigma^{isotope}_{incoh}}{\partial\Omega\partial E} + \frac{\partial^2\sigma_{coh}}{\partial\Omega\partial E} \tag{2.19}$$

In order to measure the magnetic signal one can take the difference of either the SF ($\uparrow\downarrow$) or NSF ($\uparrow\uparrow$) scattering in the two configurations ($\parallel$ and $\perp$). The spin-flip channel is usually preferred, since it involves no nuclear coherent or isotopic

incoherent scattering. Note than any other partial background cross sections will generally be respectively the same and cancel out too. In this method the polarisation needs to be rotated in a direction parallel to the scattering vector, so it is ideally suited for a point detector.

- ***Three directional polarised neutron scattering***

This technique, also known as the XYZ-difference method, has been conceived by O. Schärpf primarily for use with a multidetector, to overcome the low intensities (of magnetic scattering) that the previous method may suffer from. $\boldsymbol{P} \parallel$ to $\boldsymbol{Q}$ cannot be satisfied for all detectors, and an alternative method is used for magnetic (and not only) separation. Here, one measures SF and NSF cross sections in all x, y and z-axes, and according to the previous rules of thumb we have [25]:

$$\frac{\partial^2\sigma_x^{\uparrow\downarrow}}{\partial\Omega\partial E} = \frac{1}{2}\frac{\partial^2\sigma_{mag}}{\partial\Omega\partial E}(\cos^2\alpha + 1) + \frac{2}{3}\frac{\partial^2\sigma_{incoh}^{spin}}{\partial\Omega\partial E} \tag{2.20}$$

$$\frac{\partial^2\sigma_y^{\uparrow\downarrow}}{\partial\Omega\partial E} = \frac{1}{2}\frac{\partial^2\sigma_{mag}}{\partial\Omega\partial E}(\sin^2\alpha + 1) + \frac{2}{3}\frac{\partial^2\sigma_{incoh}^{spin}}{\partial\Omega\partial E} \tag{2.21}$$

$$\frac{\partial^2\sigma_z^{\uparrow\downarrow}}{\partial\Omega\partial E} = \frac{1}{2}\frac{\partial^2\sigma_{mag}}{\partial\Omega\partial E} + \frac{2}{3}\frac{\partial^2\sigma_{incoh}^{spin}}{\partial\Omega\partial E} \tag{2.22}$$

$$\frac{\partial^2\sigma_x^{\uparrow\uparrow}}{\partial\Omega\partial E} = \frac{1}{2}\frac{\partial^2\sigma_{mag}}{\partial\Omega\partial E}\sin^2\alpha + \frac{1}{3}\frac{\partial^2\sigma_{incoh}^{spin}}{\partial\Omega\partial E} + \frac{\partial^2\sigma_{coh}}{\partial\Omega\partial E} + \frac{\partial^2\sigma_{incoh}^{isotope}}{\partial\Omega\partial E} \tag{2.23}$$

$$\frac{\partial^2\sigma_y^{\uparrow\uparrow}}{\partial\Omega\partial E} = \frac{1}{2}\frac{\partial^2\sigma_{mag}}{\partial\Omega\partial E}\cos^2\alpha + \frac{1}{3}\frac{\partial^2\sigma_{incoh}^{spin}}{\partial\Omega\partial E} + \frac{\partial^2\sigma_{coh}}{\partial\Omega\partial E} + \frac{\partial^2\sigma_{incoh}^{isotope}}{\partial\Omega\partial E} \tag{2.24}$$

$$\frac{\partial^2\sigma_z^{\uparrow\uparrow}}{\partial\Omega\partial E} = \frac{1}{2}\frac{\partial^2\sigma_{mag}}{\partial\Omega\partial E} + \frac{1}{3}\frac{\partial^2\sigma_{incoh}^{spin}}{\partial\Omega\partial E} + \frac{\partial^2\sigma_{coh}}{\partial\Omega\partial E} + \frac{\partial^2\sigma_{incoh}^{isotope}}{\partial\Omega\partial E} \tag{2.25}$$

where α is the angle between $\boldsymbol{Q}^*$ (lying in the xy plane) and an arbitrary x-axis - the "Schärpf angle". For each component there applies the factor converting it

*or a single detector in the multidetector arrangement

into the normal component to $\boldsymbol{Q}$. So, the z-component contributes with the factor 1, being always normal to $\boldsymbol{Q}$, and the x- and y-components contribute with an α dependence. By combining these measured cross sections one can separate the different contributions, with the exception that the nuclear coherent scattering cannot be distinguished from the isotope incoherent scattering. The magnetic cross section can be independently measured in two ways, according to:

$$\frac{\partial^2\sigma_{mag}}{\partial\Omega\partial E} = 2\left(\frac{\partial^2\sigma_x^{\uparrow\downarrow}}{\partial\Omega\partial E} + \frac{\partial^2\sigma_y^{\uparrow\downarrow}}{\partial\Omega\partial E} - 2\frac{\partial^2\sigma_z^{\uparrow\downarrow}}{\partial\Omega\partial E}\right) \tag{2.26}$$

$$\frac{\partial^2\sigma_{mag}}{\partial\Omega\partial E} = 2\left(2\frac{\partial^2\sigma_z^{\uparrow\uparrow}}{\partial\Omega\partial E} - \frac{\partial^2\sigma_x^{\uparrow\uparrow}}{\partial\Omega\partial E} - \frac{\partial^2\sigma_y^{\uparrow\uparrow}}{\partial\Omega\partial E}\right) \tag{2.27}$$

SF has again an advantage for magnetic systems, since it contains none of the nuclear coherent signal. Cross sections for nuclear spin incoherent and nuclear coherent+isotopic incoherent can be found in [25].

The 3-directional method is most widely used for diffuse scattering studies of magnetic correlations in spin glasses, antiferromagnets and frustrated systems [23].

For all these cross sections to be valid (including the $\| - \perp$ method), we assume only the onsite correlation $\langle\xi_\alpha\xi_\beta\rangle = \delta_{\alpha\beta}$ (where α, β are combinations of the x, y, z axes), i.e. no magnetisation correlations between different axes. This is true for collinear magnetic systems. A chiral/helical structure will yield interference terms, and the problem is much more complicated, with non-zero transverse components of the scattered polarisation and with $\uparrow\downarrow$ processes different from $\downarrow\uparrow$ ones [25].

So far we have only been concerned with measuring the scattered intensity associated with a scalar change of polarisation along a particular axis ("longitudinal PA"). For determining more complex magnetic structures, one needs a full description of the scattering processes. This can be done by measuring all components of the polarisation tensor ("3-dimensional neutron polarimetry", i.e. vector or spherical PA) with the Cryopad polarimeter [26].

2.1.3 Synchrotron x-rays

X-rays are electromagnetic waves with wavelengths in the region of an Ångström, hence an extremely convenient probe of the structure of the matter. Quantum mechanically, x-rays can be thought of as being quantised into photons, each carrying an $\hbar\omega$ ($\hbar\boldsymbol{k}$) quantum of energy (momentum). Photons can interact with the atomic electrons in two different ways: they can either be scattered or absorbed. Synchrotrons, being intense and versatile sources of x-rays, are widely used to investigate such interactions.

Bragg diffraction - Thomson scattering

In the classical description of a scattering event, the electric field of the incident x-ray exerts a force on the electronic charge, which then accelerates and radiates the scattered wave. This is an elastic process*. In a discrete lattice, atoms re-radiate coherently and in phase with the incident radiation, giving sharp diffraction peaks. This is generally termed as Bragg scattering (see also section 2.1.1).

Assume that the scattering volume in figure 2.1 is an atom, with a classical electron distribution specified by a number density $\rho(\boldsymbol{r})$. The total scattering of this atom will have contributions from different volume elements within this charge distribution, shown as elemental cubes, and is termed as *classical Thomson charge scattering*. For $\theta \neq 0$, scattered waves from different volume elements $\mathrm{d}\boldsymbol{r}$ will have a phase difference $\phi = (\boldsymbol{k_i} - \boldsymbol{k_f}) \cdot \boldsymbol{r} \equiv \boldsymbol{Q} \cdot \boldsymbol{r}$, where $\boldsymbol{r}$ is the vector between two general volume elements. Hence, for x-rays, the scattering amplitude f_j of equation (2.6), also termed as *atomic form factor*, becomes

$$f^0(\boldsymbol{Q}) = \int \rho(\boldsymbol{r}) e^{\mathrm{i}\boldsymbol{Q}\cdot\boldsymbol{r}} \mathrm{d}\boldsymbol{r}. \tag{2.28}$$

For $\boldsymbol{Q} = 0$, there is no phase difference and the form factor equals the number of

*Inelastic scattering, whereby an incident photon transfers energy to an electron, is possible, but a secondary effect here, termed as Compton scattering.

electrons in the atom, Z. As Q (or θ) increases, the phase factor $e^{i\boldsymbol{Q}\cdot\boldsymbol{r}}$ fluctuates more and more, resulting to a damping of the diffraction pattern. In other words, when the wavelength of the radiation becomes small compared to the atom, there is a destructive interference of the waves scattered from the different parts of the electron charge density [13].

Reciprocal space considerations can also help to show that. The charge distribution $\rho(\boldsymbol{r})$ can be described by a Gaussian with a width corresponding to its spatial extent. The atomic form factor of eq. (2.28), which is nothing but the Fourier transform of $\rho(\boldsymbol{r})$, is another Gaussian, with a width inversely proportional to the width of $\rho(\boldsymbol{r})$. This is a general relationship between real and reciprocal space. For the case of neutrons, there is no form factor, since the size of the nucleus is much smaller than the wavelength. However, if the vibration of atoms is considered as a smearing of the nuclear density, the Debye-Waller factor can be thought of in a similar way to a form factor.

Photoelectric absorption, fluorescent emission and generalised atomic form factor

Electrons in atoms, due to quantisation of atomic energy levels, can excite or de-excite in a variety of ways, giving rise to interesting spectroscopies. Due to the wave-particle duality, an x-ray photon can be absorbed by an atomic electron if the photon's energy is above a certain threshold. This threshold corresponds to the binding energy of an electron in an atom - hence is element and shell specific - and is called an *absorption edge*. The expelled *photoelectron*, which can take the rest of the initial x-ray photon's energy as kinetic, leaves the atom ionised. This *photoelectric absorption* process is schematically shown in fig. 2.2(a). Let us now see the role of absorption in scattering, by considering a structurally allowed Bragg peak of a crystalline material. At low enough x-ray energies (below atomic binding energies), the absorbing response from the sample is reduced since its electrons are

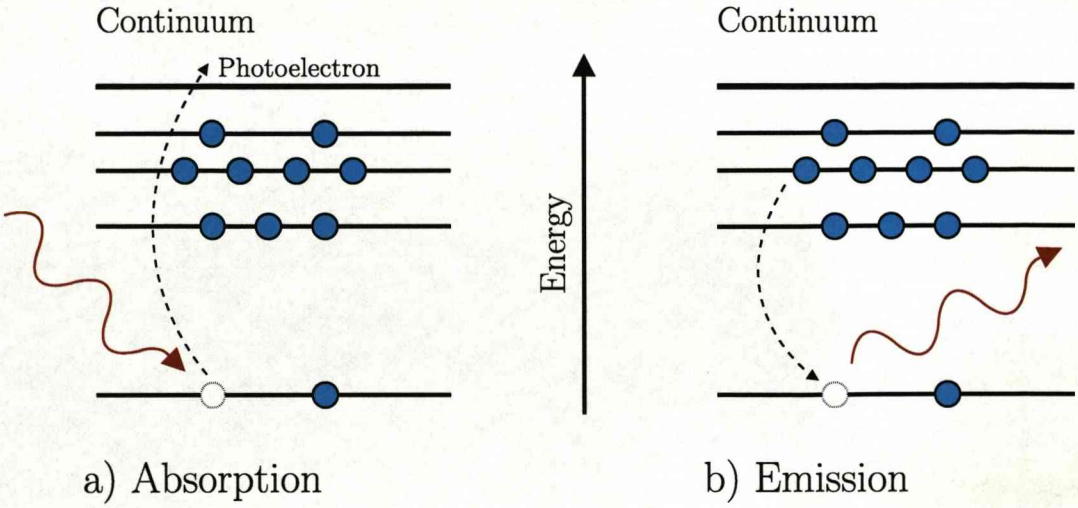

Figure 2.2: (a) An atom can absorb an x-ray, once its energy is large enough to promote a core electron to the continuum (photoelectron). (b) Subsequently, the core state can be filled by an electron from an outer shell with the emission of a fluorescent x-ray. A sharp increase in the fluorescence (absorption) spectrum is observed. Electrons in hypothetical shell structures are shown in blue.

in bound states. Scattering is not affected here. However, as the incident beam is 'tuned' near an absorption edge, resonance terms start becoming important and eventually dominate over the Thomson scattering cross section. The scattering length of an atom is changed here, by an amount denoted conventionally as f'. At much greater energies, electrons can be treated as free and $f' = 0$. In addition to this, the imaginary part of the scattering length can be altered, in analogy with a forced harmonic oscillator. Electrons can have a phase lag with respect to the driving field, introducing a term $\mathrm{i}f''$, representing the dissipation of the system. Collecting all these, the atomic form factor (or total atomic scattering amplitude) becomes

$$f(\boldsymbol{Q}, \hbar\omega) = f^0(\boldsymbol{Q}) + f'(\hbar\omega) + \mathrm{i}f''(\hbar\omega) \tag{2.29}$$

where f' and $\mathrm{i}f''$ are known as the dispersion corrections to f^0 and are energy dependent. Note that the imaginary part is proportional to the absorption cross section σ_α [13].

The absorption process creates a hole in an inner atomic shell. This is subsequently filled by an outer shell electron, with the simultaneous emission of a photon, according to energy conservation (see fig. 2.2(b)). The emitted radiation is known as *fluorescence*, and is of monochromatic nature, hence element specific. Such a spectrum can be measured at a random point $\boldsymbol{Q}$, away from a Bragg peak, and is termed as XANES (X-ray Absorption Near-Edge Structure). Qualitatively, a XANES spectrum has the opposite features of the previously described one at a Bragg position. For low incident beam energies, the absorption is low - and so is the fluorescence, while it rises as approaching the edge. Eventually, it peaks up and above the edge it follows characteristic oscillations [13]. The spectrum provides information about the available *empty* valence states that satisfy certain selection rules. From measurements of the empty valence states, one can infer information about the occupied states of the system. A XANES spectrum for $GdVO_3$ at the V K-edge is shown in fig. 4.11(a).

Angular dependence - linear dichroism

An X-ray Absorption Spectrum (XAS) generally depends on the polarisation direction of the incident beam relative to the crystal axes. The angular dependence is ruled by the symmetry (space group) of the whole crystal and not just the local symmetry of the photoabsorber. Electric dipole transitions ($\Delta l = \pm 1$) from an initial state are dominant (although some pre-edge structures of transition-metal compounds have been attributed to quadrupole transitions, where $\Delta l = \pm 2$), and mathematically involve tensorial (i.e. anisotropic) components. This is because under rotation they transform like the spherical harmonics Y_l^m. For K-edge core-level absorption, with an initial spherically symmetric $1s$ state, the selection rules for Δl ensure that the electric dipole transition will pick up the p component of the final state whereas the quadrupole transition will select the d component of the photoelectron wavefunction. Furthermore, with angle-dependent spectra, it

is possible to obtain selective information on the p_x, p_y and p_z components of the final state (for dipole transitions from a K-edge) by aligning the polarisation vector along the x, y and z axes respectively [27]. The specific advantage of angle-resolved XAS is emphasised in the near-edge region where it gives detailed information on the electronic structure of a particular element in the sample.

Dichroism is a form of angular dependence [27]. Linear dichroism arises from anisotropic tensorial scattering of an oriented structure and depends on the polarisation geometry. It can be defined as the preferential absorption of two orthogonal linear photon polarisation states (e.g. parallel and perpendicular to an orientation axis of the sample).

Resonant scattering

At a resonance, i.e. an atomic absorption edge, the dispersion corrections f' and if'' of the total atomic scattering amplitude (eq. 2.29) take their extremal values. They are known as the *resonant scattering terms* and can be comparable to the Thomson charge term f^0. The unique character of this type of scattering can give, if used correctly in an experiment, enhancement in cross sections that describe ordering phenomena in condensed matter systems [13]. The energy tunability as well as high brightness of synchrotron radiation sources has been a crucial factor in the success of many of these experiments. The first ones were mainly concerned with magnetic properties, although current possibilities include measurements of the charge and orbital ordering parameters, something not directly accessible with neutrons.

The Resonant X-ray Scattering (RXS) method was developed in the 70's by Templeton and Templeton [28], in order to detect the anisotropy of the unoccupied electronic states. Magnetic RXS was first reported by Namikawa *et al.* [29] and Gibbs *et al.* [30] when studying nickel and holmium, and was explained by Hannon *et al.* [31] by use of electric multipole transitions. Blume and Gibbs [32] realised the

importance of polarisation analysis for non-resonant x-ray (magnetic) scattering and used it as a tool in determining magnetic structures. Furthermore, they showed that magnetic and charge peaks can be distinguished in synchrotrons, due to the high degree of linear polarisation of the beam. Finally, it was suggested that PA could be used to separately measure the spin and orbital contributions to the magnetic cross section. This is not directly possible with neutron scattering but a unique characteristic of x-rays. Hill and McMorrow [33] reformulated RXS theory for experimentalists, in terms of synchrotron σ and π linearly polarised states (for definitions see section 2.6). Electric dipole and quadrupole cross sections can be found in this reference. In 1998, the RXS method was first used to study orbital and charge ordering in $La_{0.5}Sr_{1.5}MnO_4$ by Murakami and coworkers [4]. Following this, the technique has developed rapidly and several orbitally active compounds have been investigated.

RXS can be described classically, by viewing an atom as an assembly of damped forced charged oscillators, or quantum mechanically by time-dependent perturbation theory [13]. In this latter description, the quantity of interest in deriving the cross section is the transition rate probability W between initial $|i\rangle$ and final $|f\rangle$ states of the combined system of x-ray photon plus target electron. In second-order perturbation theory the transition probablility is given by

$$W = \frac{2\pi}{\hbar} \left| \langle f|\mathscr{H}_I|i\rangle + \sum_{n=1}^{\infty} \frac{\langle f|\mathscr{H}_I|n\rangle\langle n|\mathscr{H}_I|i\rangle}{E_i - E_n} \right|^2 \rho(\mathscr{E}_f) \tag{2.30}$$

where the Hamiltonian $\mathscr{H}_I$ describes the interaction between the photon and the electron, and $\rho(\mathscr{E}_f)$ is the density of states. As an aside, the first term, $\langle f|\mathscr{H}_I|i\rangle$, is the matrix element M_{if} from Fermi's Golden Rule. It is the first-order perturbation term, which gives an interaction Hamiltonian

$$\mathscr{H}_I = \frac{e\boldsymbol{A}\cdot\boldsymbol{p}}{m} + \frac{e^2A^2}{2m} \tag{2.31}$$

responsible for photoelectric absorption and Thomson scattering (first and second terms respectively). $\boldsymbol{A}$ is the vector potential describing electromagnetic fields, $\boldsymbol{p}$ is the momentum operator of the electron, while e and m refer to the electron's charge and mass. Let us now return to eq. (2.30) and in particular its higher-order resonant scattering term. This second-order perturbation sum is over all possible states $|n\rangle$ with energy E_n. In this case, the $\boldsymbol{A}\cdot\boldsymbol{p}$ term produces scattering via this intermediate state $|n\rangle$. The semi-classical picture for RXS can be given by putting eq. (2.30) into words: the incident photon is destroyed after interacting with a core electron at initial state, say $|\alpha\rangle$. This electron makes a 'virtual transition' to the intermediate state $|n\rangle$, only to 'relax back' to $|\alpha\rangle$. This elastic process is accompanied by the creation of a scattered photon, the experimentally detected one. The resonant behaviour arises when the denominator tends to zero. This occurs when the total incident energy, $E_i = \hbar\omega + E_\alpha$, is equal to the energy of the intermediate state E_n or equivalently the incident photon energy $\hbar\omega$ corresponds to an absorption edge. However, RXS is a quantum mechanical process and the above two-step picture is not truly correct for these virtual transitions [13].

The important point to make about RXS is that it is a powerful probe of the intermediate atomic states. Virtual transitions to these states are governed by two considerations. The Pauli exclusion principle requires that only unoccupied intermediate states can be accessed, while quantum mechanical selection rules imply that electric dipole transitions dominate the cross section [13]. As an example, magnetic order effects can be observed if intermediate states are split by magnetic interactions [29,30,34]. Alternatively, RXS can be used in probing the charge and orbital degrees of freedom in a condensed matter sample [6,7,10,35]. Classically forbidden Bragg reflections may appear under resonance conditions, originating from charge or orbital ordering. Furthermore, polarisation analysis can yield information on the anisotropic tensorial scattering of an individual orbital orientation in a structure.

To conclude, RXS is a probe of intermediate unoccupied atomic states, and its sensitivity to magnetic (or orbital) ordering arises if the degeneracy of the intermediate state is lifted by magnetic (or Jahn-Teller, see section 4.1) interactions. The use of RXS in the study of orbital degrees of freedom is reviewed in a paper by Ishihara and Maekawa [36].

2.2 D9 neutron diffractometer

This is a hot neutron four-circle diffractometer, used for precise measurements of Bragg intensities (elastic scattering) up to very high momentum transfers. Incident neutron beam energies are relatively large, hence the term 'hot neutrons'. The way of achieving this is by thermalising the neutrons in a hot source at 2000° K. The D9 instrument (D standing for diffraction) is situated very close to

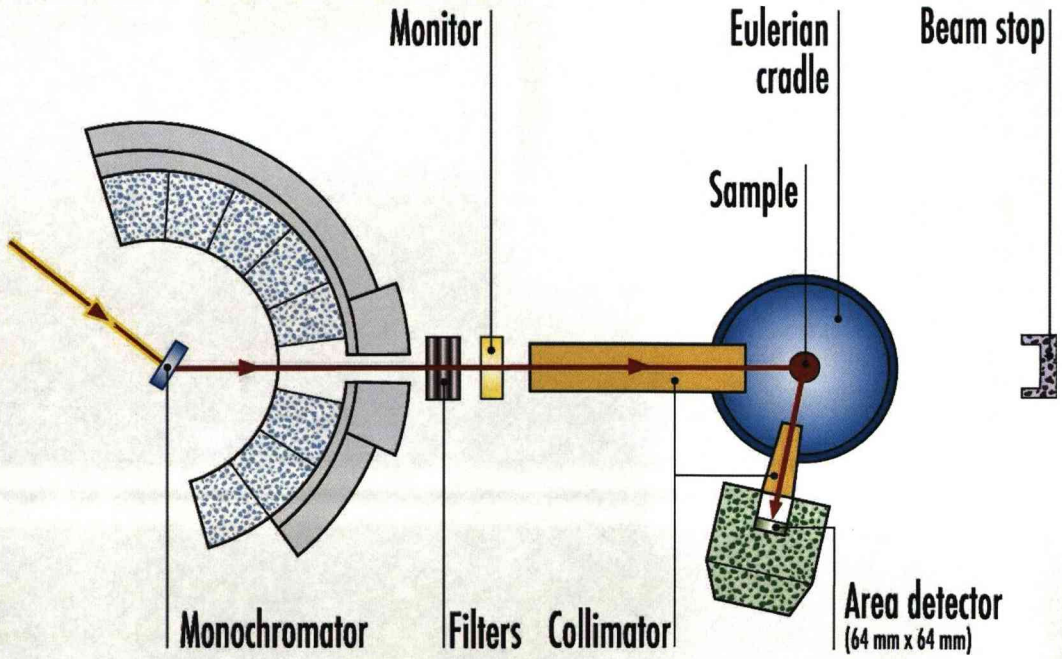

Figure 2.3: D9 instrument layout. This hot neutron four-circle diffractometer offers the possibility of measuring highly-absorbing samples [37].

the core of the nuclear reactor of the Institut Laue-Langevin (ILL) in Grenoble. Hence, the neutron flux is relatively high, of the order of 10^7 n cm^{-2} s^{-1} at the sample position. Outcoming neutrons from a reactor have a variety of wavelengths and are typically monochromated. A Cu crystal is used as a monochromator here, with the (220) reflection giving incident wavelengths ranging between 0.25 and 0.85 Å (fig. 2.3). In order to supress $\lambda/2$ contributions several resonance filters are available. These wavelengths are among the shortest available in the world and give the possibility of accessing a wider range of $\boldsymbol{Q}$. Since more Bragg reflections can be measured, structures can be determined more accurately. Identification of very small atomic displacements is possible for studies of effects such as atomic disorder and atomic thermal motions. Furthermore, hot neutrons are much more penetrating than thermal or cold neutrons (lower energy ones), and hence provide a way of measuring systems containing highly absorbing elements such as Gd. This is the main reason why we employed D9 in our studies of $GdVO_3$. The sample holder is an Eulerian cradle, with a standard four-circle geometry allowing the sample to be oriented with respect to the beam by moving it around four rotation axes. A small two-dimensional position-sensitive area detector is employed. Finally, different temperatures and magnetic fields can be achieved with displex or He-flow cryostats, furnaces and cryomagnets [37].

2.3 IN8 triple-axis spectrometer

The triple-axis (or three-axis) spectrometer is an effective tool for both elastic and inelastic measurements. It is the most versatile and useful instrument for inelastic experiments, allowing to probe nearly any coordinates in energy and momentum space in a precisely controlled manner. This elegant concept, developed by Brockhouse in 1961, has three axes corresponding to rotations of the monochromator, the sample, and the analyser (see figures 2.4 and 2.5). The monochromator defines

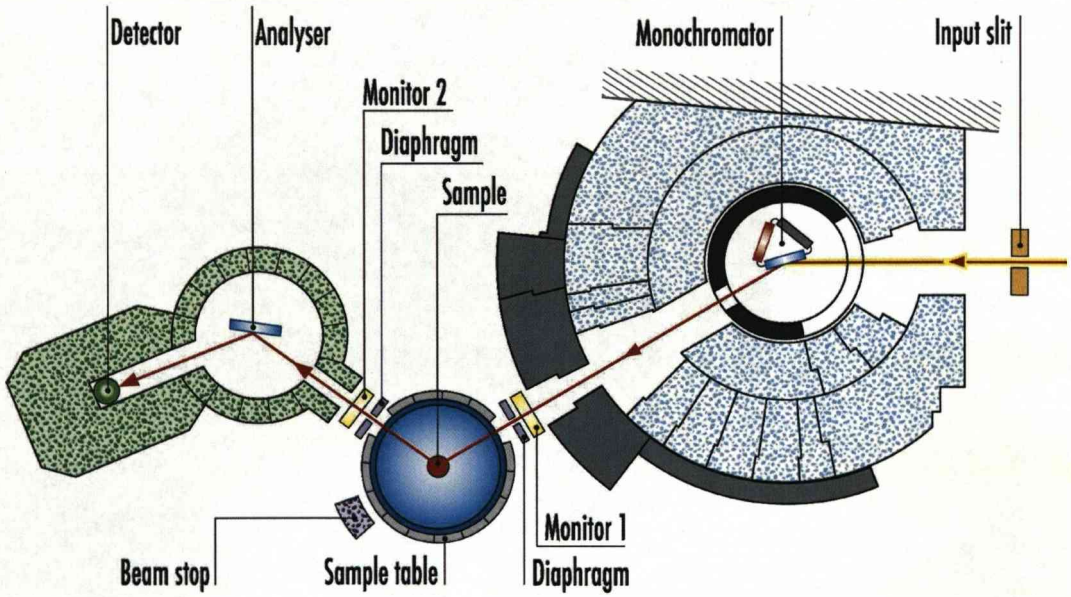

Figure 2.4: Diagram of the IN8 triple-axis spectrometer. This high flux thermal neutron instrument is designed for measuring excitations on single crystals over a wide range of energy and momentum transfers [37].

the direction and magnitude of the momentum of the incident beam (as in the previously described D9 instrument) and the analyser performs a similar function for the scattered beam [19]. In an experiment, one typically holds one wave vector ($\boldsymbol{k_i}$ or $\boldsymbol{k_f}$) constant while varying the other. $\boldsymbol{Q}$ is normally held constant while the energy transfer is varied ("energy scans"). Alternatively, one can perform "$\boldsymbol{Q}$ scans" by keeping the energy transfer fixed and varying momentum transfer. By making many such measurements, spin or phonon dispersions along desired directions in reciprocal space may be mapped out.

IN8 (IN standing for inelastic) is a high flux ($> 10^8$ n cm^{-2} s^{-1}) thermal neutron three-axis spectrometer designed for inelastic measurements on single crystals over a wide range of energy (few meV to $\sim$ 100 meV) and momentum transfers. Inside the large cylindrical structure of fig. 2.4 is a three-faced monochromator, equipped with pyrolytic graphite (PG) (002), Cu(200) and Si(111) crystals.

Typical analysers used include PG(002), PG(004) and Si(111) crystal reflections. Converging collimators as well as diaphragms can be placed to optimise the beam dimension and definition. A standard sample environment similar to the one descibed in section 2.2 is available here too, with high field magnets and wide T variations. Furthermore, for low scattering angle experiments, the sample-analyser distance can host a vacuum box to reduce air scattering. The detection of the scattered neutrons is by a ^{3}He gas-filled proportional-counter detector [37]. This highly absorbing isotope detects neutrons via a charge particle, emitted in the capture process [20].

Applications of IN8 include magnetic excitations in high-temperature superconductors, low-dimensional magnets and Spin-Peierls systems. Because of its high flux (the instrument is situated in the main reactor hall), it is well suited for small sample volumes and systems with weak magnetism. The instrument is also used for investigations of lattice vibrations (phonons) and excitations in liquids [37]. No polarisation analysis is available, so one has to design a magnetic experiment carefully. A good test is the T dependence, since magnons should dissapear above the Néel temperature. Always measure your background.

2.4 IN20 triple-axis spectrometer with polarisation analysis

The main attribute of this thermal neutron three-axis spectrometer (principle described in section 2.3) is its PA capabilities. Previously (sec. 2.1.2), we saw how this can separate magnetic scattering from other types of 'background' scattering. Being a ^{3}He single-detector instrument, the $\| - \perp$ PA method is naturally used. For this, the sample is surrounded by a standard set of Helmholtz coils, producing a guiding field of $\sim$ 15 Gauss that can be applied along any direction. Another PA option is 3-dimensional neutron polarimetry (with the Cryopad), or the spin-

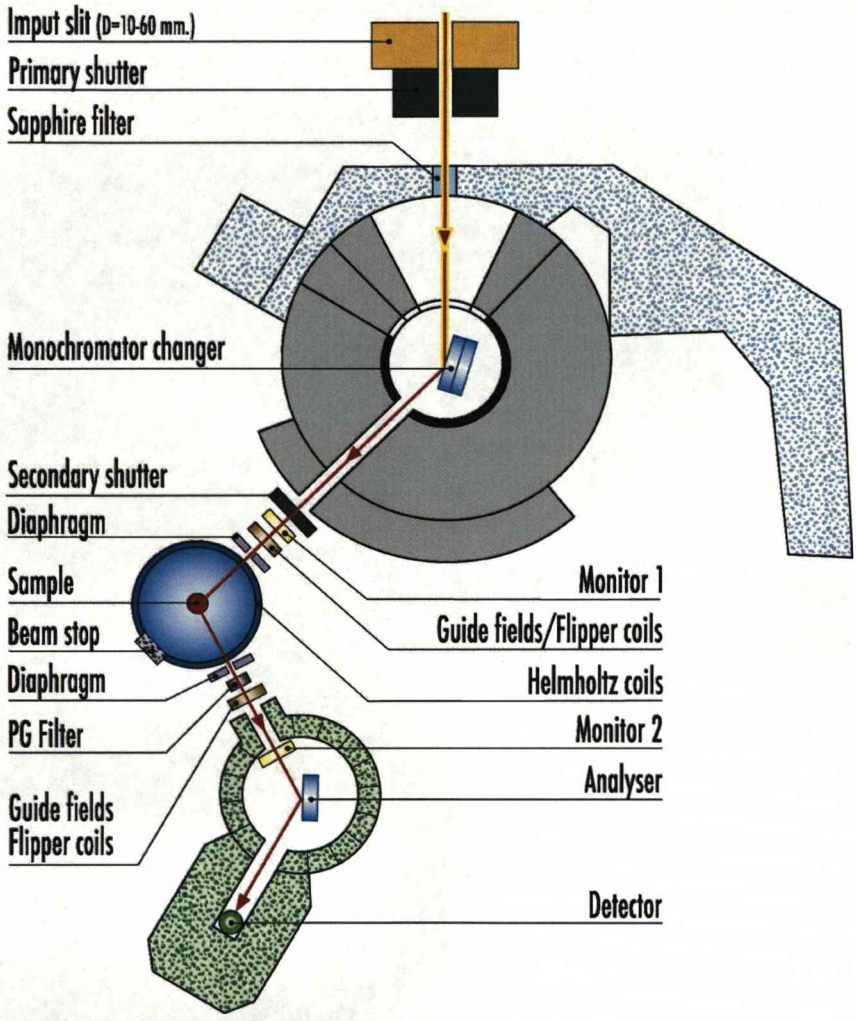

Figure 2.5: The IN20 triple-axis spectrometer with PA, ideal for magnetic scattering studies [37].

echo technique which improves the energy resolution and can measure very slow dynamics. In order to use these more advanced techniques, the Helmholtz coils have to be replaced accordingly. The neutron energy and spin state are selected by a Heusler (111) monochromator. Similarly, a Heusler (111) analyser is used for the analysis of the energy and polarisation state of the scattered neutrons. All the beam paths are surrounded by permanent-magnet spin guides, giving an overall beam polarisation of about 90% (flipping ratio 20). For unpolarised neutrons, a

Si(111) crystal can be used as a monochromator, and a PG(002) or Si(111) as analysers. The drawback to using PA is intensity loss, typically by a factor of 10 (10^7 n cm^{-2} s^{-1} for this instrument compared to 10^8 for IN8). A sapphire filter is placed before the monochromator to reduce fast neutron background. All these features can be seen in fig. 2.5. The sample environment of IN20 is the standard ILL one, with orange cryostats, furnaces, cryomagnets etc. available [37].

2.5 D7 diffuse scattering spectrometer

This truly unique instrument, originally designed and built by Otto Schärpf, is a cold neutron multidetector diffractometer with polarisation analysis. The multidetector banks, shown in fig. 2.6, are ideal for use with three directional or full XYZ PA, as discussed in section 2.1.2. This allows the unambiguous separation of magnetic, nuclear spin incoherent and nuclear coherent+isotopic incoherent scattering contibutions over a large range in $\boldsymbol{Q}$. Hence, D7 is ideal in the study of (weak) diffuse scattering from single crystals or polycrystalline materials, arising from disorder phenomena such as short-range order, spin glasses, defect structures etc. Its energy window in measuring $S(\boldsymbol{Q})$ is up to about 10 meV, corresponding to the maximum energy loss of incident neutrons. A Fermi chopper may be used, giving an option for energy analysis of the scattered neutrons by the time-of-flight method, i.e. $S(\boldsymbol{Q}, \boldsymbol{\omega})$ measurements (see section 3.3.1 for correlation functions description). The majority of the experiments however, are performed with the disk chopper removed, so one integrates over energy transfer.

The D7 operation is now described, with reference to fig. 2.6. Neutrons are monochromated by a PG(002) crystal array, with a wavelength option of 3.1, 4.8 or 5.8 Å. A Be filter ensures that higher orders of the incident wavelength, λ/n, are supressed. The neutrons are then polarised in the spin-up state by a supermirror bender and pass through a Mezei π-spin-flipper (only turned on for

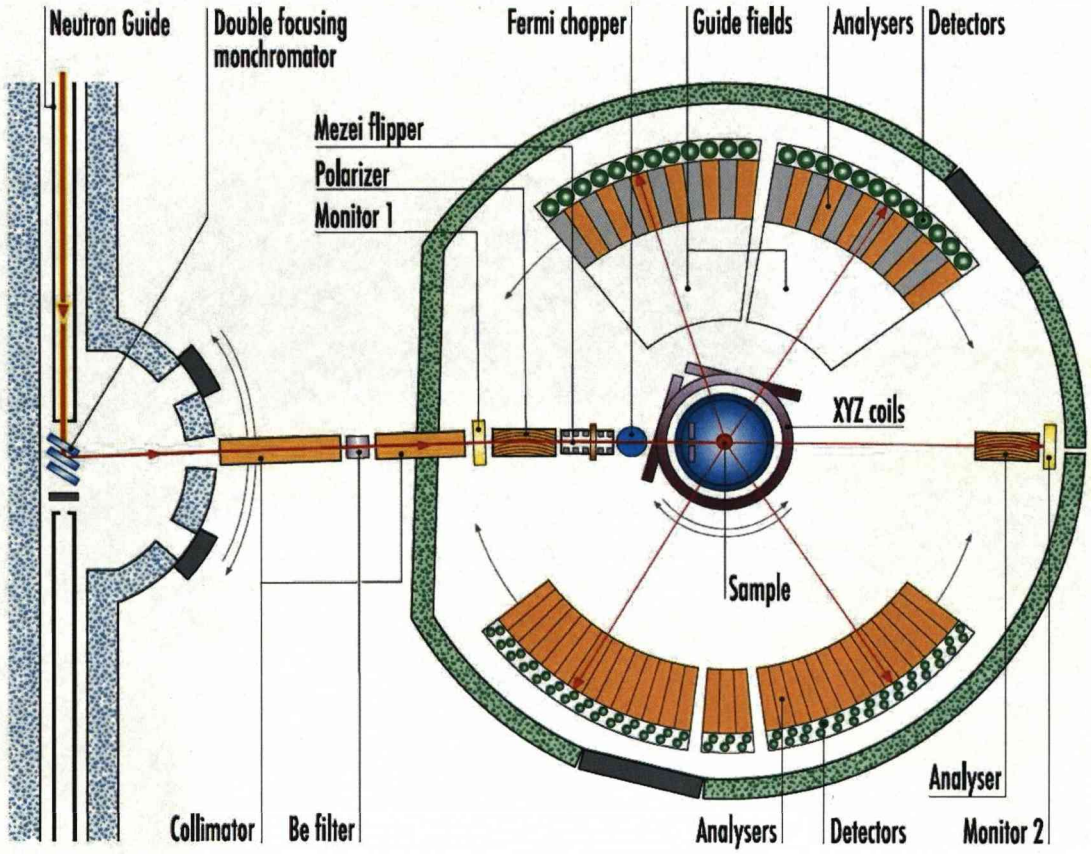

Figure 2.6: Schematic diagram of the D7 cold neutron diffuse spectrometer. Its XYZ polarisation analysis makes it unique in measuring magnetic short-range correlations, point defects, frustrated magnets and spin glasses [37].

SF cross sections). The neutron polarisation is maintained in the z-direction by a neutron guide field of ~ 1 mT. Three orthogonal XYZ coils around the sample position produce magnetic fields in all three directions, allowing for the incident neutron spin direction to be defined, as in IN20. The initial beam polarisation can be rotated by $\pi/2$ from the z-direction onto the x- or y-directions before reaching the sample. After the scattering process, the polarisation is rotated back by $-\pi/2$, allowing the sequential measurement of the SF and NSF cross sections in each direction (a total of 6 measurements). The neutrons are then analysed by supermirrors (allowing only spin-up states to pass) and detected by ^{3}He tubes

installed directly after them. The polarised neutron flux of this instrument is $\sim 10^6$ n cm^{-2} s^{-1}, and the sample environment includes a dedicated cryostat and furnace, as well as a cryomagnet and cryofurnace ($1.2 < T < 800$ K and magnetic fields up to 5.5 Tesla).

Various corrections to raw D7 data are required in order to obtain meaningful results. For example, detector efficiencies vary from one detector to another. Vanadium has the property of being an almost pure spin incoherent scatterer, hence with isotropical behaviour over 4π steradians. This is used in normalising relative detector efficiencies. The absolute scale of the differential cross section is also deduced from this measurement, since V has a well known total cross section. In order to ensure an accurate separation of SF and NSF cross sections, the flipping ratio of each supermirror analyser has to be determined. This is done by an amorphous quartz (SiO_2) measurement, which ideally has an entirely NSF cross section. Furthermore, the background scattering contributions from the cryostat, sample holder, air, etc. can be subtracted by measuring an empty sample holder as well as scattering from a sheet of cadmiun (totally absorbing) in place of the sample. Finally, the transmission of the sample needs to be taken into account [37, 38].

2.6 XMaS resonant x-ray scattering beamline

The **X**-ray **Ma**gnetic **S**cattering (**XMaS**) beamline is situated on a bending magnet [13] at the European Synchrotron Radiation Facility (ESRF), in Grenoble. It incorporates a unique combination of experimental techniques and equipment, sample environment and staff. XMaS has been designed to perform single crystal high-resolution diffraction over a continuously tunable energy range from 2.3 to 15 keV. The 'white beam' of the synchrotron's radiation is monochromated by a double bounce Si(111) water cooled crystal monochromator, shown in fig. 2.7.

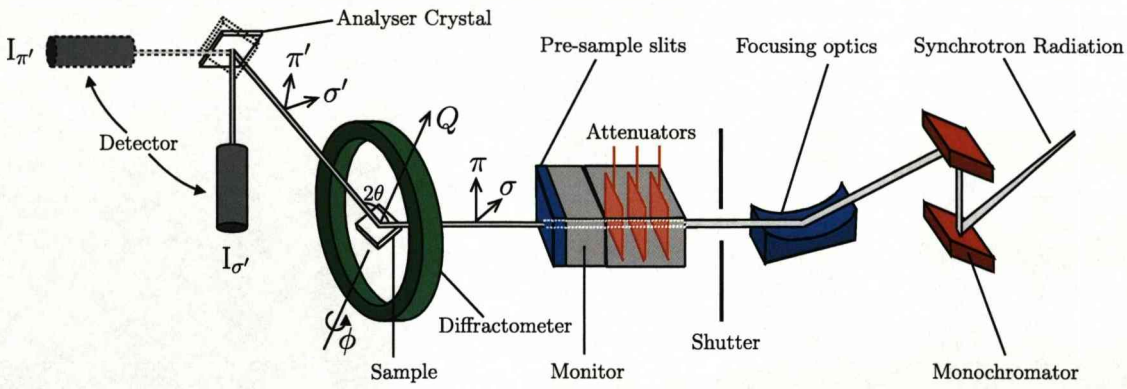

Figure 2.7: Layout of the XMaS facility at the ESRF, an instrument ideal for resonant x-ray scattering experiments (adapted from [39]). It comprises a versatile diffractometer, with tunable photon energy, well defined incident polarisation and polarisation analysis. The azimuthal degree of freedom ϕ is also shown.

The beam is then focused to the centre of the diffractometer using focusing optics (Si toroidal mirror), and if necessary attenuated by various metal foils. Its size can be adjusted by appropriate slits installed before the sample as well as in front of the detector. Apart from point detectors (NaI scintillators, Ge solid state detector, vortex Si drift diode, avalanche photodiodes), a MAR CCD area detector is also available. Harmonic rejection mirrors are installed to remove unwanted contamination wavelengths [39, 40].

XMaS offers polarisation analysis, an extremely useful technique for resonant x-ray studies of magnetic and orbital ordering. A synchrotron provides a radiation beam linearly polarised, with a direction parallel to the electron/positron orbit plane, referred to as σ polarisation. A π polarised component will lie at 90° to the synchrotron plane. In an experiment, one can select σ' or π' outgoing waves (incoming ones are always σ) by appropriate polarisation analysis, and hence measure $\sigma - \sigma'$ or $\sigma - \pi'$ scattering processes. A polarisation analyser is used for that, with an analyser crystal giving a diffraction condition parallel or perpendicular to the synchrotron plane. In order to do so, the analyser is rotated around an axis parallel to the scattered photon momentum. The wide

variety of PA crystals in XMaS covers many possible incident energies, with the polarisation analyser always fulfilling a $\theta_{\text{Bragg}} \sim 45°$ condition. The detector needs to be moved in conjunction with the PA crystal. This, together with σ and π states before and after scattering are shown in fig. 2.7. As an example, the $\sigma - \pi'$ (or $\sigma - \pi$ for brevity) channel eliminates the charge scattering, since charge scattering by its nature cannot rotate the polarisation vector of the beam. Any possible observed signal can arise from other processes in the sample, such as magnetic or orbital ones. A key signature of these phenomena is the ϕ-angle dependence. The ϕ circle, shown in fig. 2.7, rotates the sample about the surface normal (or scattering wave vector $\boldsymbol{Q}$) direction, and is termed the azimuthal degree of freedom. Note that the incident linearly polarised radiation can be converted into a circularly polarised beam by use of diamond phase plates, to allow for x-ray circular dichroism measurements.

The XMaS sample environment has temperatures ranging from 1 to 800 K, as well as a specially made 4 Tesla superconducting magnet, designed by S. Brown and P. Thompson. C. Lucas *et al.* are known to be using this facility with custom electrochemical environments [40].

Chapter 3

Square-lattice vanadates with strong cross-bond exchange

Superexchange usually falls off dramatically as the exchange path increases, so that nearest-neighbour magnetic exchange dominates. However, some square lattice vanadates have been discovered with comparable next-nearest-neighbour exchange. The first two prototypes of frustrated two-dimensional quantum Heisenberg antiferromagnets (2DQHAF) discovered were Li_2VOSiO_4 and Li_2VOGeO_4 [41–43]. They are insulating vanadium oxides, with spin $S = 1/2$ V^{4+} ions arranged in square lattice planes, at the centres of VO_5 square pyramids. These are linked by SiO_4 or GeO_4 tetrahedra, with Li ions occupying the space between the V-O planes. Because of their relatively complex structure, the magnetic ions are well separated, with weak superexchange between nearest and next-nearest neighbouring V ions mediated by more than one intermediate O ion (low energy scale systems). Li_2VOSiO_4 is the most studied of the two compounds, showing a collinear ground state with spins along the x-direction [44]. Thermodynamic measurements are most readily compared to theory when the temperature is sufficiently high to rely on a first-order high-temperature series expansion (HTSE). However, in this limit the magnetic susceptibility can only give directly the sum of $J_1 + J_2$ and not

individual values. In order to get J_1 and J_2 individually, one has to fit higher-order high-temperature series expansion to the uniform susceptibility and specific heat. Serious attempts combined with perturbative mean-field theory (MFT) and local-density approximation (LDA) have been made to get this information but unfortunately the results of J_2/J_1 are found to vary from 1.1 [43] to 4.8 [45] up to 11.7 [46, 47].

Here, we consider a new class of the $J_1 - J_2$ model with ferromagnetic nearest-neighbour (NN) exchange and comparable antiferromagnetic next-nearest-neighbour (NNN) exchange. In addition to that, a completely new way of measuring J's is employed, by making use of polarised neutron scattering. Results of uniform magnetic susceptibilities are used as constraints to the neutron measurements, forming the starting point of the fitting procedure.

3.1 $J_1 - J_2$ model on a square lattice

We consider the following Heisenberg model on the square lattice:

$$\mathscr{H} = 2J_1 \sum_{<i,j>_1} \boldsymbol{S}_i \cdot \boldsymbol{S}_j + 2J_2 \sum_{<i,k>_2} \boldsymbol{S}_i \cdot \boldsymbol{S}_k \tag{3.1}$$

where $< i, j >_1$ and $< i, k >_2$ refer to pairs of nearest and next-nearest neighbours respectively, as shown in fig. 3.1. Although quite simple in appearance, this spin model realises several interesting phenomena which are relevant to a large class of 2D frustrated quantum magnets: classical degeneracy, order by disorder, destruction of some long-ranged order by quantum fluctuations, break down of the spin-wave expansion, opening of a spin gap and possibly spontaneous translation symmetry breaking, etc [48]. Further to that, the discovery of high T_c superconductivity (HTSC) in doped layered cuprates whose undoped parent compounds are spin-half antiferromagnets, has led to a renaissance of interest in 2D frustrated

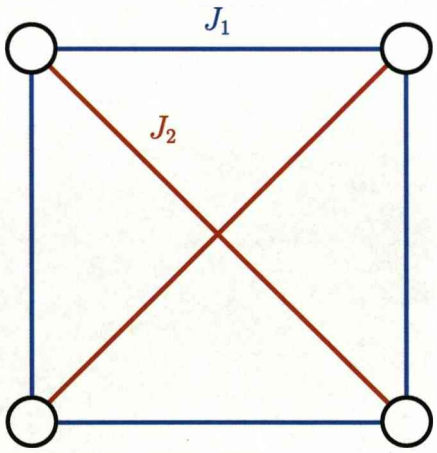

Figure 3.1: Square lattice of magnetic ions showing nearest and next-nearest neighbour interactions (J_1 and J_2 respectively).

magnets. The $J_1 - J_2$ model in particular has attracted renewed attention, both because of its simplicity and the possibility that its spin-gapped phase might provide a realisation of Anderson's resonating valence bond (RVB) concept [49–51]. According to this early proposition, for small spin values, strong quantum spin fluctuations may generate a novel spin-liquid ground state with no long-range order. The superconductivity was then conjectured to arise from the behaviour of a quantum fluid created out of a highly correlated set of electronic degrees of freedom. This disordered phase may arise from mobile holes in an AF background, giving rise to effective frustrating couplings in an undoped Heisenberg model such as HTSC Cu oxides and eventually leading to the breakdown of Néel order. Alternatively, competition of purely magnetic interactions can also lead to destruction of long-range order as in the $J_1 - J_2$ model. It has also been predicted that the $J_1 - J_2$ system presents a quantum disordered (spin-liquid) phase due to the NNN frustrating interaction J_2. For all these above reasons we start with a small general overview of some important results concerning this system. We will focus on the properties related to *frustration*. A review on the non-frustrated model ($J_2 = 0$ in eq. 3.1) can be found in [52].

3.1.1 Antiferromagnetic interactions on the square lattice

In this section we will consider the case when both exchange interactions J_1 and J_2 are antiferromagnetic. This theoretical model was the first one proposed and hence we will use a few examples on it to get some basic results. The generalised case described in 3.1.2 will then follow easily from these.

Néel antiferromagnetic order for $J_1 \gg J_2$

To start off with, assume that $J_1 \gg J_2$ and take for example a 'red' atom (spin 'up') in fig. 3.2. All of its nearest neighbouring magnetic ions will 'want' to have a spin 'down' configuration in order to satisfy the AF nearest neighbour interaction. The NNN interaction does not play a crucial role at this stage since it is negligible. We can hence easily see that in this case we get the usual long-range ordered (LRO) Néel antiferromagnetic state (NAF) with a magnetic ordering wave-vector of $\boldsymbol{Q} = (\pi, \pi)$. It is obvious - and clearer - that J_1 alone ($J_2 = 0$) favours this Néel LRO as well, being the limiting case of $J_1 \gg J_2$.

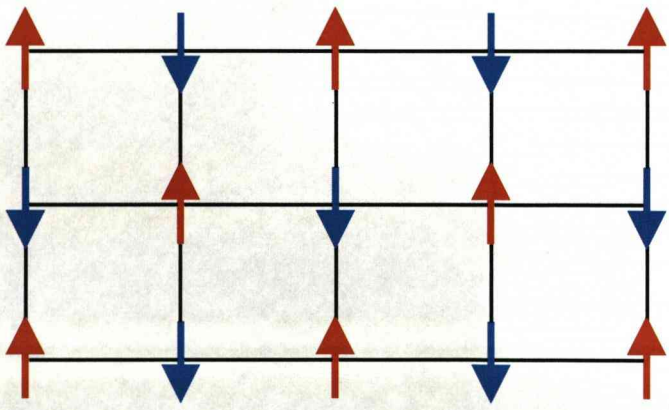

Figure 3.2: Néel antiferromagnetic structure on a square lattice with AF nearest and next-nearest neighbour exchanges ($J_1 \gg J_2$).

Collinear antiferromagnetic order for $J_1 \ll J_2$

To continue, let us take the opposite extreme in which $J_1 \ll J_2$ and in particular $J_1 = 0$. In the same sense as before, this will favour two interpenetrating Néel sublattices with independent staggered magnetisations, as shown in fig. 3.3 (a). The sublattices are rotated by 45° and enlarged by a factor of $\sqrt{2}$ compared to before, but the ordering principle on each sublattice is exactly the same as in the Néel case above. Since nearest neighbours do not interact magnetically ($J_1 = 0$), the sublattices are independent to each other and there is an infinite degeneracy for the relative spin directions in the two. This means that they can point in any random direction since there is no energy cost when rotating globally all the spins of one sublattice with respect to the other.

Interestingly enough, by introducing an infinitesimal J_1, quantum zero-point spin fluctuations can select configurations where both sublattices have their staggered magnetisations collinear in spin space, as shown in fig. 3.3 (b). This collinear antiferromagnetic (CAF) ground state has its minimum energy at a $\boldsymbol{Q} = (0, \pm\pi)$ or $(\pm\pi, 0)$ magnetic ordering wave vector, corresponding to ferromagnetic lines arranged in an antiferromagnetic way. Thus, the ground state breaks the spin-rotational symmetry as in an antiferromagnet, and additionally the 90° rotational symmetry of the square lattice.

This idea of "*order by disorder*" can be traced back to a remark by Villain *et al.* [53], in the study of a frustrated Ising model on the square lattice. With thermal or quantum fluctuations introduced, the system has *lower energy excitations* and it is energetically favourable to adopt a magnetic long-range ordered stucture (e.g. that of fig. 3.3 (b)) rather than being classically disordered at zero temperature (fig. 3.3 (a)). In the same paper it was also shown that site dilution (non-magnetic sites) selects the same ordered pattern, whence the name of "order by disorder". It is instructive, at this stage, to use the purely ferromagnetic example of the $J_1 - J_2$ model to explain more precisely why this exact magnetic

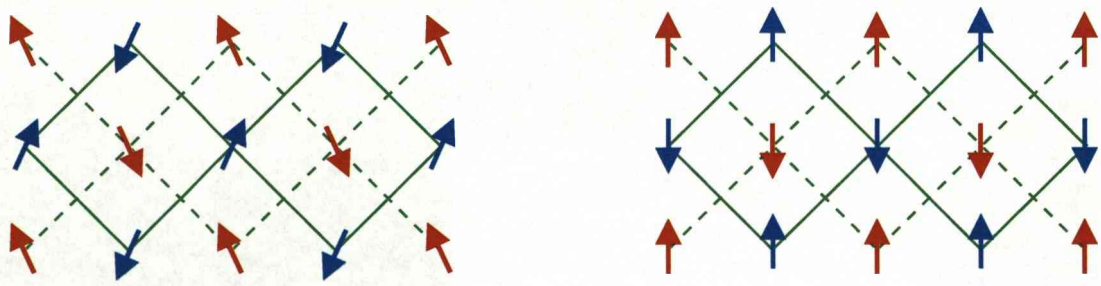

Figure 3.3: Spin structures on a square lattice for the case of $J_1 \ll J_2$ showing (a) two independent Néel sublattices with an infinite degeneracy for $J_1=0$, and (b) a collinear antiferromagnetic structure selected by quantum fluctuations by introducing an infinitesimal J_1.

structure is chosen naturally. This model (NN and NNN both ferromagnetic) can be thought of as two interpenetrating ferromagnetic sublattices. Here, zero-point motion is completely eliminated when the two sublattices are parallel, forming a pure (uniform) ferromagnet. In the antiferromagnetic case of interest, fluctuations can never be eliminated, but they are minimised in the configuration that is *maximally ferromagnetic*. This occurs when the spins along the x or y axes are ferromagnetically aligned. Fluctuations thereby select the collinear configurations [54].

Already in the 80's, Shender developed this "*order by disorder*" theory in explaining experimental data on the garnet $Mn_3Cr_2Ge_3O_{12}$ [55]. In his analysis, when fluctuations are taken into account, an exchange interaction appears between the spins of one sublattice via the other and couples the sublattices. A CAF structure follows from the fact that fluctuations at one site are orthogonal to the mean value of the magnetisation at that site and the system can gain some magnetic exchange energy by making such fluctuations coplanar on neighbouring sites, that is to making the spins collinear [48] as discussed above. Further experimentation continued by Brückel *et al.* [56–58], showed similar evidence for the dynamical

interaction between spin subsystems of the form of $(Fe_xGa_{1-x})_2Ca_3Ge_3O_{12}$, which are again decoupled garnets. In inelastic neutron scattering experiments this interaction was observed as a spinwave gap due to quantum fluctuations and as a splitting of the acoustical magnon branch. Such a selection of order by quantum fluctuations (and dilution) was also discussed by Henley [59], giving a collinear (and 'anticollinear', i.e. *least* collinear) magnetic ground state.

Frustration due to next-nearest neighbour exchange in a Néel or a collinear AF

We have so far discussed the limiting cases of $J_1 \gg J_2$ and $J_1 \ll J_2$, giving a NAF and a CAF respectively. Let us now briefly describe how frustration comes about in the square lattice of interest for $J_1 \gtrsim J_2$ and $J_1 \lesssim J_2$. Assume a Néel antiferromagnetic structure like that of fig. 3.4 (a) with the top left corner spin as 'up'. Its right NN is antiferromagnetically coupled to it in the 'down' state. Similarly, this latter spin will cause the one below it to be 'up'. From the diagram, we can already see that the two diagonal spins are *'frustrated'*, since the NNN interaction is antiferromagnetic but they are in the same 'up' state. For the CAF stucture of fig. 3.4 (b) with $J_2 > J_1$, the first interaction to satisfy would be the cross-bond exchange. The two spins in the middle column connected by the yellow solid line are again AF coupled obeying the interaction, but one is left with two spins in the same state (joined by the dashed line). These two NN are the frustrated spin pair in the case of a CAF. This frustration is exhibited throughout the whole lattice in both cases.

Generally, frustration describes a situation where in the ground state of a classical spin system not all interactions can be satisfied simultaneously. It is important to note here that *frustration in these square lattices comes purely from the NN-NNN competition*, and this is the kind of frustration that will be discussed.

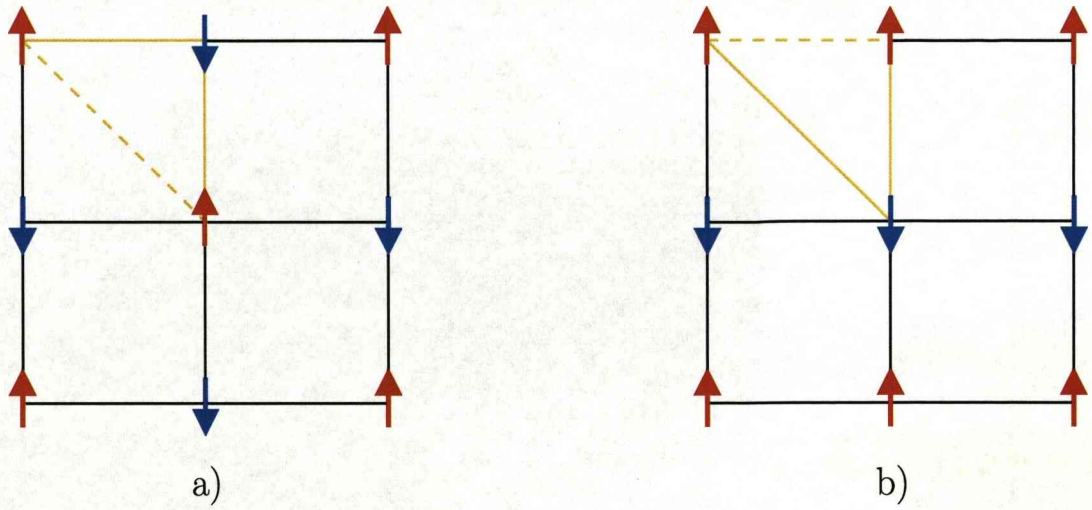

Figure 3.4: Spin frustration in a square lattice for (a) a Néel AF ($J_1 > J_2$) and (b) a collinear AF ($J_1 < J_2$). Continuous yellow lines are used for 'satisfied' spin pairs while dashed ones indicate 'frustrated' pairs.

Breakdown of magnetic long range order for $J_1 \sim J_2$

Let us now define the frustration parameter $\alpha \equiv J_2/J_1$, a quantity that can take values between 0 and ∞ when both NN and NNN are antiferromagnetic. It is useful in quantifying the degree of frustration for the various different phases that can occur in our model $J_1 - J_2$ system.

So far, we have not discussed the possibilities for intermediate phases between a CAF and a NAF ground state. Generally, a classical ordered state is stable against quantum fluctuations in higher dimensions. However, according to theoretical predictions for systems with lower dimensionality, the coexistence of quantum fluctuations and frustration tries to destabilise the classical ground state by producing a novel disordered state when the frustration effect is significant. Many approaches (including spin-wave theory [60, 61], numerical exact diagonalisations [62, 63], series-expansions [64–67], large N-methods [68], quantum Monte Carlo [69, 70], Ising and plaquette expansions, variational wave functions, cluster-effective-field approximations [71]...) have now firmly established that quantum

fluctuations destabilise the classically ordered ground state and lead it to a quantum disordered singlet one with a wavefunction $|\psi\rangle = \frac{1}{\sqrt{2}}(|\uparrow\downarrow\rangle - |\downarrow\uparrow\rangle)$ $(S = 0)$. We can simply understand why this formation of singlets would naturally occur in such a system by recalling that the energy of a singlet of two spins $\frac{1}{2}$ is $-3/4 \cdot J_1$ compared to the energy of two classical spins which is only $-1/4 \cdot J_1$ [48, 72]. Thus, the stability of this phase comes from the extreme stability of small $S = 0$ clusters and eventually from the fact that frustrated bonds between two different singlets do not contribute to the total energy.

The first-neighbour singlet, also called a *dimer* or a *valence bond* can cover the lattice in many ways, corresponding to different ground states of a *valence bond crystal* (VBC), see fig. 3.5. In a VBC, the simplest scenario for overcoming frustration, the pattern of singlets is regular. However, there is no long-ranged order in spin-spin correlations, but long-ranged order in dimer-dimer or larger singlet units exists. The coupling of this order to lattice distortions is probable in experimental realisations of spontaneous VBC. Furthermore, magnetic excitations of a VBC are generally thought to be gapped as opposed to gapless states for the NAF and CAF phases. In this simplest scenario, the translational and other spatial symmetries of the Hamiltonian are broken.

Alternatively, all symmetries can be restored in a flat superposition of local antiferromagnetic correlations (short range valence bond states) to form a so-called *spin liquid* (SL), shown in fig. 3.5 (f). The search for a true quantum SL - a quantum magnet which remains disordered at the very lowest temperatures - in dimensions greater than one has been central to research on quantum magnets for more than three decades.

Despite many years of numerical and analytical efforts, no definitive picture emerged around the maximally frustrated point $\alpha \sim 0.5$, where the magnetic order disappears. However, people seem to agree that there exists a second-order quantum transition from the Néel state into the spin liquid state at $\alpha \sim 0.34$, and

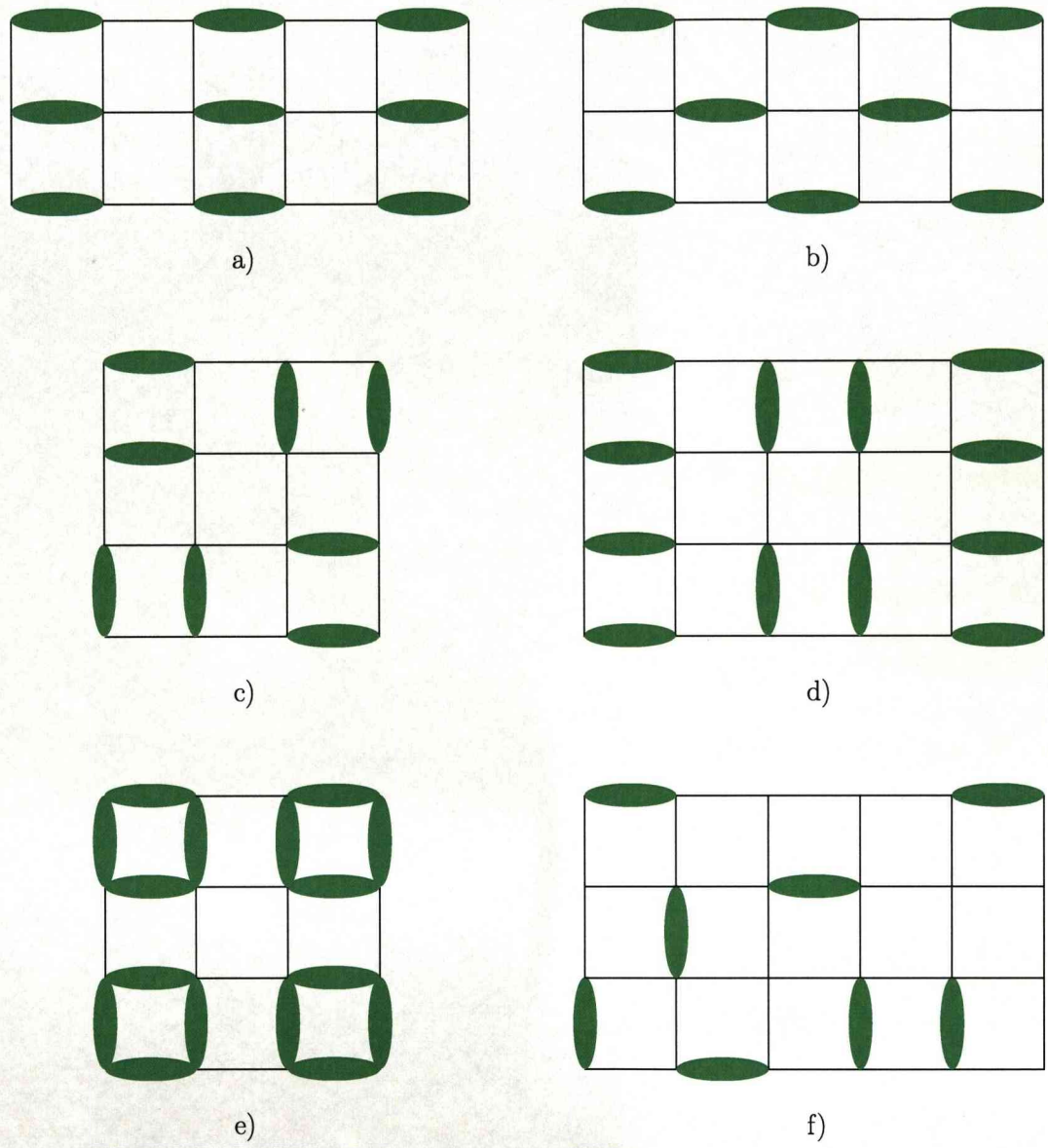

Figure 3.5: Dimer formations on a square lattice for $J_2/J_1 \sim 0.5$. Spin singlets shown in green are arranged to give (a) a columnar dimerised VBC when parallel dimers attract each other, (b) a staggered VBC when the system tries to minimise the number of parallel dimers, (c) a checkerboard structure and (d) a striped one. Part (e) shows a resonating plaquette VBC with 4-spin plaquettes (dimers) of $S = 0$ on alternating squares and finally (f) depicts a resonating valence bond, the true 'spin liquid' state.

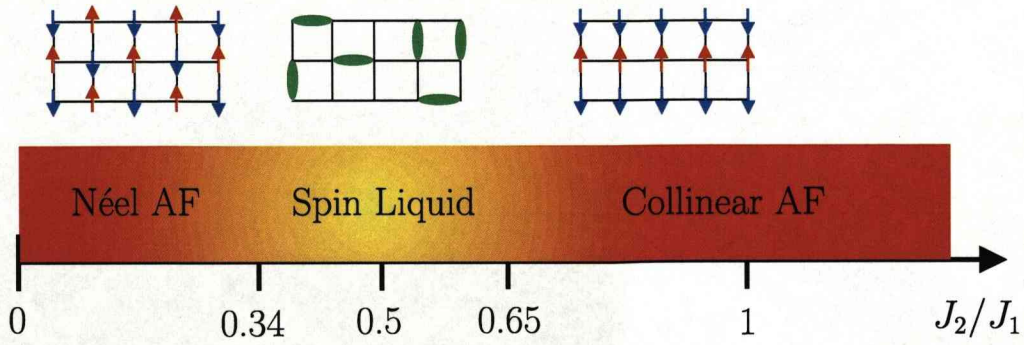

Figure 3.6: Generally "accepted" phase diagram for frustrated antiferromagnets. For low values of α - the frustration parameter - a NAF is predicted, followed by an intermediate SL phase before reaching the CAF structure and order by disorder. The shading represents the variation in the ordered moment.

a first-order transition from the spin liquid state to the collinear state at $\alpha \sim 0.65$. These are shown in fig. 3.6, the generally accepted phase diagram for frustrated antiferromagnets. Frustration parameter α is plotted along x, and starting from 0 we get a Néel AF which survives but with reduced sublattice magnetisation up to $\alpha \sim 0.34$. This is followed by a *spin liquid* state for maximum frustration, and finally a CAF for higher α's, reaching *order by disorder* when $\alpha \to \infty$.

One of the most common ideas in the field is the formation of a columnar spontaneous dimerised ground state for $\alpha \sim 0.5$ [64, 65]. Sushkov *et al.* [73] took these ideas further to predict a few more specific structures within the 'SL' phase of fig. 3.6. According to this work, there are two more second-order phase transitions. The system goes from a simple Néel state to a Néel state with superimposed spin columnar dimers, followed by a columnar dimerised spin liquid, a columnar dimerised structure with plaquette-type modulation and finally the collinear state at $\alpha \sim 0.34,\ 0.38,\ 0.5$ and 0.6 respectively.

However, generally speaking, the nature of the ground state in this intermediate region still remains an open question.

3.1.2 Generalisation of phase diagram to include ferromagnetic interactions

Nic Shannon *et al.* [74] came to stir the quantum waters of the square lattice phase diagram by including ferromagnetic interactions. In this fully generalised $J_1 - J_2$ model one can get any combinations of FM and AF interactions. The convention used here is positive J's for AF and negative J's for FM couplings. The new possibilities of a uniform ferromagnet ($J_1,\ J_2 < 0$) and a NAF and CAF with mixed ferro- and antiferromagnetic exhange couplings ($J_1 > 0,\ J_2 < 0$ and $J_1 < 0,\ J_2 > 0$ respectively) are shown in fig. 3.7. Panel a) shows a ferromagnet in which both NN and NNN are ferromagnetic. It is obvious that the NNN interaction does not compete with the NN one but on the contrary it reinforces the structure. Similarly for b), the Néel AF with AF NN and FM NNN interactions. There is no frustration here either, nearest and next-nearest neighbours are all satisfied and reinforce this Néel state. On the contrary, panel c) shows a frustrated collinear magnet with FM NN and AF NNN interactions, hereafter referred to as simply a *frustrated ferromagnet*. Frustration occurs since by satisfying the NN and NNN interactions of the top left spin 'up', we are left with a frustrated NN bond as shown in fig. 3.7 (c).

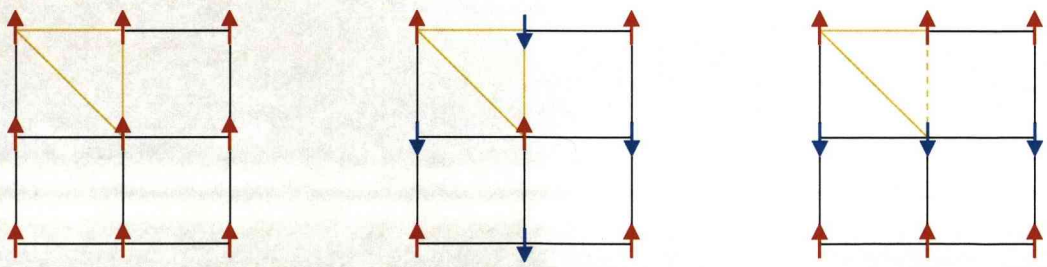

Figure 3.7: Spin frustration and satisfaction in a square lattice for (a) a uniform FM ($J_1,\ J_2 < 0$), (b) a NAF with $J_1 > 0$ and $J_2 < 0$ and (c) a frustrated FM with $J_1 < 0$ and $J_2 > 0$. Continuous yellow lines are used for 'satisfied' spin pairs while the dashed one indicates a 'frustrated' pair.

Since the properties of the $J_1 - J_2$ model depend on the relative and not the absolute size of the exchange couplings J_1 and J_2, it is convenient to introduce two parameters to characterise it, namely an overall energy scale J_c and a frustration angle ϕ defined by

$$J_c = \sqrt{J_1^2 + J_2^2} \quad \text{and} \quad \phi = \tan^{-1}(J_2/J_1), \tag{3.2}$$

such that $J_1 = J_c \cos\phi$, and $J_2 = J_c \sin\phi$. The three phases (NAF, CAF and FM) under this scheme are given in fig. 3.8, where J_1 and J_2 are plotted along the x and y-axes. In addition to the known spin liquid region for $J_1 > 0$, $J_2 \sim J_1/2$, where the NAF and CAF phases compete, a new spin liquid region may exist for $J_1 < 0$, $J_2 \sim -J_1/2$, where the FM and CAF phases compete, due to symmetries of the Hamiltonian [74]. The phase transition between the FM and NAF is straightforward, without going through an intermediate phase.

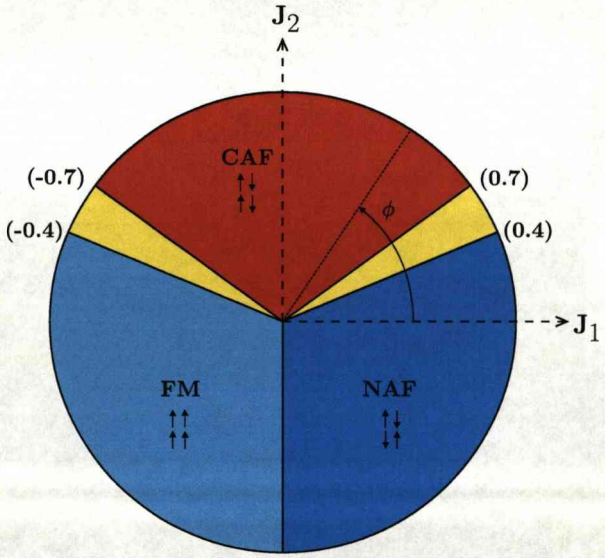

Figure 3.8: Classical phase diagram for the general $J_1 - J_2$ model [74]. The numbers are J_2/J_1 for phase boundaries determined from the classical ground state energy. At these values, zero-point fluctuations destroy the relevant order parameter [75]. The yellow areas for $J_1 > 0$ correspond to the known spin-liquid regime, and for $J_1 < 0$ to a new spin-liquid region.

3.2 Experimental procedure

Li_2VOSiO_4 and $Pb_2VO(PO_4)_2$ powders were grown by Enrique Kaul (m=26.078 g and 91.962 g respectively), while $SrZnVO(PO_4)_2$ by Ramesh Nath (m=45.62 g) at the Max-Planck Institute for Chemical Physics of Solids in Dresden, by the solid state reaction method. In this method the reagents are in powder form, do not melt, and the reaction takes place through diffusion between the grains at high temperatures. This synthesis technique was used in order to avoid multi-phase composition for these compounds [76].

The neutron scattering experiments were performed on D7 and IN20 at ILL, using full polarisation analysis to get the purely magnetic signal.

For the D7 experiments, $Pb_2VO(PO_4)_2$ and $SrZnVO(PO_4)_2$ were mounted in a cylindrical 25 mm diameter aluminium container with a height of about 8 cm as shown in fig. 3.9. The incident wavelength used was $\lambda = 3.1$ Å and the neutron beam's transmission was 0.87 and 0.62 for the two compounds respectively. Li_2VOSiO_4, being highly absorbing, was placed within two aluminium concentric cylinders of 17 and 25 mm. This geometry gives higher transmission than a full cylinder (T=0.39 in this case). In all cases, a cadmium cap on top of the sample container was used in order to absorb neutrons and reduce Al Bragg scattering. A closed-circuit refrigerator (2.7K<T<300K) and a standard ILL orange cryostat (1.5<T<300K) were used to control the temperatures. The magnetic ground states were measured at the base temperature of 1.5K (below T_N in all cases) and the magnetic form factors at room temperature. Further measurements for $Pb_2VO(PO_4)_2$ and $SrZnVO(PO_4)_2$ at 20K and 35K respectively, revealed short-range spin correlations.

The $Pb_2VO(PO_4)_2$ was also studied at IN20, mounted in the same way in an orange cryostat. A Heusler monochromator and analyser were used for PA, and a cylindrical ^{3}He detector for the data collection. The spectrometer was used in the W configuration, with fixed final wavevectors of $k_f = 2.662$ Å^{-1} and 4.1 Å^{-1}.

Figure 3.9: $SrZnVO(PO_4)_2$ powdered sample in an aluminium can ready to be measured.

The bulk magnetisations of $Pb_2VO(PO_4)_2$ and $SrZnVO(PO_4)_2$ powders were measured using a SQUID magnetometer at the University of Liverpool. They were placed in a completely symmetric cylindrical non-magnetic container especially made for these measurements with high precision by Keith Williams from the University of Liverpool. The Automatic Background Subtraction method (ABS) was used to remove the diamagnetic component of the sample holder in order to get clearer and more accurate results, since these spin-half systems are weak and dilute (only 1 in 14 atoms is magnetic). The key to using the ABS feature is identifying the centre position of the sample in the sample holder before performing the actual sample measurement. In order to do so, we performed a centering scan on a stainless steel sample (with high moment), which was located at the expected position of the sample. Then, by removing this surrogate, the sample holder background response was collected and stored to be subtracted later from the sample measurement response [77], giving much more accurate results.

3.3 Results

3.3.1 $Pb_2VO(PO_4)_2$

This compound was discovered and grown by Cristoph Geibel and Enrique Kaul, as a result of search for new magnetic $J_1 - J_2$ materials. It forms a predominantly 2D structure with magnetic properties typical of frustrated 2DQHAF.

Structure

Dilead vanadium oxide bis(phosphate) ($Pb_2VO(PO_4)_2$) crystallises in the monoclinic system with spacegroup $P2_1/a$ and lattice parameters $a = 8.747(4)$ Å, $b = 9.016(5)$ Å, $c = 9.863(9)$ Å and $\beta = 100.96(4)°$ [76, 78]. Because of the low symmetry of this structure four formula units are contained in one unit cell (Z=4). Three projections of the $Pb_2VO(PO_4)_2$ structure are shown in fig. 3.10. The structure contains corrugated layers formed by VO_5 square pyramids oriented in alternating directions in a chessboard fashion. The pyramids are connected by tetrahedral PO_4 groups. The waves in the layers propagate along the *b-axis*. The square bases of the similarly oriented pyramids are located approximately at the same level. The magnetic [$VOPO_4$] layers are well separated (~10Å) by non-magnetic Pb atoms and isolated PO_4 tetrahedra, indicating a quasi-2D character for the system. It is interesting to note here that the most likely reason for corrugation of the layers is the presence of these extra PO_4 tetrahedra between them. As we will see later, in the Li_2VOSiO_4 structure [41], adjacent [$VOSiO_4$] layers with a similar type of polyhedral linkage are flat, since they are separated only by Li^+ cations (see fig. 3.23). In this compound the vanadium ion is in the oxidation state 4+, implying a d^1, S=1/2 magnetic configuration. The V^{4+} cation is coordinated by five O anions, forming a slightly distorted square pyramid. A short V-O distance [$\sim$ 1.56 Å] (this O is the apical one) indicates the existence of a vanadyl bond, while the other four oxygen ions form the basal plane of the pyramids and

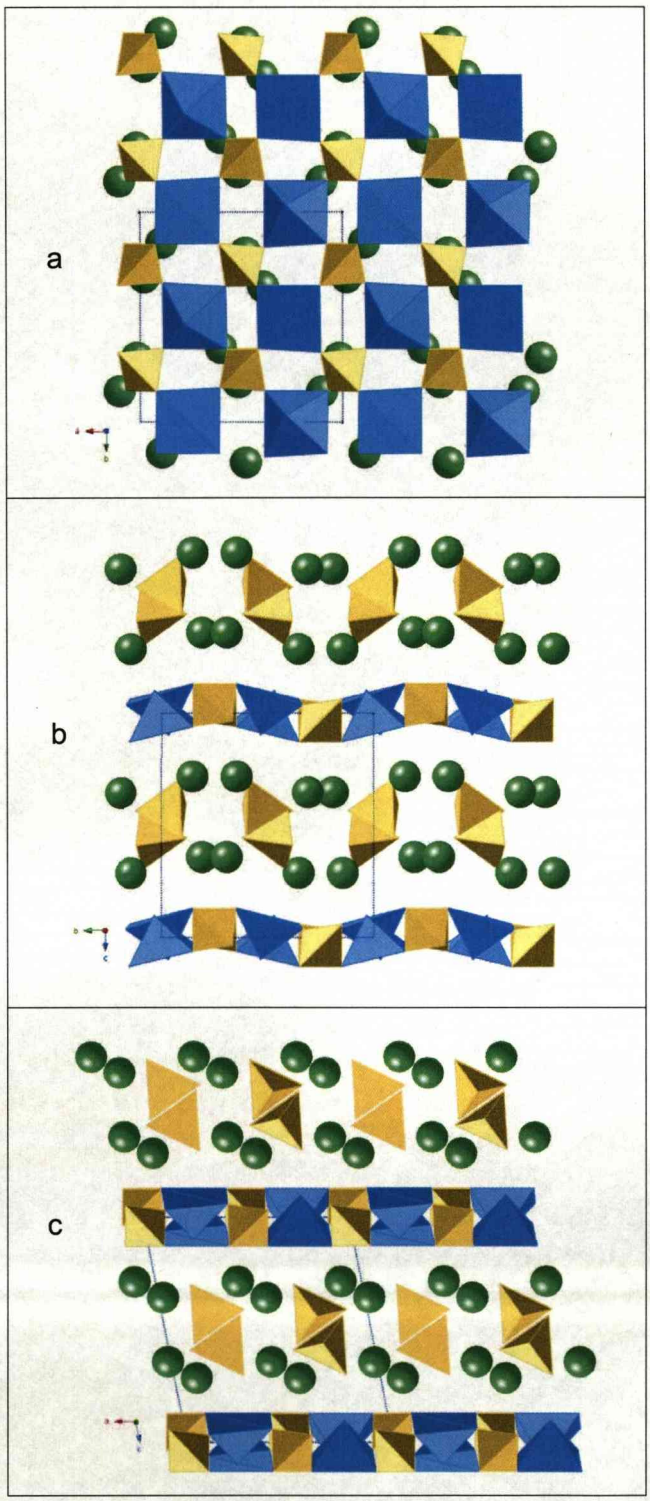

Figure 3.10: The structure of $Pb_2VO(PO_4)_2$ contains corrugated layers formed by VO_5 square pyramids (blue), oriented in alternating directions in a chessboard fashion. The pyramids are connected by tetrahedral PO_4 groups (yellow). The layers are separated by the Pb atoms (green) and isolated PO_4 tetrahedra. Projections shown are along the a) *ab*, b) *bc* and c) *ac* planes.

are situated at the typical distance of about 2 Å from the vanadium [76, 78].

Magnetic susceptibility

In general, the compounds presented in this chapter exhibit quasi-two-dimensional behaviour. The exchange constants are relatively small with typical strengths of the order of 10 K. For this reason the magnetic properties as measured in the SQUID are characterised by a paramagnetic high temperature behaviour, followed by an intermediate region in which χ(T) develops a round maximum characteristic of low dimensional materials [76]. As we will see, this is due to short range correlations appearing at temperatures of the order of the magnetic superexchange energies. At lower temperatures below this maximum, all the compounds undergo a magnetic phase transition towards an ordered state.

The bulk magnetic properties of $Pb_2VO(PO_4)_2$ were obtained using the Liverpool SQUID magnetometer. The polycrystalline sample was measured under an applied field of 1000 Oe and in the temperature range 1.7 K<T<400 K, giving the results of fig. 3.11. For T>50 K, χ(T) is characterised by a paramagnetic Curie-Weiss (CW) behaviour. Below that, χ(T) deviates from it passing through a broad maximum at $T_{\mathrm{Max}} \sim 8.5$ K and decreases towards a finite value at lower temperatures. The good quality of the sample is evidenced by the absence of any trace of an impurity tail at the lowest attainable temperatures, which is typical of paramagnetic foreign phases. A kink in χ(T) indicates the onset of magnetic ordering at the Néel temperature $T_{\mathrm{N}} \sim 3.7$ K (fig. 3.11 a). This temperature can be seen more clearly by plotting $\partial\chi/\partial T$ (T) as in fig. 3.11 b. The temperature of the maximum in χ(T), T_{Max}, has been taken as the temperature at which $\partial\chi/\partial T = 0$. The error bars in fig. 3.11 a) are not plotted, being smaller than the points themselves, although they are magnified in taking $\partial\chi/\partial T$ as seen in fig. 3.11 b. The errors are greater around the boiling point of ^{4}He, since the equipment cannot stabilise its temperature very well in this range.

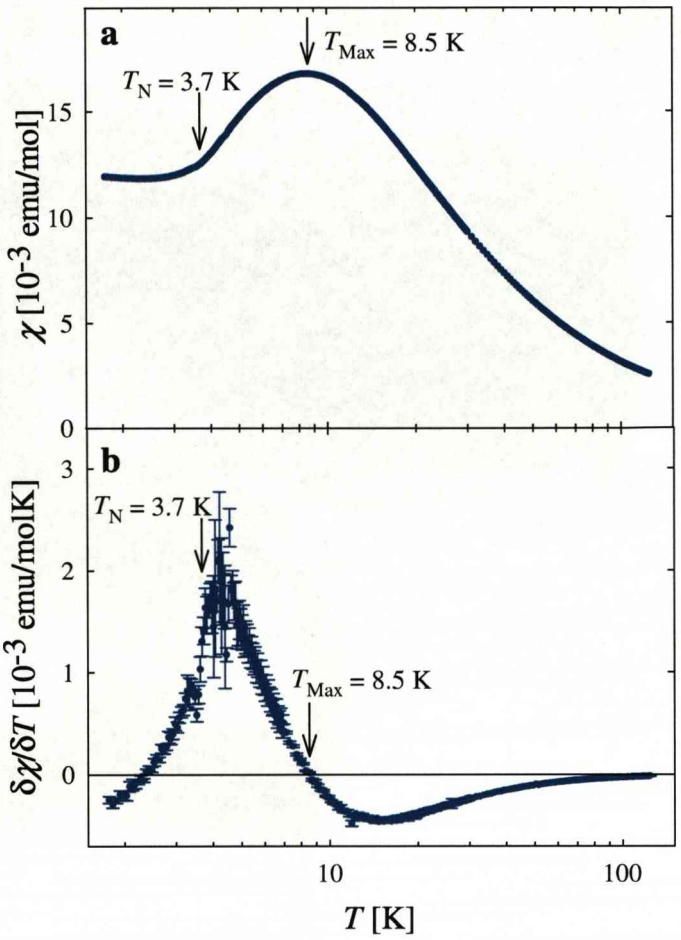

Figure 3.11: Magnetic response of polycrystalline $Pb_2VO(PO_4)_2$ as measured at 1000 Oe. Part (a) shows χ(T) characteristic for a low-dimensional spin system while (b) is the differential $\partial\chi/\partial T$ (T). The magnetic phase transition at T_N manifests as a change of slope in χ(T). T_{Max} indicates the approximate energy scale for this 2-D system.

The high-temperature data can be fitted according to the Curie-Weiss law:

$$\chi^{-1}(T \to \infty) = \frac{T + \theta_{CW}}{C}, \tag{3.3}$$

where θ_{CW} is the Curie-Weiss temperature. A fit for $T > 50$ K, shown as the red line on top of the data in fig. 3.12, gives $\theta_{CW} = (4.5 \pm 1)$ K (in our convention a FM has a negative θ_{CW}, while an AF a positive one). This value of θ_{CW} is rather

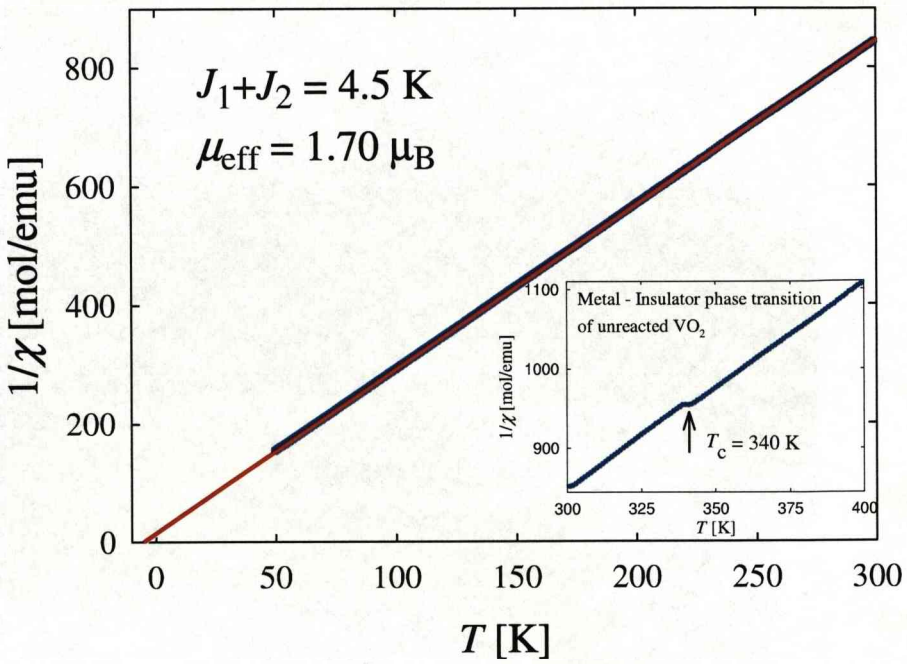

Figure 3.12: Inverse susceptibility of polycrystalline $Pb_2VO(PO_4)_2$ for $T > 50$ K, together with the Curie-Weiss law fit (red line), giving $\theta_{CW} = (4.5\pm1)$ K. The inset shows a metal-insulator phase transition at $T_c \simeq 340\ K$ for unreacted VO_2, observed as a step in χ^{-1}(T).

small compared to $T_{Max} \sim 8.5$ K. In the case of the unfrustrated two-dimensional Heisenberg square lattice antiferromagent, the temperature of the maximum in χ(T) is directly related to the magnetic exchange as $T_{Max} \simeq J_{2D}$ [76,79]. However, in our 2DQHAF system, mean-field theory gives $\theta_{CW} = J_1 + J_2$ [80]. This is simply what one might expect from a bulk magnetisation measurement - to give the sum of all the interactions in the system - not being able to distinguish symmetries in the crystal or powder. The fact that θ_{CW} is smaller than T_{Max} - which reflects the overall energy scale of the system J_c - suggests that J_1 and J_2 have opposite signs. Therefore, this preliminary analysis of $Pb_2VO(PO_4)_2$ seems to offer evidence of mixed ferro- and antiferromagnetic exchange couplings. These physical results were originally observed by E. Kaul [76] and formed the basis for the theoretical work of N. Shannon *et al.* [74].

From the susceptibility measurement, one can also get the effective moment of the magnetic ions according to:

$$\mu_{\text{eff}} = \left(\frac{3k_{\text{B}}}{\mu_0 N_{\text{A}} \mu_{\text{B}}^2}\right)^{1/2} \sqrt{\chi_{\text{m}} T} = 2.827\sqrt{\chi_{\text{m}} T} \tag{3.4}$$

where in the second step μ_{eff} is measured in Bohr magnetons per formula unit and χ_{m} in emu/mol (cgs units). $\chi_{\text{m}}T$ is simply the slope of the inverse susceptibility plot (fig. 3.12) and by inserting it into eq. (3.4) we get $\mu_{\text{eff}} = (1.70 \pm 0.02)\ \mu_{\text{B}}$.

The Landé g-value can now be calculated from the relationship (using the same units for the effective moment):

$$g_{\text{J}} = \frac{\mu_{\text{eff}}}{\sqrt{J(J+1)}} \tag{3.5}$$

which yields $g_{\text{J}} = 1.96 \pm 0.03$ for this compound. These results are consistent with an $S = 1/2$ (and $L = 0$) system, expected to give $g_{\text{J}} = 2$ and $\mu_{\text{eff}} = 1.73\ \mu_{\text{B}}$.

Another important point is the observation of a step in the susceptibility at $T_{\text{c}} \simeq 340$ K, shown in the inset of fig. 3.12. This originates from the presence of a small amount of unreacted VO_2 and relates to a well known structural phase transition from a high-temperature paramagnetic rutile structure to a low-temperature monoclinic one. This structural transition is also accompanied by a metal (above T_{c}) to insulator (below T_{c}) transition. There has been a lot of interest since the late 50's in this area which still is an active topic of current research. These early experiments included conductivity, pressure and x-ray diffraction measurements [81–85] on various vanadium oxides. This Metal-Insulator transition is a generally observed phenomenon in TM oxides and relates fundamentally to the structure of the crystal as well as the magnetic ion. Its electronic configuration (or oxidation state) seems to determine the exact value of T_{c}. Experimental data for a few transition-metal compounds as well as suggested mechanisms for this effect are reviewed in [86].

Neutron measurements

In this section neutron results from the D7 and IN20 instruments at the ILL are presented in a 'natural' to follow order, starting from the magnetic form factor, then continuing with the ground state and finally the short-range spin correlations of this system.

- ***Magnetic form factor of V^{4+}***

At room temperature (RT), in the true paramagnetic phase of this system, the V^{4+} ions point in random directions (no magnetic correlations). This happens because the magnetic moments of the unpaired $3d$ electrons on neighbouring V atoms are completely uncoupled to each other due to the existence of strong thermal fluctuations of the order of kT. The scattering in this case can be simply understood as the F.T. of these unpaired electrons.

The occurence of the form factor f determining the *magnetic* scattering, in contrast to the absence of any such factor for the *nuclear* scattering, arises since the electrons which determine the magnetic moment are distributed over a volume of space comparable with the neutron wavelength. Thus this form factor is somewhat similar to the electronic form factor of an atom for x-ray scattering. Nevertheless, the two are by no means identical since only a few electron orbits in an outer unfilled shell of the atom contribute to the magnetic moment and, hence, to the form factor f for the magnetic scattering of neutrons. Therefore, the form factor for magnetic neutron scattering is found to fall off more rapidly with angle than the factor for x-ray scattering [20].

This q-dependence of the magnetic neutron scattering cross section in this paramagnetic state was measured at D7, giving the experimental data of fig. 3.13. A simple Gaussian of the form $Ae^{(-Q^2/2\sigma^2)}$ with $\sigma = 1.805$ Å^{-1} is shown as the red curve on the same plot and was used to describe and model the lower temperature data for both $Pb_2VO(PO_4)_2$ and $SrZnVO(PO_4)_2$ powders.

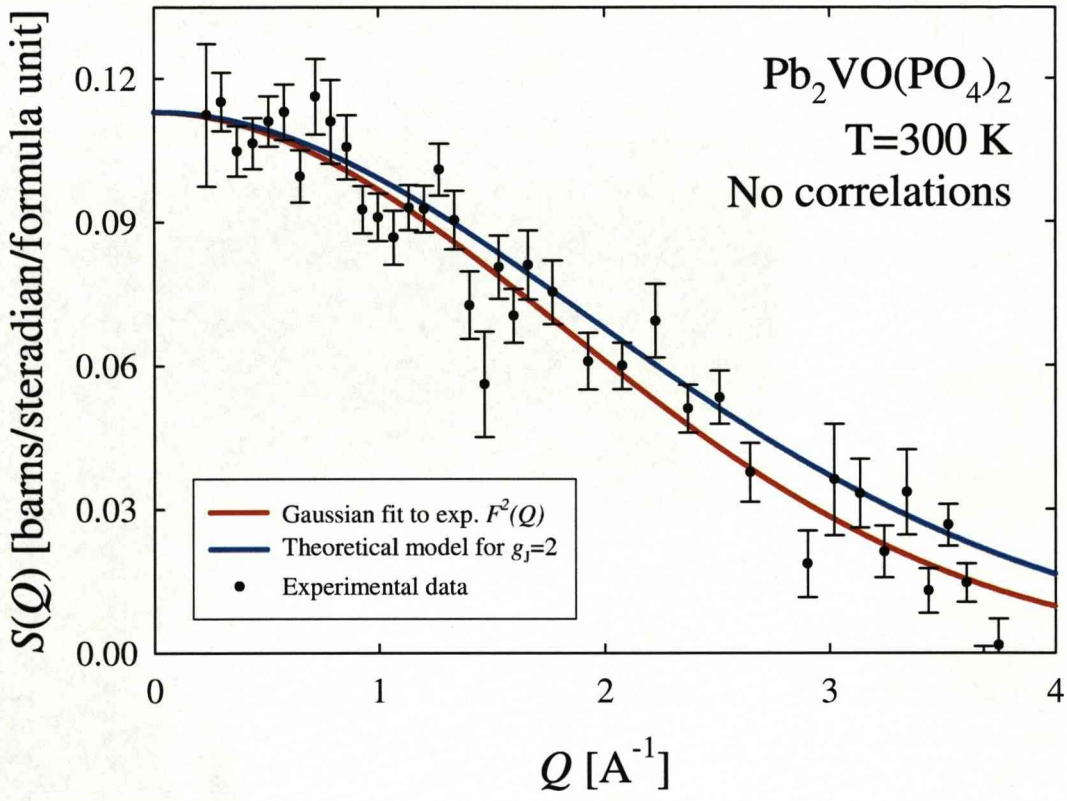

Figure 3.13: Paramagnetic neutron scattering cross section of $Pb_2VO(PO_4)_2$. The red curve is a simple Gaussian fit while the blue one is an analytical calculation of what is expected for the V^{4+} ion form factor.

This V^{4+} form factor can be analytically calculated according to:

$$F^2(Q) = \langle j_0 \rangle^2(Q) \text{ where } \langle j_0 \rangle(Q) = Ae^{-a\left(\frac{Q}{4\pi}\right)^2} + Be^{-b\left(\frac{Q}{4\pi}\right)^2} + Ce^{-c\left(\frac{Q}{4\pi}\right)^2} + D \quad (3.6)$$

assuming the simplest scenario of spin-only scattering ($g_J = 2$). $\langle j_0 \rangle$ is a function of the momentum transfer Q (measured in $Å^{-1}$) which describes the radial distribution of spin and current densities. Note that $F^2(Q)$ does not depend on the direction of the scattering wavevector Q but only on its magnitude. By substituting the values of the constants A, B, C, D, a, b, c, tabulated in [87], we get the blue curve of fig. 3.13. These two fits to the magnetic form factor are consistent to each other within the statistical error bars of this measurement.

- ***Magnetic ground state***

Below T_N, the magnetic moments of the individual V^{4+} ions are oriented in a defined manner since magnetic interactions become dominant over the kT term (in contrast with their random orientation in space for the paramagnetic phase). In this magnetically ordered system there is *coherence* between the neutrons scattered by the magnetic ions, giving rise to the build-up of coherent diffraction peaks dependent on the two-dimensional magnetic structure.

Fig. 3.14 shows the magnetic ground state diffraction pattern of $Pb_2VO(PO_4)_2$, consisting of sharp magnetic Bragg reflections on top of a diffuse magnetic background. Data were collected at 1.5 K within a few hours and were modelled by both a collinear antiferromagnetic structure (fig. 3.14 a) and a Néel structure (fig. 3.14 b) according to:

$$I(Q)_{\text{calc.}} = \frac{2}{3}(\gamma r_0)^2 \mu_{\text{ord.}}^2 F^2(Q) \left| \sum_j \boldsymbol{S}_j e^{-\mathrm{i}\boldsymbol{Q}\cdot\boldsymbol{r}_j} \right|^2 L_{\text{powder}} \frac{1}{N} \frac{\sigma_{\text{Li}}^{\text{struct.}}}{\sigma_{\text{Li}}^{\text{magn.}}} + \alpha F^2(Q) \quad (3.7)$$

where $\gamma = 1.913$, r_0 is the classical radius of the electron, $\mu_{\text{ord.}}$ is the ordered component of the magnetic moment of the ions and $F^2(Q)$ is the magnetic form factor. The summation is across all V^{4+} ions j with spin $\boldsymbol{S}_j$ and position vector $\boldsymbol{r}_j$ within the magnetic unit cell (geometrical magnetic structure factor), and this is where we can select the type of ordering [(π, π) NAF and $(\pi, 0)$ or $(0, \pi)$ CAF].

$$L_{\text{powder}} \propto \frac{1}{\sin^2\theta \cos\theta} \quad (3.8)$$

is a term known as the Lorentz factor (for powders in this case), relating the geometrical structure factor of the magnetic (or structural) Bragg peaks to the integrated intensity obtained experimentally. This calculation (eq. 3.7) has to be normalised overall with the experiment due to the fact that the structure factor calculation of the integrated magnetic intensities (generated by a *fortran*

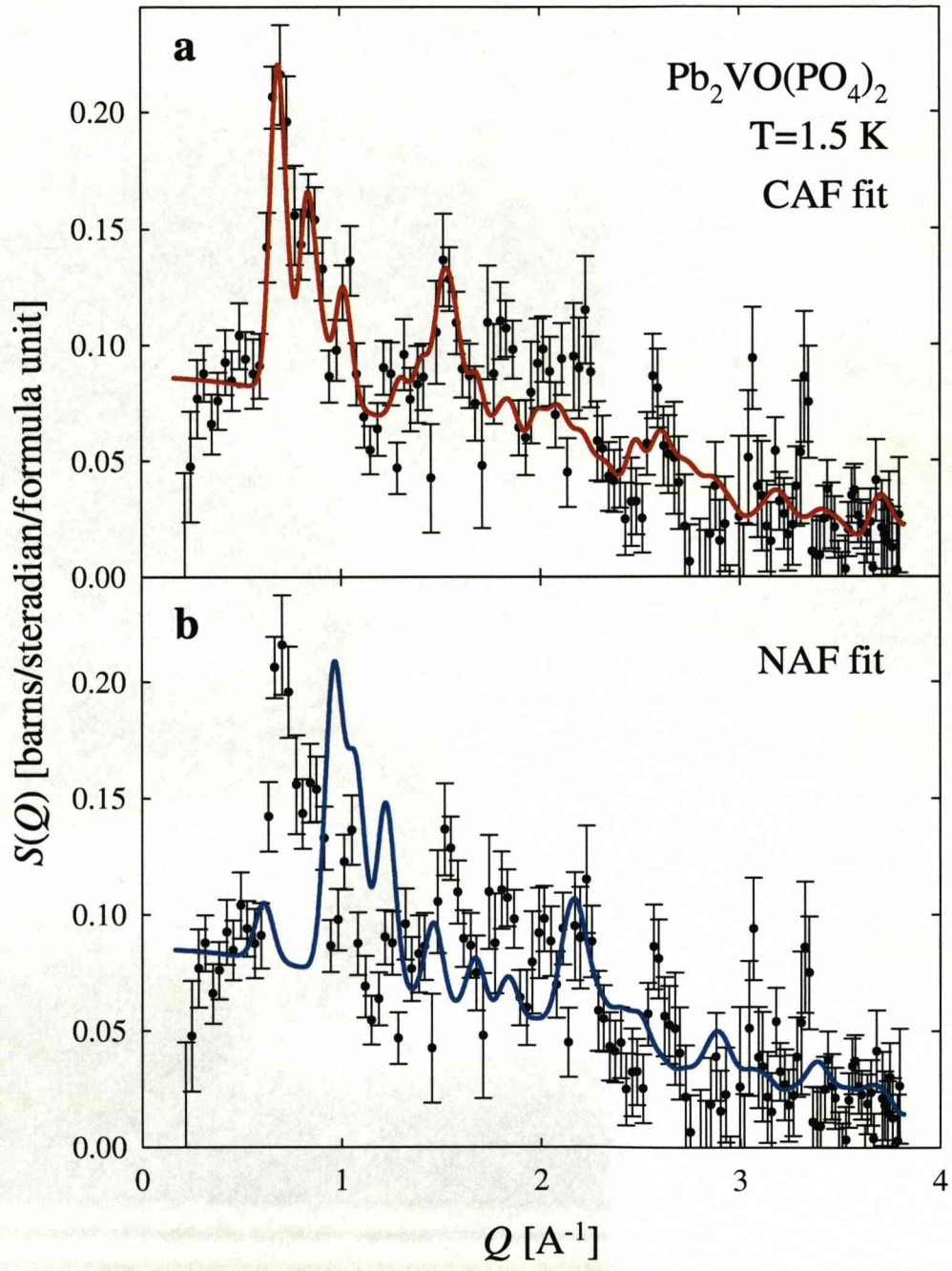

Figure 3.14: Magnetic ground state diffraction pattern of $Pb_2VO(PO_4)_2$ measured at 1.5 K. The ordered component of the ions' moments gives rise to sharp magnetic Bragg reflections, while the disordered component gives a diffuse background. The reduced ordered moment of $\sim$ 0.5 μ_B together with the diffuse background indicate presence of quantum disorder. Part (a) shows a CAF model with an ordering wavevector of $\boldsymbol{Q} = (\pi, 0)$, giving the best fit to the data. For comparison, the Néel ground state model is shown in part (b).

code) has arbitrary units while the experimental cross-section is measured in barns/steradian/formula unit. By using the $Pb_2VO(PO_4)_2$ structural data - measured at the same time as the magnetic data and displayed in a different channel on the D7 instrument - and by running a separate structure factor calculation for the nuclear scattering cross section (as shown in section 3.3.3) we were able to deduce $N \sim 213$ in this case. However, this normalisation is not enough for this system, since it only accounts for the height of the peaks. In comparing integrated intensities one needs to equally worry about the widths of the peaks from a scattering point of view (due to the crystallite quality for example) as well as the instrumental resolution. For these compounds we observed a larger width for the magnetic peaks compared to the nuclear ones. The Li_2VOSiO_4 measurement was used as the standard one for this type of normalisation for all compounds since it has a much simpler structural and magnetic diffraction pattern, giving hence more accurate results for the widths (see section 3.3.3). The values used are $\sigma_{\mathrm{Li}}^{\mathrm{struct.}} = 0.0241$ Å^{-1} and $\sigma_{\mathrm{Li}}^{\mathrm{magn.}} = 0.0398$ Å^{-1}. Finally, the last term in eq. (3.7) is a fraction α of the form factor used in fitting the diffuse magnetic background.

From simply inspecting fig. 3.14 one can see the agreement of the experiment with the theoretical calculation for a CAF structure as shown in part (a). The ordering wavevector for this best fit is $\boldsymbol{Q} = (\pi, 0)$, otherwise referred to as a CAF with a modulation along the $a-axis$. Shown in part (b) is the Néel antiferromagnetic model for comparison. Clearly, this does not reproduce the experimental data adequately, failing to descibe the magnetic Bragg peaks.

From the CAF fit the value of the ordered moment comes out as $\mu_{\mathrm{ord.}} = (0.50 \pm 0.04)\ \mu_{\mathrm{B}}$, an interesting result in its own right. This reduced moment, together with the considerable amount of diffuse scattering at this temperature coming from the disordered component of the moment is an indication of the presence of *quantum disorder*.

- ***Spin correlations***

In a neutron scattering experiment, the quantity of interest usually measured is the *scattering function* of the system $S(\boldsymbol{Q},\omega)$. It is also referred to as the *dynamical structure factor* since it incorporates temporal information, and it should not be confused with the *geometrical structure factor* as discussed in the previous section. $S(\boldsymbol{Q},\omega)$ is the Fourier transform of the "time-dependent pair-correlation function" $G(\boldsymbol{r},t)$ which is a function of space and time, and is entirely determined by the system itself without reference to any properties of the neutrons. The zeroth energy moment of $S(\boldsymbol{Q},\omega)$ is given by:

$$S(\boldsymbol{Q}) = \int_{-\infty}^{\infty} S(\boldsymbol{Q},\omega)\mathrm{d}(\hbar\omega) \tag{3.9}$$

and is known as the "static structure factor". Note that for powders, $S(\boldsymbol{Q})$ depends only on $|\boldsymbol{Q}|$.

Exchange constants are usually determined via the excitations from the ordered phase. However, the large single-crystal samples required for inelastic neutron scattering experiments were not available for any of these compounds. The novelty in our approach was to model $S(Q)$ in polycrystalline materials by using high-temperature series expansion (HTSE) of the dynamic susceptibility. This very important concept forms the core of the measurements and analysis for these 2DQHAF systems. In the determination of the NN and NNN exchange constants we used the 1^{st} order HTSE given by:

$$S(\boldsymbol{Q}) \sim S(S+1)\left[1 + \frac{S(S+1)}{3}\cdot\frac{J(\boldsymbol{Q})}{\mathrm{k}T}\right]\cdot F^2(Q) \tag{3.10}$$

where S is the spin of the magnetic ions, $F^2(Q)$ the usual magnetic form factor of the individual magnetic ions and

$$J(\boldsymbol{Q}) = \sum_l J(\boldsymbol{R}_l) e^{i\boldsymbol{Q}\cdot\boldsymbol{R}_l} \tag{3.11}$$

is the F.T. of the exchange interactions. In this summation, for the case of these frustrated 2D systems, the index l runs over all nearest and next-nearest neighbouring ions at position vectors $\boldsymbol{R}_l$ around a central atom, as shown in fig. 3.15. The interactions are taken as J_1 or J_2 for NN and NNN respectively. The resulting expression evaluated for these 8 nearest and next-nearest neighbours is:

$$J(\boldsymbol{Q}) = 2J_1[\cos(2\pi h) + \cos(2\pi k)] + 2J_2\{\cos[2\pi(h+k)] + \cos[2\pi(h-k)]\} \tag{3.12}$$

where h and k are reciprocal lattice indices of the 2D square lattice. In order to compare with powder measurements, we used spherical polar co-ordinates to calculate the intensity of $S(\boldsymbol{Q})$ (eq. 3.10) as a function of $|\boldsymbol{Q}|$.

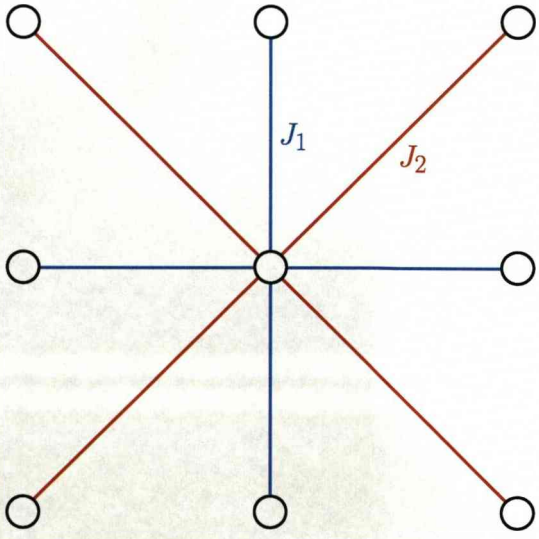

Figure 3.15: Square lattice of magnetic ions used in evaluating the F.T. of the exchange interactions $J(\boldsymbol{Q})$. The summation is taken around the central atom for all nearest and next-nearest neighbours.

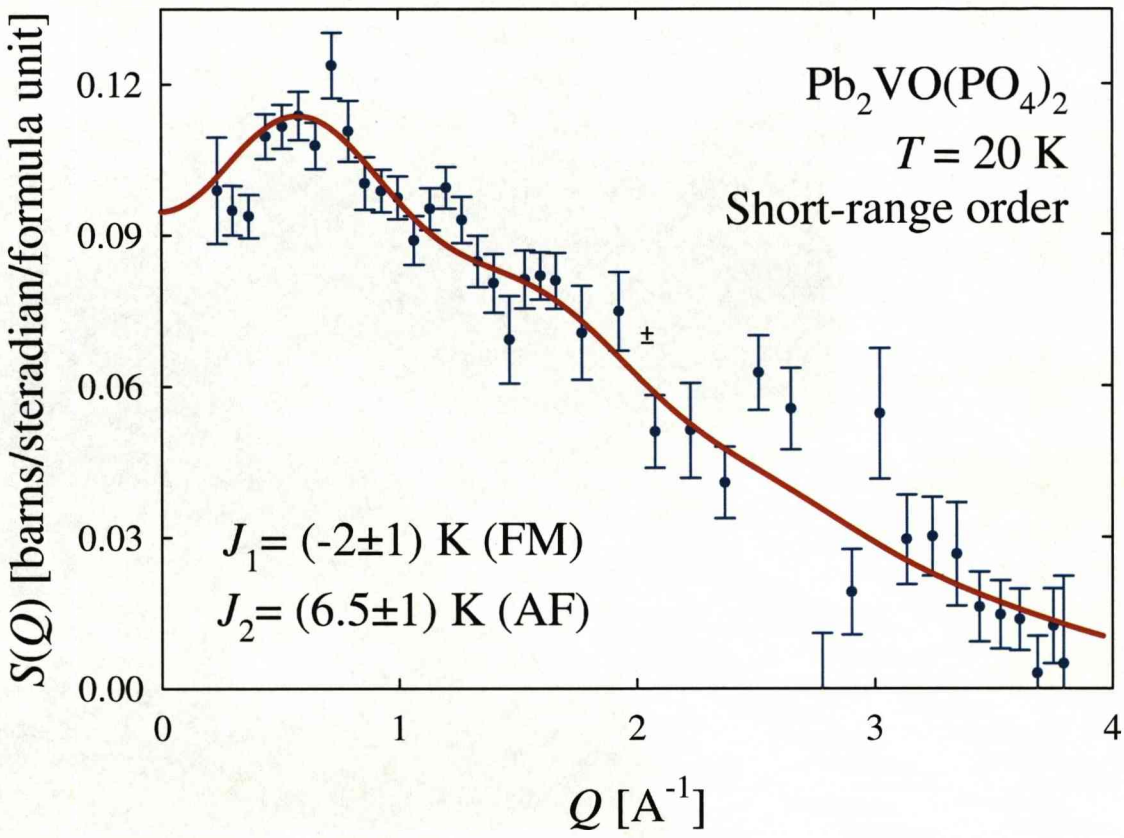

Figure 3.16: Short-range spin correlations in the paramagnetic phase of $Pb_2VO(PO_4)_2$. The red curve is a first-order HTSE calculation yielding ferromagnetic $J_1 \sim (-2 \pm 1)$ K and antiferromagnetic $J_2 \sim (6.5 \pm 1)$ K.

Fig. 3.16 shows the diffuse neutron scattering intensity at $T = 20$ K, a temperature well into the paramagnetic phase for this compound. Although magnetic long range order has been destroyed at this temperature, the kT term has not completely washed out all magnetic interactions. The presence of oscillations in the data indicates the existence of short-range spin correlations.

Given the constraint from the magnetic susceptibility measurement $\theta_{\rm CW} = 4.5$ K, we are able to determine the individual values of J_1 and J_2 by modelling these spin correlations in the paramagnetic phase. The solid line in fig. 3.16 shows a high-temperature series expansion of the spin correlations at $T = 20$ K. Best agreement with the data is obtained for ferromagnetic $J_1 \sim (-2 \pm 1)$ K and

antiferromagnetic $J_2 \sim (6.5 \pm 1)$ K ($\chi^2 = 1.66$ for this model compared with $\chi^2 = 2.34$ for no correlations). Combining these in eq. (3.2) we get the overall energy scale of the system $J_c \sim 6.8$ K. Thus $T \sim 3J_c$ and, therefore, we are justified in taking the first-order HTSE (eq. 3.10) as a valid approximation to model the diffuse scattering from these short-range correlations.

Further to these measurements, the energy excitations of this system were explored using the triple-axis instrument IN20 at the ILL. Scans of energy transfer were performed at fixed reciprocal lattice points Q and at a few temperatures T. A typical measurement is shown in the energy scan of fig. 3.17. For all points Q in reciprocal space, the excitations are found to be within $\sim \pm 4$ meV, and the system's energy scale is indeed low. Hence, we were able to properly integrate over energy transfer in measuring $S(Q)$ (see eq. 3.9) using D7 since this instrument has an energy window up to 10 meV.

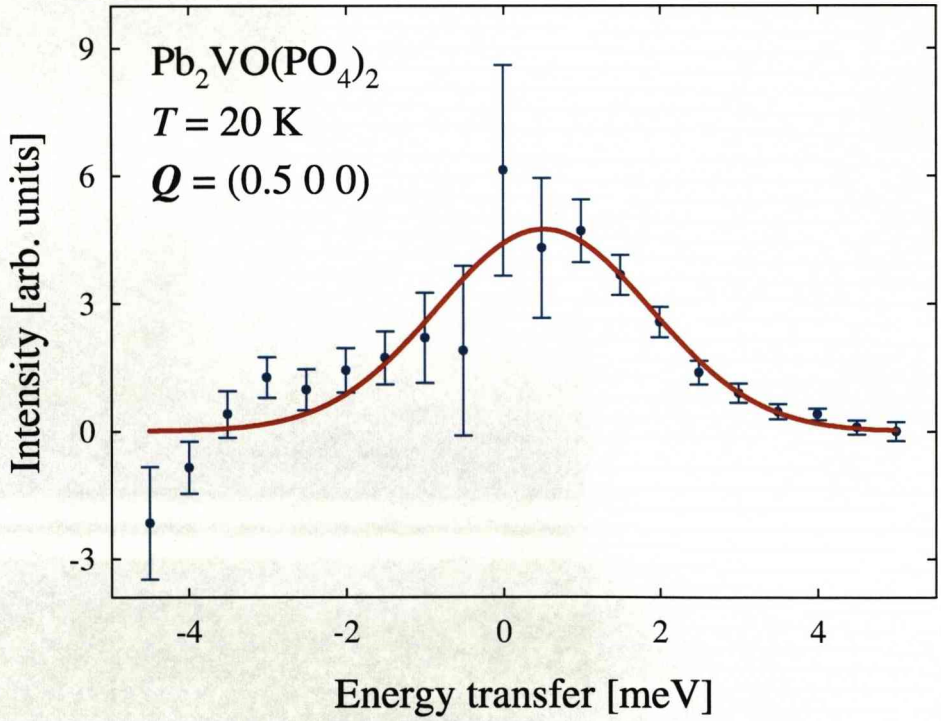

Figure 3.17: Typical energy scan showing the excitation width of powdered $Pb_2VO(PO_4)_2$ at 20 K. This particular excitation has a FWHM of $\sim \pm 3.2$ meV.

3.3.2 $SrZnVO(PO_4)_2$

Originally discovered by Meyer, Mertens and Müller-Buschbaum [88] who only reported the structural characterisation, this compound shares many characteristics with its relative 2DQHAF $Pb_2VO(PO_4)_2$. Their structural relationship is the replacement of the two Pb^{2+} cations by Sr^{2+} and Zn^{2+}. Again, it forms a two-dimensional square lattice of V^{4+} ions with competing interactions leading to frustration. The profound structural similarities with $Pb_2VO(PO_4)_2$ attracted our interest since small changes introduced by the cationic substitution can tune the magnetic exchanges J_1 and J_2 and thus the frustration ratio. The method of getting the exchange constants is in principle the same as descibed in section 3.3.1.

Structure

Strontium zinc vanadium oxide bis(phosphate) ($SrZnVO(PO_4)_2$) crystallises in the orthorhombic system with spacegroup *Pbca* and lattice parameters $a = 9.0660$ Å, $b = 9.0117$ Å and $c = 17.5130$ Å [76, 89]. Because of its low structure symmetry eight formula units are contained in one unit cell (Z=8). Note that the *c-axis* is almost doubled compared to a and b, as opposed to $Pb_2VO(PO_4)_2$. Projections of the $SrZnVO(PO_4)_2$ structure are shown in fig. 3.18, revealing the extreme similarities with that of $Pb_2VO(PO_4)_2$ (compare with fig. 3.10). The main difference between their space group arises from the way the $VOPO_4$ layers are stacked along the *c-axis* and, therefore, does not imply any significant structural change in the magnetic layers. In $SrZnVO(PO_4)_2$, the a and b structural axes are defined in the literature as rotated by 90° with respect to the $Pb_2VO(PO_4)_2$ ones. For this reason, the wave-vector of the modulation in the $VOPO_4$ corrugated layers in this compound is parallel to the *a-axis* instead of parallel to b as in $Pb_2VO(PO_4)_2$.

In $SrZnVO(PO_4)_2$ the interlayer distance is appreciably smaller compared to that of $Pb_2VO(PO_4)_2$ (8.7565 and 9.8635 Å respectively). This behaviour correlates qualitatively with the ionic radii of the involved A^{2+} cations: Pb^{2+}=1.12 Å,

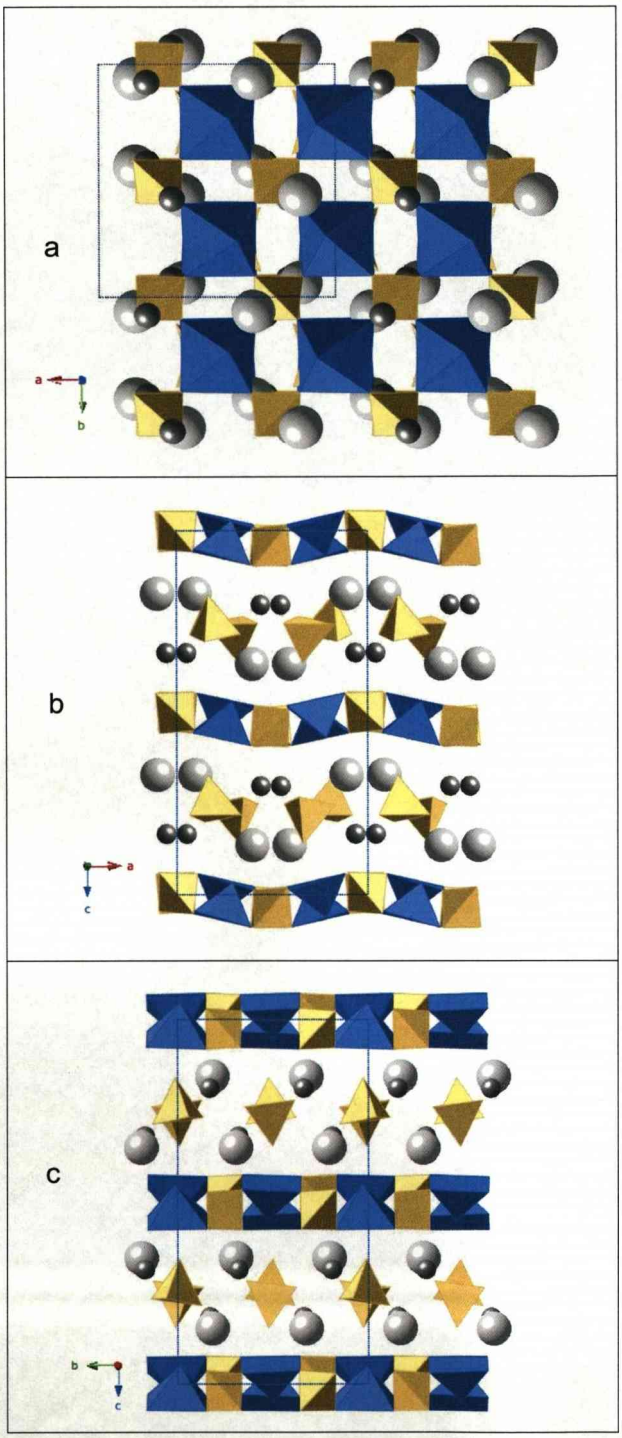

Figure 3.18: The structure of $SrZnVO(PO_4)_2$, similarly to that of $Pb_2VO(PO_4)_2$, contains corrugated layers formed by VO_5 square pyramids (blue), oriented in alternating directions. The pyramids are connected by tetrahedral PO_4 groups (yellow), while the layers are separated by Sr (light grey) and Zn (dark grey) atoms and isolated PO_4 tetrahedra. Projections shown are along the a) *ab*, b) *ac* and c) *bc* planes.

Sr^{2+}=1.18 to 1.26 Å and Zn^{2+}=0.6 to 0.73 Å. We can see that Zn^{2+} is much smaller than Pb^{2+}, which explains the smaller interlayer distance in $SrZnVO(PO_4)_2$. The characteristics of the interlayer zone are very important in these compounds, because it determines the degree of modulation of the $VOPO_4$ layers. This modulation modifies all the molecular bond angles and lengths, in contrast to the highly symmetric $Li_2VOSi(Ge)O_4$ compounds. One expects this to modify the superexchange energies and thus the magnetic properties. Between these compounds, $SrZnVO(PO_4)_2$ presents the highest degree of modulation of the $VOPO_4$ layers [76].

Magnetic susceptibility

The magnetic properties of $SrZnVO(PO_4)_2$ are, in all aspects similar to those of $Pb_2VO(PO_4)_2$ as is naturally expected from the high degree of resemblance between their structures. However, some qualitative differences are expected, since the $VOPO_4$ layers are more distorted than in $Pb_2VO(PO_4)_2$. The polycrystalline sample was measured under an applied field of 1000 Oe and in the temperature range 1.7 K<T<360 K. At high temperatures χ(T) follows closely a Curie-Weiss law down to $T \sim 50$ K. Below that, χ(T) deviates from this CW behaviour going through a broad maximum at $T_{\mathrm{Max}} \sim 6.3$ K as shown in fig. 3.19 (a). This maximum is an indication of the energy scale of this two-dimensional system, which is slightly lower than the one of $Pb_2VO(PO_4)_2$. The Néel temperature for $SrZnVO(PO_4)_2$ is $T_{\mathrm{N}} \sim 2.6$ K, as can be seen from a kink in χ(T) at this point. This magnetic ordering can be observed more clearly in the $\partial\chi/\partial T$ (T) plot of fig. 3.19 (b). For this compound, the value of T_{N} is much more clear-cut than in the case of $Pb_2VO(PO_4)_2$. This is because the SQUID magnetometer can maintain a much more stable temperature, being further away from ^{4}He's boiling point, and hence give more accurate measurements. Typical error bars, shown in this plot, confirm that. Similarly to before, the temperature of the maximum in

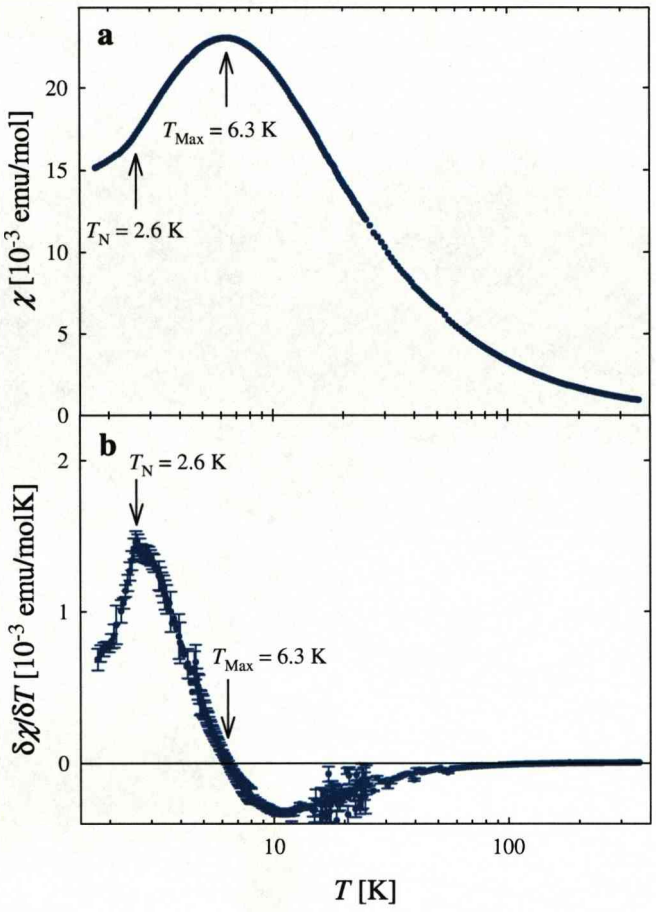

Figure 3.19: Magnetic response of polycrystalline $SrZnVO(PO_4)_2$, measured at 1000 Oe. Part (a) shows χ(T) characteristic for a low-dimensional spin system (as for $Pb_2VO(PO_4)_2$, see fig. 3.11 a) while b) is the differential $\partial\chi/\partial T$ (T). A change of slope in χ(T) indicates a magnetic phase transition at $T_N \sim 2.6$ K while T_{Max} gives the approximate energy scale for this two dimensional system.

χ(T), T_{Max}, has been taken as the temperature at which $\partial\chi/\partial T = 0$. The presence of paramagnetic foreign phases is excluded in this sample too, since there is no upturn in χ(T) below T_N.

Following the same analytical steps we performed for $Pb_2VO(PO_4)_2$, the high temperature data were fitted according to the Curie-Weiss law (eq. 3.3). Fig. 3.20 shows the inverse of the experimental susceptibility together with the CW law fit, giving $\theta_{CW} = (1.5\pm1)$ K for this compound. This extremely low value of θ_{CW},

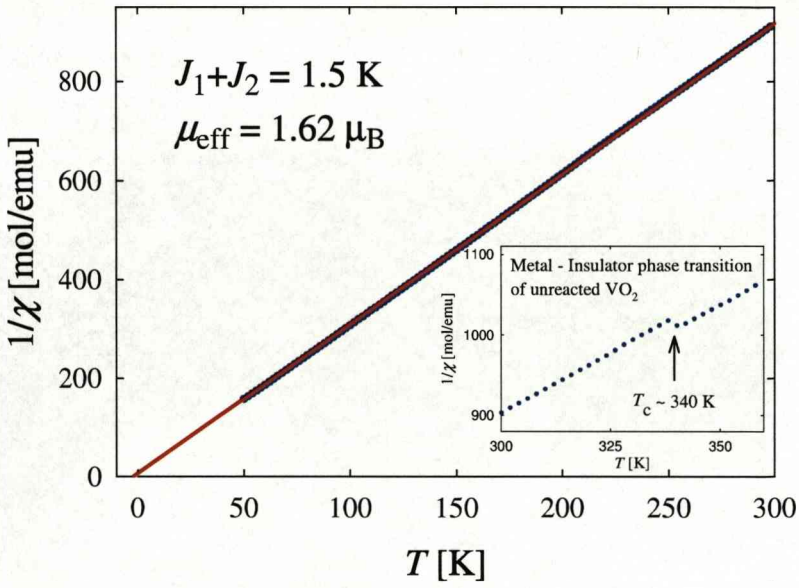

Figure 3.20: Inverse susceptibility of polycrystalline $SrZnVO(PO_4)_2$ for $T > 50$ K, together with the Curie-Weiss law fit (red line), giving $\theta_{CW} = (1.5\pm1)$ K. The inset shows a metal-insulator phase transition of unreacted VO_2 at $T_c \simeq 340$ K, observed as a step in χ^{-1}(T).

compared to $Pb_2VO(PO_4)_2$, indicates either very weak interactions - which would be in contradiction with the pronounced maximum at a relatively larger T - or a higher degree of frustration. Remembering that $\theta_{CW} = J_1 + J_2$, this low θ_{CW} value suggests that J_1 and J_2 have a similar magnitude but a different sign.

The effective moment and Landé g-value calculated from equations (3.4) and (3.5) are $\mu_{eff} = (1.62\pm0.07)$ μ_B and $g_J = 1.87\pm0.09$ for $SrZnVO(PO_4)_2$, consistent with an $S = 1/2$ system.

Similarly to $Pb_2VO(PO_4)_2$, we observe a step in the susceptibility at $T_c \simeq$ 340 K, shown in the inset of fig. 3.20, coming from a small amount of unreacted VO_2. This result agrees with the well studied metal to insulator transition of this oxide [81–85]; above 340 K it adopts the rutile structure with the V^{4+} ions forming a body-centred tetragonal lattice, while below 340 K, its symmetry distorts to a monoclinic cell.

Neutron measurements

In order to clarify the situation with $SrZnVO(PO_4)_2$, a neutron scattering experiment was performed in very much the same way as for the previously studied compound. The magnetic ground state and short-range spin correlations measured on D7 are presentented in this section.

- ***Magnetic ground state***

Below the Néel temperature of $SrZnVO(PO_4)_2$ ($T_N \sim 2.6$ K), the magnetic moments of the vanadium ions orient in a specific way giving rise to magnetic diffraction peaks, whose pattern is shown in figure 3.21. The general picture consists again of sharp magnetic peaks, coming from the ordered moment of the V^{4+} ions, superimposed on a diffuse magnetic background coming from the disordered component of the magnetic ions. By comparing it with that of $Pb_2VO(PO_4)_2$ (fig. 3.14), we observe that the patterns do not look alike. This is due to the different structures of the lattices in real space for these compounds (monoclinic space symmetries generally have more diffraction peaks than orthorhombic).

The red curve of fig. 3.21 corresponds to a CAF ground state spin structure model. Calculations of $\boldsymbol{Q} = (0, \pi)$ and $(\pi, 0)$ ordering wave vectors give the same result, due to the fact that the lattice constants a and b are closer to each other compared to its relative $Pb_2VO(PO_4)_2$. Inconsistencies at $Q > 1.5$ Å^{-1} are attributed to large nuclear scattering.

In order to get an absolute value for the effective moment, a nuclear structure factor calculation was first performed. This allows for normalising the magnetic calculation's integrated intensities with those of the experiment, as descibed in eq. (3.7) ($N \sim 800$ in this case). By using the same widths as for the structural and magnetic Li_2VOSiO_4 peaks we obtain $\mu_{\text{ord.}} = (0.42 \pm 0.04)\ \mu_B$ for $SrZnVO(PO_4)_2$. This lower ordered moment suggests that this compound has a higher degree of *frustration* compared to $Pb_2VO(PO_4)_2$, and is closer to the spin-liquid region

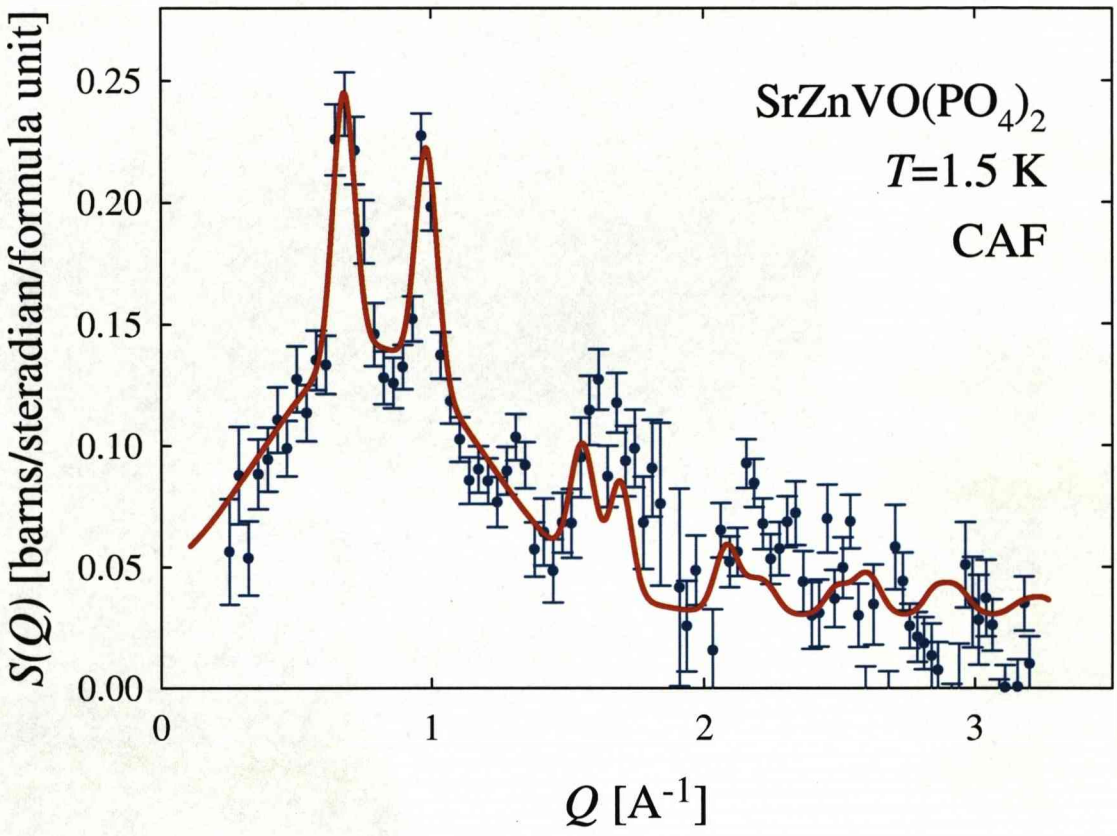

Figure 3.21: Magnetic ground state diffraction pattern of $SrZnVO(PO_4)_2$ at 1.5 K. Sharp magnetic Bragg reflections coexist with a diffuse background, as for $Pb_2VO(PO_4)_2$. However, the reduced ordered moment of $\sim$ 0.42 μ_B brings this compound even closer to the spin liquid regime. Best fit was obtained with a CAF ground state spin structure, shown as the solid line on the plot.

of the $J_1 - J_2$ phase diagram (fig. 3.8). Here, the diffuse background does not resemble that of a simple magnetic form factor and was therefore empirically fitted. This background arises from short-range spin correlations, which coexist with the long-range CAF order, and reinforces the presence of *quantum disorder*.

- ***Spin correlations***

Exchange interactions J_1 and J_2 were again determined by diffuse neutron scattering. Fig. 3.22 shows the static structure factor $S(Q)$ measurement for powdered $SrZnVO(PO_4)_2$ at $T = 35$ and 15 K, temperatures into the paramagnetic phase for this compound. These short-range spin correlations were modelled by a first-order HTSE of the dynamic susceptibility, as before. The Curie-Weiss temperature ($\theta_{CW} = 1.5$ K for this compound) was used as a constraint in extracting J_1 and J_2. The calculations, shown as the red lines in fig. 3.22, are for ferromagnetic $J_1 \sim (-4 \pm 1)$ K and antiferromagnetic $J_2 \sim (5.5 \pm 1)$ K. Combining these in eq. (3.2) we get the overall energy scale of the system $J_c \sim 6.8$ K, which agrees with the position of the broad maximum in the susceptibility data, and is similar to $Pb_2VO(PO_4)_2$. The oscillations in the 35 K data (fig. 3.22 (a)) are rather small, and within the experimental error bars not very clear to see. However, the model itself predicts small variations from the form factor for this quantum disordered system. Note that $T > 3J_c$ and hence, the first-order HTSE (eq. 3.10) is valid in this case. In order to see the short-range spin correlations clearer we went to the lower temperature of 15 K (fig. 3.22 (b)). The thermal energy term kT is smaller, thus the magnetic correlations are relatively stonger here. The oscillations are more pronounced as expected, but for these data T is smaller than $3J_c$ by a few degrees. As a result, the first-order HTSE is not a valid approximation to take and although there is good agreement, these data give only a qualitative test of the model.

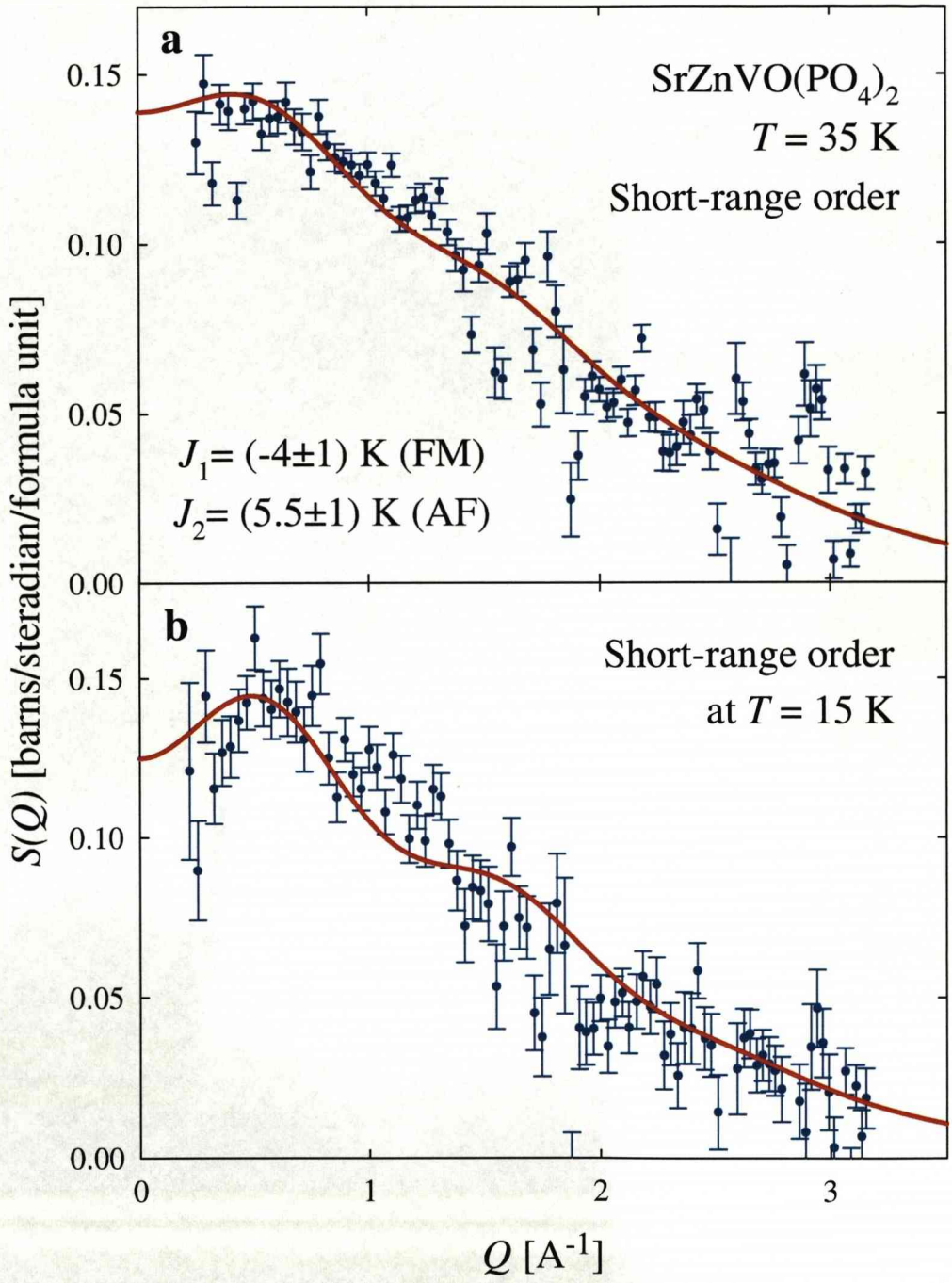

Figure 3.22: Short-range spin correlations in the paramagnetic phase of $SrZnVO(PO_4)_2$. The red curves are first-order HTSE calculations for ferromagnetic $J_1 \sim (-4 \pm 1)$ K and antiferromagnetic $J_2 \sim (5.5 \pm 1)$ K. Oscillations of this quantum system are smaller at 35 K (part a) compared to those at 15 K (part b). However, first-order HTSE is not a good approximation to make in the latter case, so the comparison in (b) is qualitative.

3.3.3 Li_2VOSiO_4

The main experimental result presented here for this prototype frustrated 2DQHAF discovered by Millet and Satto [41] is the ground-state spin structure. Due to the absorbing nature of Li ($\sigma_{abs} = 70.5$ barns), the measurement was performed in the concentric cylinder geometry, as described in section 3.2. The short-range spin correlations, being much weaker, were impossible to see.

Structure

Dilithium vanadyl silicate is isostructural to the non-magnetic Ti^{4+} ($S = 0$) titanosilicates [90, 91] of general formula $A_2^{1+}TiOSiO_4$, where A^{+1}= Li or Na. The parent compound is the mineral natisite, $Na_2TiOSiO_4$ [90]. Li_2VOSiO_4 crystallises in the tetragonal system with spacegroup $P4/nmm$ and lattice parameters $a = 6.3682(6)$ Å and $c = 4.449(1)$ Å. Two formula units are contained in one unit cell (Z=2) [41]. Projections of the Li_2VOSiO_4 structure are shown in fig. 3.23 (a) and (b). This compound has a highly symmetric tetragonal structure in which the $[VOSiO_4]$ layers are separated by only one single layer of Li atoms. The structure of the layers is the same as that described for $Pb_2VO(PO_4)_2$, with the difference that these layers are completely flat and undistorted in the absence of PO_4 tetrahedra between them. The coordination polyhedra (V^{4+} pyramids and $Si^{4+}O_4$ tetrahedra) are regular, unlike in $Pb_2VO(PO_4)_2$ and $SrZnVO(PO_4)_2$. Therefore, there are only two types of oxygen ions: the *apical* and the *equatorial* ones, shown in fig. 3.23 (c). The apical oxygen forms a stronger bond with the vanadium, being closer to it than the equatorials.

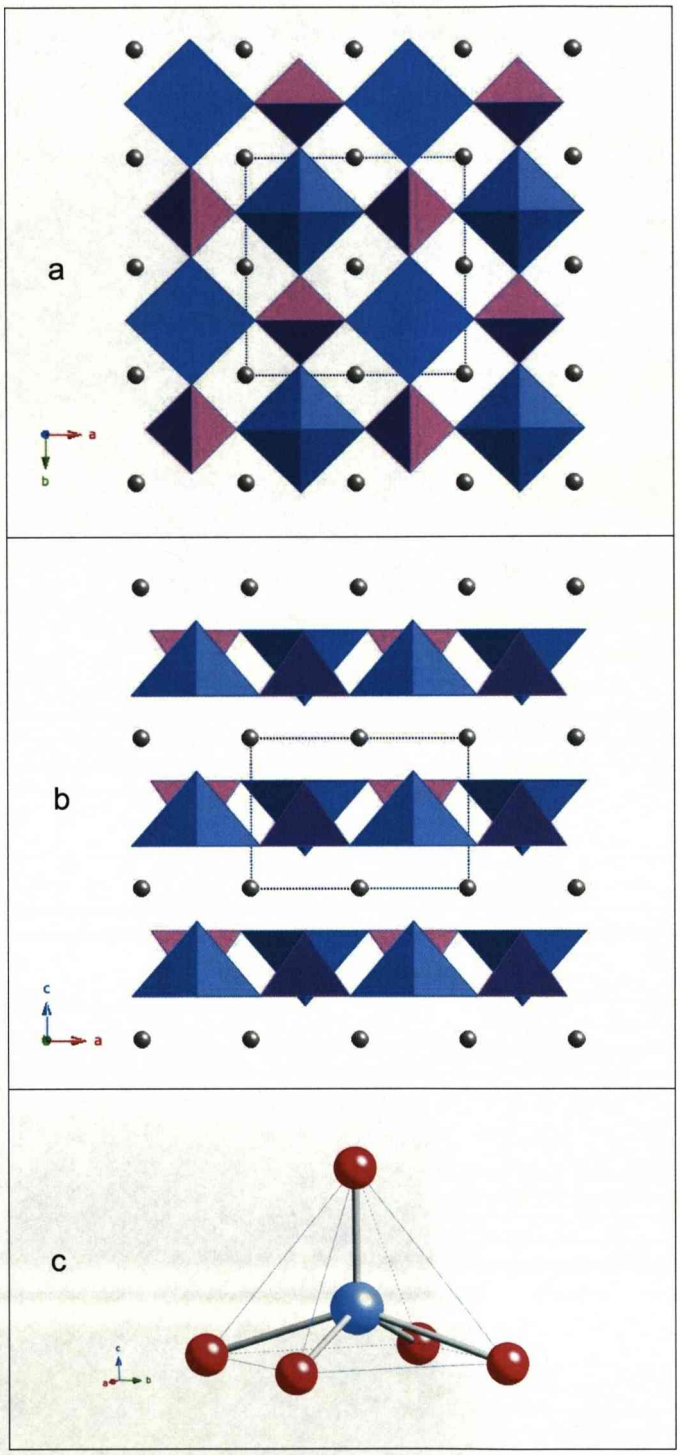

Figure 3.23: The structure of Li_2VOSiO_4 contains flat, parallel layers formed by VO_5 square pyramids (blue), oriented in alternating directions in a chessboard fashion. The pyramids are connected by tetrahedral SiO_4 groups (mauve) and the layers are separated by intercalated Li cations (grey). Projections shown are along the (a) *ab* and (b) *ac* planes. Part (c) shows a perspective view of the vanadium coordination polyhedron.

Nuclear scattering

In the case of Li_2VOSiO_4*, the structural data will be briefly discussed, since it is important to show the measurement which was used for normalising intensities and getting absolute values for the ordered moments of all three* $J_1 - J_2$ *compounds.* Interference effects from the assembly of all nuclei in the structural unit cell of Li_2VOSiO_4 give rise to the coherent scattering cross-section shown in fig. 3.24. We can already see how much smaller the error bars are in this measurement compared to any magnetic cross sections determined by the method of *xyz*-polarisation analysis. Generally speaking, structural scattering is much stronger than any magnetic scattering.

The infinitely high $\delta - functions$ which would arise from a *'mathematical'* crystal with a perfect arrangement of atoms in 3D, are broadened by the mosaic spread of the polycrystalline material as well as the instrumental resolution function of D7. Hence, a geometrical structure factor calculation convolved with a Gaussian, shown as the green line in fig. 3.24, is used to model these structural peaks. This Gaussian has a width $\sigma_{\mathrm{Li}}^{\mathrm{struct.}} = 0.0241$ Å^{-1}, and the importance of it is in getting the absolute values of the ordered moments in all of our systems, as shown in eq. (3.7). Note that in this formula, $N \sim 214$ for this case. Li_2VOSiO_4 has the highest symmetry of all three compounds (teragonal), giving only a few very well defined and not overlapping diffraction peaks. Thus, the width of the Gaussians of this simpler structural diffraction pattern was used for calculations on all compounds, in order to give higher accuracy to our results. The structural patterns of $Pb_2VO(PO_4)_2$ and $SrZnVO(PO_4)_2$ (not shown here) have indeed very good agreements with calculations using this value of σ.

For the purposes of this refinement for Li_2VOSiO_4, we only varied the lattice constants and not the fractional co-ordinates of any atoms in the unit cell. Furthermore, for this wavelength ($\lambda = 3.1$ Å), the aluminium container and cryostat give a structural peak at $Q \sim 3.11$ Å^{-1}, shown in the measurement of fig. 3.24.

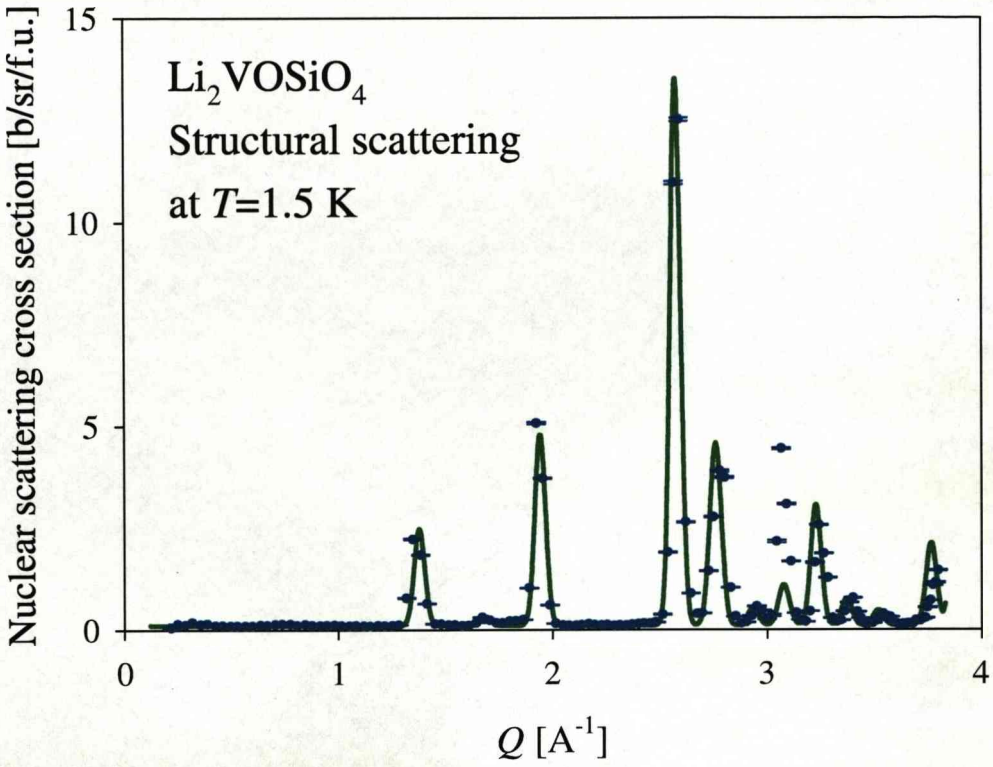

Figure 3.24: Coherent nuclear scattering cross section of Li_2VOSiO_4 at 1.5 K. The fit is a geometrical structure factor calculation convolved with a Gaussian. Best agreement with experimental data is obtained for a width $\sigma_{\mathrm{Li}}^{\mathrm{struct.}} = 0.0241$ Å^{-1}. The structural peak at ~ 3.11 Å^{-1} arises from the Al container and cryostat.

Magnetic ground state

The magnetic diffraction pattern of Li_2VOSiO_4, collected at $T = 1.5$ K, is shown in fig. 3.25. We can see that, like in the other two compounds, this ground state has ordered and disordered spin components. The ordered component of the moment gives rise to coherent scattering resulting in magnetic Bragg peaks, whilst the disordered component results in a diffuse scattering observed as the background in this measurement. The difference of this compound with respect to $Pb_2VO(PO_4)_2$ and $SrZnVO(PO_4)_2$ is that this diffuse background has a lower absolute value. From this, we infer that the disordered moment is less than in the other two compounds, which means that Li_2VOSiO_4 is not that close to the

spin liquid regime. This indeed agrees with high-temperature expansions for the uniform susceptibility and specific heat [43, 45–47], which place this compound in the *order by disorder* area of the phase diagram (fig. 3.8), whereby the frustration parameter α is greater than 1.

The diffraction pattern of the ground state of this system is best described by a CAF spin-structure model, calculated in the same way as before, using equation (3.7). This calculation is shown as the red curve on top of tha data of fig. 3.25. Since this compound is tetragonal ($a = b$), the magnetically ordered structures with wave vectors $\boldsymbol{Q} = (0, \pi)$ and $\boldsymbol{Q} = (\pi, 0)$ are equivalent.

For the same reasons as in the previously described nuclear scattering of Li_2VOSiO_4, the magnetic peaks have a finite width. In this case, the value of the width best describing the data is $\sigma_{\mathrm{Li}}^{\mathrm{magn.}} = 0.0398$ Å^{-1}. This result is used in normalising calculated intensities, with respect to experimentally measured ones, for all three compounds, according to eq. (3.7). As for the structural scattering, Li_2VOSiO_4's magnetic pattern is simpler to model, yielding more accurate results for the magnetic width.

The ordered moment of this compound comes out as $\mu_{\mathrm{ord.}} = (0.55 \pm 0.04)\ \mu_{\mathrm{B}}$, in agreement with [92]. The value of this moment is larger compared to the $Pb_2VO(PO_4)_2$ and $SrZnVO(PO_4)_2$ compounds. This result, reinforces the fact that Li_2VOSiO_4 is a less frustrated spin system than the other two, something suggested earlier in view of the lower diffuse background level.

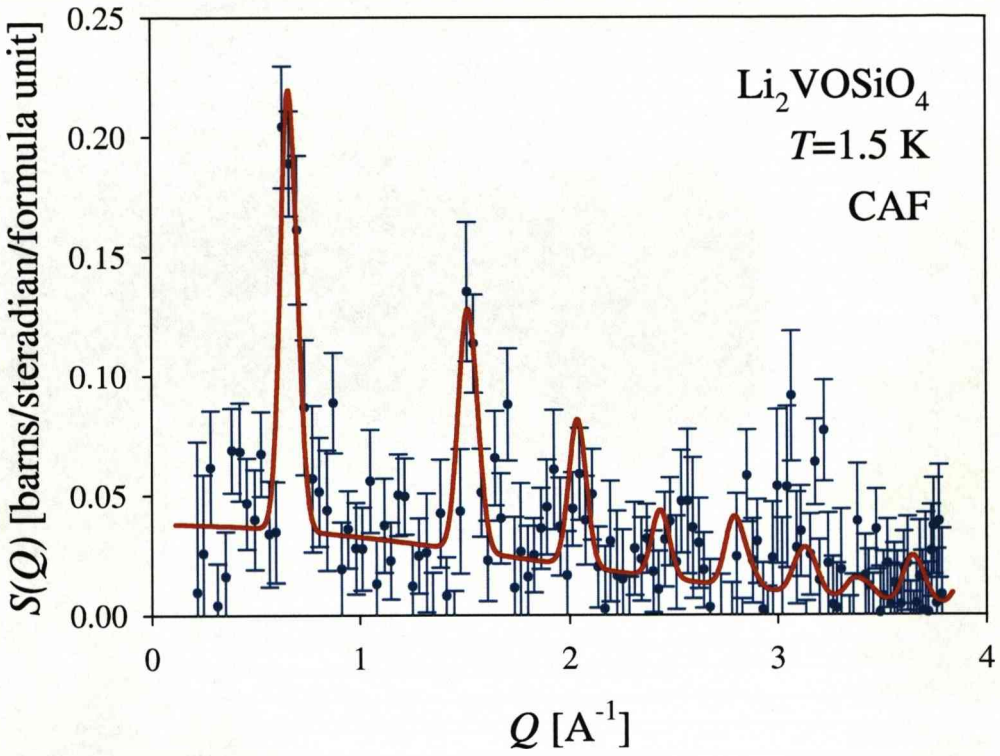

Figure 3.25: Magnetic ground state diffraction pattern of Li_2VOSiO_4 at 1.5 K. Sharp magnetic Bragg reflections coexist with a diffuse background, as for $Pb_2VO(PO_4)_2$ and $SrZnVO(PO_4)_2$. However, the latter component is smaller, suggesting that this compound has a lower degree of frustration. Best fit is obtained for a CAF ground state spin structure with an ordered moment of $\sim 0.55\ \mu_B$, shown on the plot.

3.4 Discussion

Throughout this chapter, the $J_1 - J_2$ model of magnetic interactions has been used in describing two-dimensional frustrated quantum Heisenberg antiferromagnets. Some new and interesting magnetic properties of such novel quantum magnets have been explored at a fundamental level by using neutrons. In particular, $Pb_2VO(PO_4)_2$ and $SrZnVO(PO_4)_2$ are the first experimental realisations of frustrated square-lattice ferromagnets. Here, we will attempt to show the diversity of properties that the $J_1 - J_2$ phase diagram (see fig. 3.8) can have, by using selected example materials.

3.4.1 Classical examples: Mn,MgO and Mn,ZnF_2

By mixing a magnetic crystal with an isomorphous diamagnetic one, an artificial situation can be created so that in the random distribution of magnetic ions there occur isolated groups of two, three or more close neighbours. This technique is particularly useful for studying the exchange in strongly coupled systems where there are magnetic transitions. In order to determine the exchange interactions for these systems, paramagnetic resonance experiments were performed, being the most direct method available in the early 60's for investigating such interactions [93, 94].

In the first salt, neighbouring Mn^{2+} ions are present as substitutional impurities in MgO, with Mn:Mg $\sim$ 1:100. The exchange interactions between Mn^{2+} ions in this fcc structure are expected to be similar to those in the antiferromagnetic MnO. The analysis of the spectra gave antiferromagnetic interactions $J_1 \sim J_2 \sim 28$ K [95]. The other studied material is similar to the first one, but with a ratio of Mn:Zn $\sim$ 1:50 and a body-centred tetragonal unit cell. The principle followed was the same but the results differed qualitatively in that the NN interaction was found to be ferromagnetic with a strength of $J_1 \sim -0.4$ K. The NNN interaction is antiferromagnetic with $J_2 \sim 4$ K [96].

These dilute magnetic systems do not form a regular square lattice, although one can define and measure NN and NNN interactions. The fundamental difference with the compounds discussed so far is that they cannot be treated as quantum systems since their spin value of $S = 5/2$ is high for quantum fluctuations to occur. Nevertheless, it is interesting to see that people were interested and had devised materials and techniques for measuring them half a century ago. Further to that, Mn,ZnF_2 is a salt where mixed ferro- and antiferromagnetic interactions were observed, a very puzzling result for the authors of ref. [96].

3.4.2 Néel order: $VOMoO_4$

This compound, nearly isostructural to Li_2VOSiO_4, is formed by $MoVO_5$ layers containing VO_5 pyramids separated by MoO_4 tetrahedra. The only difference is that in Li_2VOSiO_4 a plane of Li^+ ions is present between the $SiVO_5$ layers [97].

Initially, it was thought to be a prototype of a weak one-dimensional antiferromagnet [98, 99], although more recent works have established it as being a 2DQHAF described by the $J_1 - J_2$ model [97, 100].

An interesting property of this compound is that even though its structure is similar to Li_2VOSiO_4's, the exchange couplings are more than an order of magnitude larger. From susceptibility measurements, Carretta *et al.* [97] found $T_N \sim 42$ K, and estimated $J_1 + J_2 \sim 155$ K.

Neutron powder-diffraction measurements performed on $VOMoO_4$ show a simple AF Néel state below ~ 40 K, with spins pointing either along the c axis or in the ab plane [100]. This magnetic order gives a dominant role to the NN interaction ($J_1 \gg J_2$), placing this system in the unfrustrated Néel region of the $J_1 - J_2$ phase diagram. The saturated magnetic moment of this system ($\mu_{ord.} \sim 0.41\ \mu_B$ at 2K) strongly indicates a two-dimensional character and enhanced quantum fluctuations. Furthermore, the value of the magnetic moment is claimed to be consistent with $J_2 \sim 0.2 J_1$ [100].

However, the individual values of J_1 and J_2 for this square lattice still await to be determined directly by appropriate experiments. Such results would be of particular interest to theorists and would help to parametrise better this area of the phase diagram.

3.4.3 Order by disorder: Li_2VOSiO_4

The peculiarity of that system with respect to other realisations of the $S = 1/2$ Heisenberg model on the square lattice comes from the arrangement of the VO_5 pyramids. They point upwards on one sublattice and downwards on the other. As a consequence, nearest neighbours are not in the same horizontal plane while next-nearest neighbours are, and the coupling J_1 between nearest neighbours does not necessarily need to be larger than the coupling J_2 between next-nearest neighbours [101]. Furthermore, the superexchange path of NN differs from that of NNN. The nearest neighbour exchange follows a 90° path through a tetrahedral SiO_4 group, while the next-nearest neighbour exchange pathway is in a straight line with the intermediate SiO_4 group. Since the $J_1 - J_2$ model predicts a degenerate groundstate if $J_2 > J_1/2$, this compound is *a priori* a good candidate to study the physics in that regime.

Indeed, various techniques have determined that Li_2VOSiO_4 develops such a long-range order with a value for the frustration parameter $\alpha > 0.5$ [42, 43, 45–47, 92], driven by the *order from disorder* mechanism. The precise nature of this transition is not fully understood though. A residual coupling between the layers, as well as thermal fluctuations can play a role in selecting magnetic configurations. Furthermore, quantum fluctuations have not fully lifted the classical degeneracy - the quantum state is twofold degenerate with $\boldsymbol{Q} = (0, \pi)$ or $(\pi, 0)$ magnetic ordering wave vectors. F. Mila suggested studying phonons as a way of exploring this [101]. If the system is coupled to phonons, one can expect that the breaking of the rotational symmetry of the spin fluctuations will induce a lattice distortion.

Finally, the precise value of the ratio J_2/J_1 is not yet known for Li_2VOSiO_4, with values in the literature ranging from 1.1 [43] to 4.8 [45] up to 11.7 [46, 47]. A diffuse neutron scattering experiment using xyz-polarisation analysis would clarify the situation, although a sample with the non-absorbing isotope of Li is required for the data collection.

3.4.4 Frustrated ferromagnets: $Pb_2VO(PO_4)_2$, $SrZnVO(PO_4)_2$ and related compounds

The distinctive characteristic of these phosphates is the commensurate modulation of the $[VOPO_4]$ layers which is a consequence of the complicated structure of the $[A_2^{2+}PO_4]$ region. The magnitude of this modulation is determined by the actual composition of the interlayer $[A_2^{2+}PO_4]$ zone [76].

For the two studied compounds $Pb_2VO(PO_4)_2$ and $SrZnVO(PO_4)_2$, the substitution of Pb^{2+} cations for Sr and Zn keeps the general layout of the structure unchanged. However, it introduces distortions in the whole lattice which affect the exchange constants. For $Pb_2VO(PO_4)_2$ we get a frustration ratio $\alpha \sim -3.25$ and a frustration angle $\phi \sim 107°$. In the case of $SrZnVO(PO_4)_2$ - where the $VOPO_4$ layers are more distorted - our analysis gives $\alpha \sim -1.38$ and $\phi \sim 126°$. This is much closer to the phase boundary between the *spin-liquid* and CAF regions, believed to be at $\phi \sim 145°$ for frustrated ferromagnets [74]. The reduced moments and diffuse background of these CAF systems measured at the base temperature of 1.5 K, also suggest that there are enhanced quantum fluctuations. In particular, $SrZnVO(PO_4)_2$ has a lower ordered moment per V^{4+} site ($\mu_{\text{ord.}} \sim 0.42\ \mu_B$ compared to $\sim 0.5\ \mu_B$ for $Pb_2VO(PO_4)_2$), reinforcing the fact that it is closer to the so-called *spin-liquid* regime. These results show that this family of compounds has a high flexibility for tuning the magnetic exchange interactions by chemically substituting the cations in the interlayer zone. Other combinations of A^{2+} cations may be used to shift the system closer towards the critical region, thus providing crucial tests for the theories and models. Such possibilities include $BaZnVO(PO_4)_2$ and $BaCdVO(PO_4)_2$ [88, 102].

Chapter 4

Orbital ordering in $GdVO_3$

An electron in a solid - being bound to or nearly localised on a specific atomic site - has three attributes: charge, spin and orbital. The orbital represents the shape of the electron cloud in the solid. In transition-metal oxides (TMO) with anisotropic-shaped d-orbital electrons, the Coulomb interaction between the electrons (strong electron correlation effect) is of importance for understanding their metal-insulator transitions and properties such as high-temperature superconductivity and colossal magnetoresistance. The orbital degree of freedom can play an important role in these phenomena. Its correlation and order-disorder transition causes a variety of effects through strong coupling with charge, spin and lattice dynamics [103]. An overview is given here on this *"orbital physics"*, starting from general concepts applied to TMO and then more specifically to the RVO_3 compounds, where R is Y or a rare earth element.

4.1 Orbital physics in transition metal oxides

The wave function of an electron can take various shapes when bound to an atomic nucleus by the Coulomb force. These shapes are termed as orbitals. Only s orbitals are spherically symmetric; the others have a pronounced angular de-

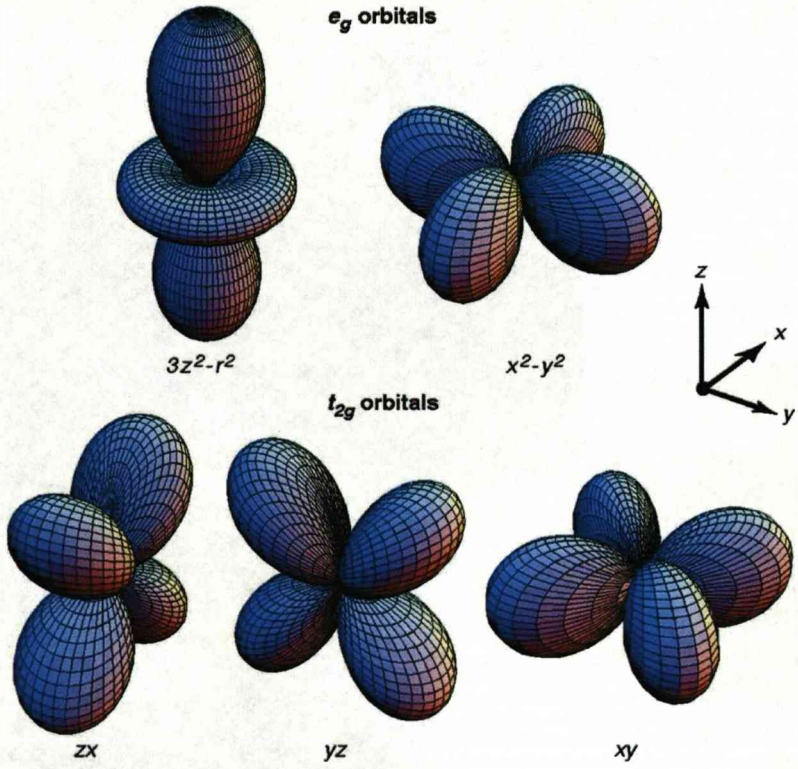

Figure 4.1: The angular distribution of d orbitals, after Y. Tokura *et al.* [103]. The $d_{3z^2-r^2}$ and $d_{x^2-y^2}$ levels are grouped together and called the e_g levels. Similarly for d_{xy}, d_{xz} and d_{yz}, called the t_{2g} levels. The $d_{3z^2-r^2}$ orbital is also referred as d_{z^2}. In a spherical symmetry they all lie on the same energy level, however this degeneracy is lifted in a cubic environment.

pendence. This means that, since local environments in crystals are often not spherically symmetric, different orbitals will behave in different ways. Therefore, local environment in a crystal plays a crucial role on the energy levels of an atom.

For TMO, the relevant electrons for the superexchange interaction are the outermost d electrons. The d orbitals fall into two classes, the e_g orbitals which point *along* the x, y and z axes (the $d_{3z^2-r^2}$ orbital, which has lobes pointing along the z axis and the $d_{x^2-y^2}$ orbital, which has lobes pointing along both the x- and y-axes) and the t_{2g} orbitals which point *between* these axes (these are the d_{xy}, d_{xz} and d_{yz} orbitals). Fig. 4.1 shows schematic representations of these orbitals [72, 103].

Cubic environment in octahedra

A common case of a local environment to consider is the octahedral one, adopted by many TM compounds. The TM ion sits at the centre of an octahedron surrounded by six ions such as oxygens situated on each corner. The crystal field in this case arises mainly from electrostatic repulsion from the negatively charged electrons in the oxygen p orbitals. Now, let us consider the four oxygen ions located at the x-y plane of the octahedron, and assume by convention that they congregate *along* these x and y axes. The three t_{2g} orbitals which point between the x, y and z axes have a lower overlap with the neighbouring oxygen p orbitals than the e_g orbitals and hence will have a lower electrostatic energy. The five levels (which would be degenerate in a spherically symmetric charge distribution) split therefore, with the threefold t_{2g} levels lowered in energy and the twofold e_g levels raised in energy [72, 104, 105].

Mott insulators - Hubbard model

So far we have considered only one TM ion. However, in solids - with a periodic array of atoms - there are two important features added on. One is the magnetic interactions manifesting as exchange couplings between spins and the other is the possible band formation and metallic conduction of the electrons. The most widely accepted theory for TMO and in particular *vanadates and titanates* - commonly referred to as *Mott insulators* - is given by the *Hubbard model.* Normally, metallic behaviour occurs because electrons save kinetic energy by being delocalised over the whole of the crystal. However, in TMO the onsite Coulomb energy (energetic cost of putting extra electrons on a lattice site) is so strong to overcome that electrons cannot move freely through the crystal but have to avoid each other. As a result, metallic behaviour breaks down and electrons can no longer be treated as free particles; electron correlations are important. Therefore, the system is insulating, even though electronic bands are not fully occupied or

empty, contrary to standard band theory predictions. The competition between metallic behaviour (which gives kinetic energy gain and is parametrised by the energy width of the conduction band W) and the Coulomb repulsion energy U is expressed by the *Hubbard model*. If U is not infinite, it is possible for an electron to visit its neighbour's site providing their spins are antiparallel, a requirement coming from Pauli's exclusion principle. This is energetically favourable, so that electrons on neighbouring sites are antiparallel, forming an AF structure. Such an antiferromagnetic insulator is known as a *Mott insulator*. The most important difference from the usual band insulator is that the internal degrees of freedom, spin and orbital, still survive in the Mott insulator. In these systems, metallic behaviour can be realised when U is smaller than the electronic bandwidth W, while at the crossover $U \sim W$ there is a metal-insulator transition [72, 103].

Distorted perovskite structure

Let us now consider the Mott insulators with composition ABO_3, where A and B sites accommodate the rare-earth and TM ions, respectively. They crystallise in a structure based on the ideal cubic mineral perovskite, $CaTiO_3$. This consists of shared TiO_6 octahedra situated at the corners of the cube, with the larger Ca ion in the body centre of the unit cell, as shown in fig. 1.1(a). ABO_3 compounds are distorted versions of this structure, with the TM coordination polyhedra slightly tilted, in order to adapt to various mismatches between equilibrium $(A - O)$ and $(B - O)$ bond lengths [104, 106]. This type of distorted perovskite cell was originally observed in *gadolinium ferrite*, hence the terminology "$GdFeO_3$-type distortions" is now commonly used in describing these systems. These distortions play an important role in orbital physics. Despite the very simple, nearly cubic lattice formed by magnetic ions, a variety of spin structures have been observed in these compounds, with the basic ones shown in fig. 4.2 [107]. Example materials include $YTiO_3$ and $LaTiO_3$ exhibiting isotropic ferromagnetism and G-type anti-

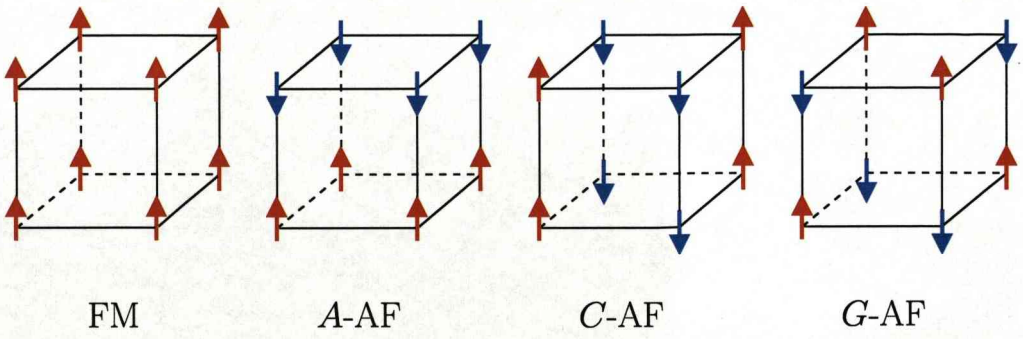

Figure 4.2: Perovskites can order ferromagnetically, in an A-type (C-type) AF structure consisting of ferromagnetic planes (chains) with AF order between them or with spins staggered in all three directions (G-type AF structure).

ferromagnetism respectively. Furthermore, anisotropic magnetic states of the C- and A-type are observed in $LaVO_3$ and $LaMnO_3$ respectively. The richness of the spin-orbital states realised in these compounds with a similar lattice structure indicates that different mechanisms lifting the orbital degeneracy might be at work, depending on the type of orbitals, the spin value and the relative magnitudes of U and W (closeness to the Mott transition) [108].

Jahn-Teller effect

Before proceeding in a more detailed description of these mechanisms, let us introduce the "Jahn-Teller effect" (JT), a key concept for most orbitally ordered TM systems. The Jahn-Teller effect is a name applied to several phenomena which occur in systems having a degenerate electronic state (orbital degeneracy). In the original papers [109, 110], a theorem is proved according to which any configuration of atoms or ions (except a linear chain) with a degenerate electron ground state is unstable with respect to deformations which lower the symmetry of the configuration (the degeneracy here is understood to be other than the Kramers spin degeneracy). Hence, this degeneracy of highly symmetric configurations is lifted, giving rise to a specific and strong electron-vibrational interaction termed

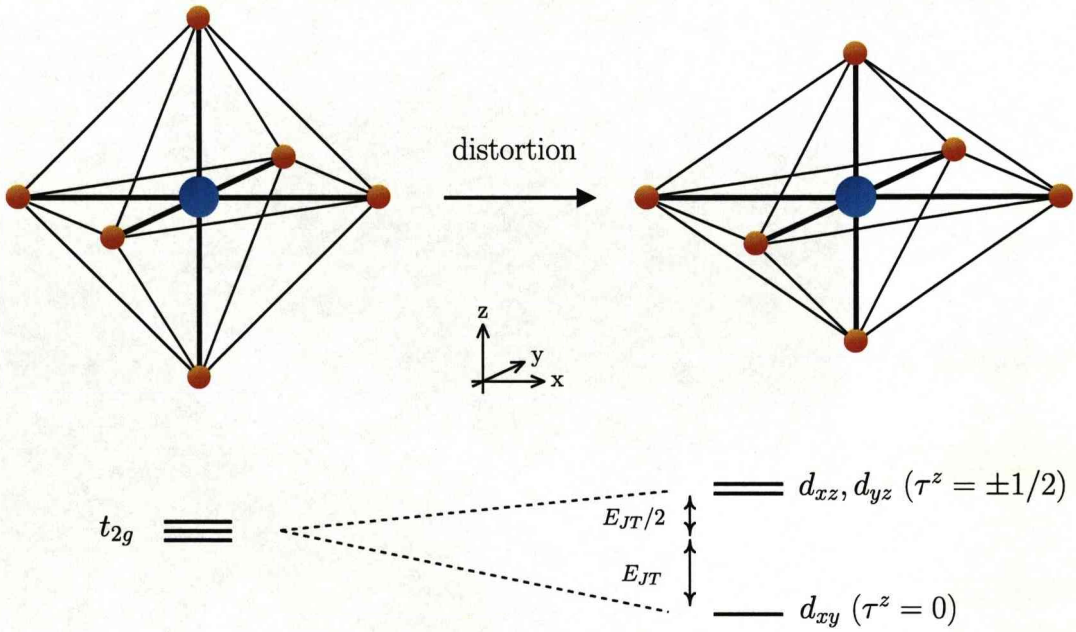

Figure 4.3: The Jahn-Teller effect for a t_{2g} system. An octahedral complex can distort and lift the cubic-symmetry degeneracy of orbital energy levels by splitting them. If the orbitals are not completely filled, the distortion lowers the total energy of the ion at the expense of the crystal elastic energy.

as 'vibron', essentially coming from the orbital-lattice coupling [105, 108]. This interaction can be thought of as existing between the electrons of the degenerate level and (a) the deformation of the surroundings or equivalently, (b) the vibrations of the ligands surrounding the given ion. In several cases it causes structural phase transitions which lower the symmetry of the crystal as a whole [111]. This is generally driven by energy minimisation; it sometimes is energetically favourable for octahedra to spontaneously distort as shown in fig. 4.3, altering the orbital energy levels. There is an elastic energy cost for that, but it is compensated by the resultant electronic energy saving due to the distortion. Fig. 4.3 is a schematic diagram of this effect for the case of t_{2g} electronic systems, showing the resulting structure and orbital energy levels. Assume that only one orbital is occupied by an electron (t_{2g}^1 electronic configuration), and the symmetry of the crystal field

experienced by this d-electron is high, leading to the orbital degeneracy problem. Now, if the octahedron distorts, with the apical oxygens shifting closer to the magnetic ion and the in-plane ones moving away, as shown in fig. 4.3, then the d_{xy} orbital ($|l^z = 0\rangle$) will be stabilised since it has a lower overlap (or Coulomb repulsion) with the wavefunctions of the apical oxygens. Hence, it is energetically favourable for the electron to occupy this level. The reverse way of looking at it is that in order for the system to minimise its energy, a nondegenerate level with the d_{xy} wavefunction moves downward by an energy E_{JT} (and is occupied by the single electron), while two other levels, with d_{yz} and d_{xz} wavefunctions (or $|l^z = \pm 1\rangle$) remain degenerate and move upwards by an energy $\Delta E = E_{\mathrm{JT}}/2$. This is naturally accompanied by a distortion of the octahedron around the magnetically active transition element. Note that systems with partially filled t_{2g} levels can be mathematically described either by an effective moment $l_{eff} = 1$ (giving $|l^z = 0, \pm 1\rangle$ as descibed above), or alterantively by an orbital spin operator τ called *pseudospin* [111], with properties that are exactly analogous to those of the usual spin operator. This fictitious spin enables one to write the Hamiltonan of the interaction of the electrons with the vibrations, and in this case it takes the value of $\tau = 1/2$, with individual τ^z's shown in the orbital energy levels of fig. 4.3 [105].

We saw before how degeneracy of orbitals can occur in a high-symmetry octahedral environment, resulting in twofold t_{2g} and threefold e_g levels of magnetoactive d-electrons. Various different mechanisms have been proposed, or actually measured in some cases, that can further remove these degeneracies. The previously described "Jahn-Teller effect" is currently at the centre of attention and believed to play a very essential role in this for the case of TMO.

The role of lattice distortions

Let us now discuss the role of general lattice distortions in lifting these degeneracies. In perovskites, there are two different origins of lattice distortions that should be distinguished. The first one is due to ionic-size mismatch effects, that generate cooperative rotations and also some distortions of octahedra in order to fulfill the close-packing conditions within a perovskite structure [104]. These are the 'extrinsic' deviations from cubic symmetry, in the sense that they are not triggered by orbitals themselves and are present even in perovskites having no orbital degeneracy at all, e.g. in $LaAlO_3$ or $LaFeO_3$. The orbitals may split and polarise under the extrinsic deformations, but they play essentially the role of spectators. In such a case it is misleading to speak of "orbital ordering" in a sense of a cooperative phenomenon, such as "spin ordering" [108]. The other type of lattice distortions comes from a *cooperative* Jahn-Teller effect [105, 112]. In materials with a high concentration of Jahn-Teller ions, the distortions and the corresponding filling of the orbitals of different centres are not independent: an interaction between them arises and makes these distortions cooperative, leading to phase transitions. The cooperative JT effect can be characterised from several points of view. First, there is a lowering of the symmetry and a distortion of the lattice, accompanied by a simultaneous ordering of orbitals. Furthermore, the JT effect and the filling of one of the orbitals are accompanied by a change in the space-charge distribution - more precisely, by the appearence of a quadrupole moment at the centre. Finally, it may be said that in a crystal the vibrations which are important for the JT effect transform from local vibrations into phonons, which propagate throughout the crystal and carry the interaction between Jahn-Teller ions. These cooperative JT-distortions - generated by the orbital-lattice coupling itself - occur at the *orbital ordering temperature*. This temperature, where the orbitals order in periodic structures similar to the (magnetic) ones shown in figure 4.2, can be experimentally seen as a structural transition. For this reason people refer to it

as $T_{\rm str}$ or $T_{\rm OO}$ [108].

Usually, these two contributions (ionic-size mismatch and cooperative JT effect) are superimposed on each other, making it difficult to identify which one is dominant. Whatever the origin though, the lattice distortions generate low (non cubic) symmetry components in the crystal field potential, which split the initially degenerate orbital levels.

Direct quadrupole interactions

Another type of interaction between Jahn-Teller ions (apart from the 'electronic-vibrational') which can also lead to an orbital ordering is the direct quadrupole-quadrupole interaction. We have already mentioned that the JT effect is accompanied by the appearance of a quadrupole moment, because of the symmetry of d electrons. In the case of e_g orbitals, it turns out that the quadrupole moment can be expressed in terms of the same pseudospins τ as for t_{2g} systems, associated with the two wavefunctions d_{z^2} and $d_{x^2-y^2}$, in such a way that d_{z^2} corresponds to the value $\tau^z = 1/2$, while $d_{x^2-y^2}$ corresponds to $\tau^z = -1/2$. For t_{2g} orbitals, the situation can be alternatively described by an effective orbital angular momentum $l_{eff} = 1$. This quadrupole-quadrupole interaction between orbitals is highly anisotropic to the extent that its form depends on the radius vector connecting the given pair [105].

Superexchange interactions between orbitals

Up to this point we have discussed two types of interactions which are of essentially the same nature and are caused by a direct Coulomb interaction (either by a direct quadrupole interaction or through anions). In Jahn-Teller systems, however, there is also an exchange interaction, which also leads to an ordering of orbitals. Furthermore, this interaction may make the governing contribution to the ordering energy. In contrast with the direct interactions, which do not depend on the spin

and which are exclusively expressed in terms of pseudospins (the spins can come into play only as a result of spin-orbit coupling), the exchange interaction also depends on the spins. This leads simultaneously to an orbital degeneracy *and* to a spin degeneracy [105, 113–116].

The primary mechanism for the exchange interaction in TM compounds, where the direct overlap of d orbitals of adjacent ions is slight, is the indirect superexchange. The overlap is essentially not between the atomic d wavefunctions but of their superposition with the s and p wavefunctions of the ligands (oxygen ions). This mechanism for lifting the orbital degeneracy is based on a natural generalisation of ordinary superexchange, which is responsible for the magnetic properties of Mott insulators. In the usual description of superexchange, the exchange interaction between neighbouring ions originates from the energy gain due to virtual hoppings of an electron to the neighbouring lattice site and back. This is determined by the effective transition integral or hopping integral t which is related to the energy bandwidth W according to:

$$W = 2zt \tag{4.1}$$

where z is the number of nearest neighbours of a given lattice site. The other very important factor is the Coulomb repulsion of electrons at a common lattice site, U. The relationship between these parameters for Mott insulators is $t \ll U$. In this limit, superexchange is completely described by the Hubbard model. Parts (a) and (b) of figure 4.4 illustrate these essential features for the case of a pair of ions with single electrons in nondegenerate levels. In part (a), hops of electrons are forbidden by the Pauli principle, while in (b) virtual transitions of the electron to the neighbouring site are allowed with an energy gain of $2t^2/U$ for the system. This corresponds to a preferred antiferromagnetic spin state. The situation changes significantly when we consider an orbital degeneracy: intra-atomic exchange J_{H} needs to be taken into account [114, 116, 117]. According to Hund's rule, the

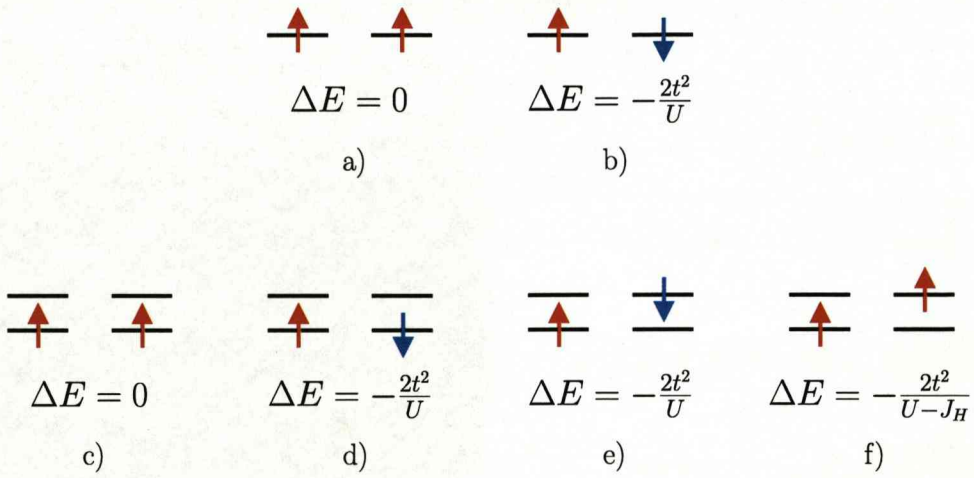

Figure 4.4: Superexchange in the case of (a-b) nondegenerate levels and (c-f) twofold-degenerate orbitals. The energy gain due to virtual hoppings of electrons between orbitals is shown for various possible configurations of an ion pair. This superexchange mechanism leads not only to spin but also to orbital ordering due to Hund's rule intra-atomic exchange coupling J_{H} (part f).

atomic configuration with the lowest energy corresponds to the maximum value of the total spin. In a degenerate level, we can have two electrons either at the same orbital (they will then have opposite spins according to the Pauli principle) or at different orbitals (but with their spins parallel). This later configuration has a lower energy, with an energy gain of J_{H} with respect to the former one. A schematic for such a system is shown in parts (c-f) of fig. 4.4. For one electron (or hole) per lattice site at a doubly degenerate level, it is favourable for it to hop to the neighbouring site in such a way that in the intermediate state, the two electrons will have parallel spins and located at different orbitals. Such an intermediate state is shown in fig. 4.4 (f) and its energy is lower than configurations (d) and (e). This way virtual hoppings are allowed too, in accordance with the Hubbard model, and the order is ferromagnetic in terms of the spin but antiferro-orbital in terms of the filling of orbitals (i.e. an alternation of orbital states). Note that in magnetic dielectrics, the relation between the three parameters discussed is

usually $t \ll J_{\mathrm{H}} < U$. It is worth mentioning here that the Hubbard model is used to describe the behaviour of materials having narrow band gaps and is based on the existence of a strong intra-atomic interaction of electrons. For reference, $U \approx 5 - 10$ eV, $J_{\mathrm{H}} \approx 1$ eV and $t \approx 0.1 - 0.3$ eV [113, 118].

Pioneers of this field Kugel' and Khomskiĭ investigated the thermodynamic properties theoretically and found that when the temperature is increased, the spin ordering vanishes first (as $T_{SO} \sim t^2 J_{\mathrm{H}}/U^2$), and then the orbital ordering, at $T_{OO} \sim t^2/U$ [113]. This result from the 70's agrees impressively well with recent measurements of $R\mathrm{VO}_3$ compounds (see for example ref. [119]).

For e_g orbitals, the superexchange mechanism for the ordering makes an appreciable contribution to the cooperative ordering and hence it acts along with the direct mechanisms (Jahn-Teller and quadrupole mechanisms). In the exchange model, the change in the lattice structure (the structural transition) is a secondary effect; here we may speak in terms of a "JT ordering without a JT interaction". Actually all three mechanisms act jointly, and it is quite difficult to determine which will be predominant in each specific case [105]. The behaviour is remarkably different for some t_{2g} compounds, where lattice effects and superexchange compete, giving rise to *orbital disorder* instead [108, 120] as we shall see in the next chapter.

We will point out again that the exchange interaction occuring in Jahn-Teller magnetic materials incorporates spin and orbital variables simultaneously. In other words, superexchange leads - in addition to spin ordering - also to orbital ordering. As a result, there is an unusual interaction between these two subsystems, and there is also the possibility that, say, the magnetic field will affect the orbital structure and so on.

Relativistic spin-orbit interaction

As mentioned before, t_{2g} states may be characterised by an effective angular momentum $l = 1$. For them, the conventional relativistic spin-orbit interaction $\lambda(\boldsymbol{S} \cdot \boldsymbol{l})$ is important, as it may sometimes play a crucial role in lifting the orbital degeneracy. The degeneracy can be also lifted by a Jahn-Teller mechanism as described before, with the two mechanisms being mutually exclusive. In order to see that, let us take the case of a single electron in a t_{2g} level; the description for a single hole (t_{2g}^2) is analogous. From the JT point of view, an octahedron is compressed along the z-axis ($c_s/a_s < 1$), as shown in fig. 4.3, giving a d_{xy} orbital (corresponding to $|l^z = 0\rangle$) at a lower energy from the degenerate d_{xz} and d_{yz} ones (with $|l^z = \pm 1\rangle$), drawn in fig. 4.5 (a). Such a deformation - favourable from the JT standpoint - has a ground state without an angular momentum ($l^z = 0$), and the spin-orbit interaction is correspondingly ineffective. Assume now a tetragonal deformation of the other sign, i.e. an elongation along the z-axis ($c_s/a_s > 1$). The lowest energy term would be the doublet $|l^z = \pm 1\rangle$. This energy decrease comes again from the JT effect but it is not as favourable since it is only half the amount of the one for compressed octahedra (with $c_s/a_s < 1$). In return, the ground state has now a non-zero orbital angular momentum which splits the doublet further by the spin-orbit interaction. The mechanism is shown in fig. 4.5 (b). The additional energy gain is λS and a spin anisotropy arises since the spin becomes oriented along the deformation axis z [105, 106].

Hence, in the ordered phase, the Jahn-Teller and spin-orbit interaction mechanisms stabilise deformations of opposite types, with a result depending on the relationship between E_{JT} and $\lambda(\boldsymbol{S} \cdot \boldsymbol{l})$. Generally speaking, these energies are comparable in magnitude in crystals of $3d$ elements, and transitions are observed by both of these mechanisms. A JT transition (if this is the dominant interaction) is a purely structural transition and the magnetic ordering occurs at some other (lower) temperature. On the other hand, the transitions determined by

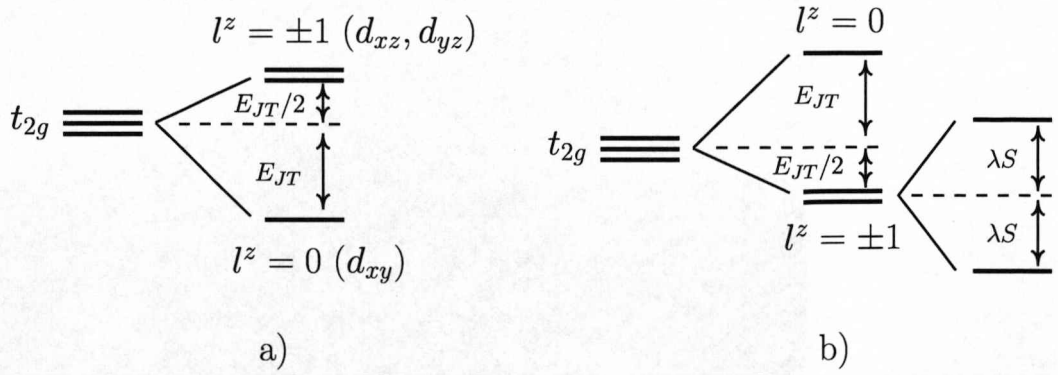

Figure 4.5: Two types of splitting of the t_{2g} one-electron level. a) 'Jahn-Teller' lifting of the degeneracy ($c_s/a_s < 1$), where the d_{xy} orbital is stabilised. b) Lifting of degeneracy due to the spin-orbit interaction ($c_s/a_s > 1$), with the deformation stabilising the twofold-degenerate state d_{xz}/d_{yz}. This state is then split by the spin-orbit interaction. Note that a_s and c_s are not lattice constants but interatomic distances between the central ion's site and surrounding anions in the octahedron.

the spin-orbit interaction occur simultaneously with the magnetic ordering. If the spins become ordered on the z-axis, then the l_s interaction will automatically stabilise the orbitals $|l^z = \pm 1\rangle$, and the corresponding lattice deformation will occur (and vice versa, if the corresponding ordering of orbitals occurs, there will be a simultaneous spin ordering). In this case, therefore, the lattice deformation occurs at the Néel temperature and has the external manifestations of simply a magnetostrictive effect [105, 108].

The above described mechanisms of lattice distortions, superexchange and relativistic spin-orbit interactions are the main ones lifting the orbital degeneracy, and hence leading to orbital ordering in TMO. In principle, for the $R\mathrm{VO}_3$ compounds, they can all contribute to different extents, depending on the ion R and the system's temperature. Properties particular to this family of compounds will now be discussed.

The RVO_3 family

In vanadium oxides RVO_3, where R is Y or a rare earth, V is in the 3+ oxidation state with two electrons in the t_{2g} d orbitals (t_{2g}^2 configuration). They have the same spin direction according to Hund's-rule coupling, giving a total spin $S = 1$. These oxides crystallise in a perovskite structure, with $GdFeO_3$-type distortions increasing from La- towards Y-based compounds [108]. At room temperature they can be described by a *Pbnm* orthorhombic unit cell with lattice constants of $a \approx b \approx c/\sqrt{2}$. However, at lower temperatures, these vanadates undergo a cooperative structural transition (of second order typically) to space group $P2_1/b$. This very fact indicates the presence of unquenched orbital degeneracy, suggesting that underlying $GdFeO_3$-type distortions are indeed not sufficient to remove it. The structural transition temperature ($T_{\rm str}$ or $T_{\rm OO}$) can be close to the magnetic one ($T_{\rm N}$ or $T_{\rm SO}$), as in the case of $LaVO_3$ [119, 121], or quite separated from it, as in $LuVO_3$, YVO_3 and $GdVO_3$ [119, 122–125]. It is accepted that the xy orbital is static below $T_{\rm OO}$ and accomodates one of the two magnetic electrons. The other electron occupies the doublet yz/zx. This gives an orbital degree of freedom to the system, with an orbital pseudospin operator $\tau = 1/2$ associated with the two possible states d_{yz} and d_{zx}. Therefore, orbital ordering & quantum fluctuations are expected to play an important role in the physics of RVO_3 [108]. A common theme for this category of compounds is to order spins and orbitals in C- and G-types, according to the empirical Goodenough-Kanamori rules: a C-type orbital ordering (OO) is compatible with a G-type spin ordering (SO) and vice versa [119,126]. This can be explained from the nature of the superexchange as discussed previously. If orbitals of adjacent ions overlap strongly, the superexchange is antiferromagnetic, as in fig. 4.4 (b) or (d) (C-type OO, G-type SO). However, there may be a situation with zero overlap of filled orbitals but a large overlap of a filled orbital of one ion with a vacant orbital of its neighbour. The intra-atomic exchange interaction $J_{\rm H}\boldsymbol{S_1} \cdot \boldsymbol{S_2}$ lifts the degeneracy in this case and spins

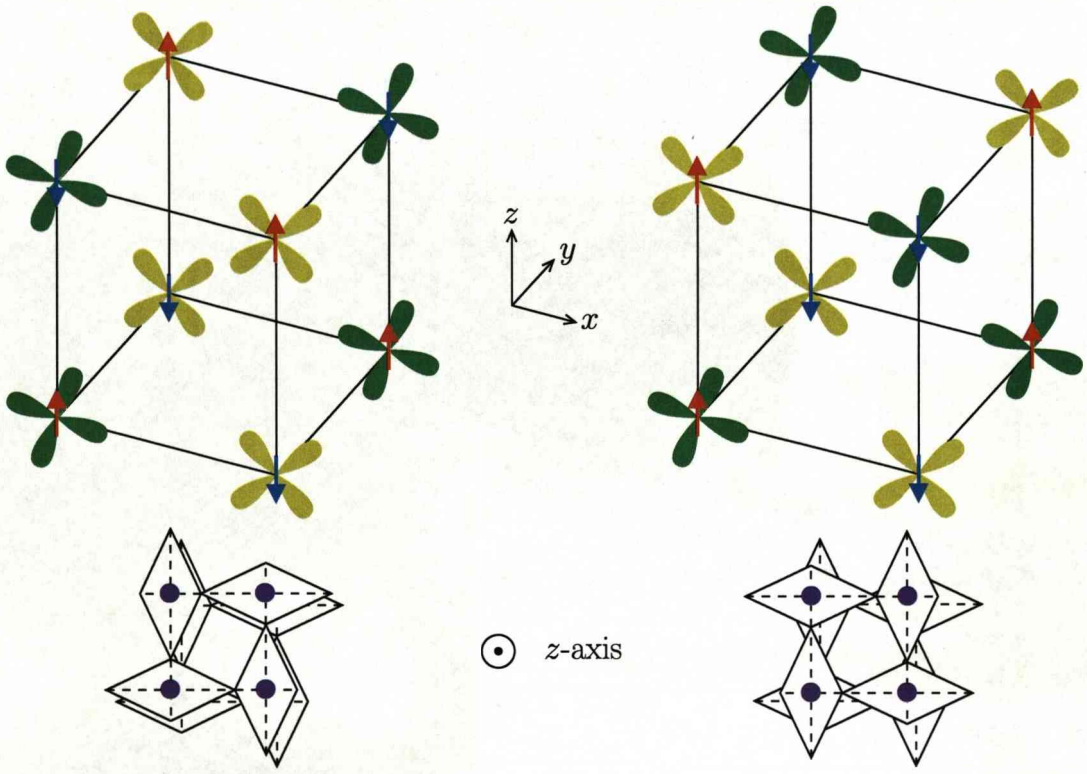

Figure 4.6: Structures of spin and orbital patterns most commonly adopted by $R\mathrm{VO}_3$ compounds. Part (a) shows a C-type OO and G-type SO (top), together with the cooperative JT distortions in the ab plane, showing an "in phase" V-O bonds arrangement (bottom). Part (b) shows a G-type OO and C-type SO, with V-O bonds 90° out of phase. Orbitals in green and yellow are yz and zx respectively, while the commonly occupied xy ones are not plotted. Vanadium sites are in purple, with oxygens at the corners of octahedra not shown for clarity.

are ferromagnetically aligned according to Hund's rules, as in fig. 4.4 (f) (G-type OO, C-type SO) [105]. These configurations are shown in fig. 4.6, together with the V-O bonds that are arranged (a) in phase for C-type OO and (b) 90° out of phase for G-type OO [127]. $R\mathrm{VO}_3$ compounds adopt these two different states of fig. 4.6 depending on the R-site ion and temperature, i.e. both configurations can be observed in the same compound.

Usually, the total energy of a magnet in a magnetic field is lowest when the magnetic moment is aligned parallel to the magnetic field. However, upon weak-field cooling (or warming), some $R\mathrm{VO}_3$ compounds (R = La, Y, Sm, Nd, Gd, Er) exhibit a magnetisation opposite to the applied magnetic field at a certain temperature T_R [124, 128–130]. This phenomenon, known as magnetisation reversal, is common in ferrites with two or more magnetic sublattices, but it is unusual in the case of $R\mathrm{VO}_3$, particularly for R = Y, La and Lu, due to the magnetic equivalence of all the V^{3+} ions. The sequential spin and orbital phase transitions were first suggested through this canted-spin moment reversal observation, with a net magnetisation caused by the tilting of the antiferromagnetic moments [131]. The response of the orbital moment to the forces generated at the phase transition can abruptly reverse the Dzyaloshinsky-Moriya vector so as to create a canted spin in the direction opposite to the applied field below T_R. For the case of YVO_3, a single-ion magnetic anisotropy had to be included in the model [129, 132] since there is no structural change at T_R. These two spin canting mechanisms (single-ion magnetic anisotropy and Dzyaloshinsky-Moriya coupling) produce moments in opposite directions and the competition between them can lead to the observed magnetisation reversal. In an attempt to uniformly explain this phenomenon for all $R\mathrm{VO}_3$ compounds, L.D. Tung took a different approach. He argues that inhomogeneities caused by defects in the orbital sector can reverse the magnetisation by producing some random field spins in an infinite antiferromagnetic network [124].

Specifically for GdVO_3, the orbital ordering transition occurs at $T_\mathrm{OO} \sim 199$ K, followed by an antiferromagnetic spin ordering of the vanadium moments at $T_\mathrm{SO} \sim 118$ K. In the magnetically ordered region, there is another transition at $T_\mathrm{M} \sim 8$ K, associated with the ordering of the Gd moments. The magnetic state below T_M is history dependent, showing up in different jumps in the magnetisation along the a-axis, but only when warming the sample through T_M. More specifically,

the zero-field cooling magnetisation can be seriously affected by the presence of an inevitably trapped field in the superconducting solenoids of the SQUID magnetometer, suggesting the presence of different domain arrangements [125]. This magnetic memory effect is a unique feature of $GdVO_3$ among other orthovanadates, making it an interesting system to study its transitions as a function of applied field. The overall aim is to link the lattice, orbital and spin degrees of freedom for this rich-phase-diagram system. Here we consider the zero-field phases.

4.2 Experimental procedure

$GdVO_3$ single crystals with well-defined faces were grown by L.D. Tung at the University of Warwick, by means of the floating zone technique, using a high temperature xenon arc furnace. $GdVO_3$ powder is prepared first, and then pressed and annealed at 1500° C under a flow of Ar, in order to get single crystals.

The neutron scattering experiment was performed on the hot four-circle diffractometer D9 at the ILL, with an Eulerian cradle sample holder and a small two-dimensional position-sensitive detector. This instrument is ideally suited for measuring the crystal structure and the magnetic ground state of this absorbing system, with $\sigma_{abs}^{Gd} = 49700$ barns. A Cu(220) monochromator was used, giving a nominal wavelength value of $\lambda = 0.51$ Å for our setup. The $GdVO_3$ single crystal ($m = 145.4$ mg) was carefully glued by Garry McIntyre to a V/Al pin with Kwik-Fill, a material traditionally used to polyfill cars. For the room-temperature data collection (295 K), the pin with the sample was placed straight into the beam on a goniometer head (see figure below). Further complete data sets were collected at 2, 50 and 150 K with the crystal, still on the pin, transfered to a 2K displex cryostat, which was mounted on the phi circle of the Eulerian cradle.

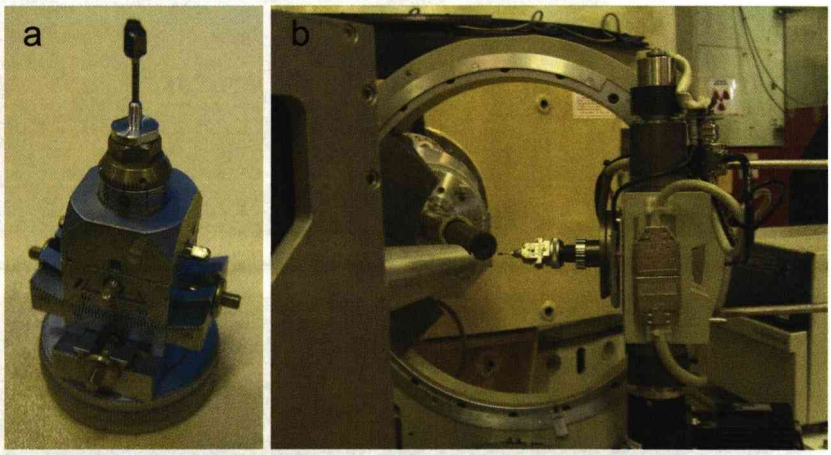

Figure 4.7: $GdVO_3$ single crystal (a) mounted on a goniometer head and (b) placed on the Eulerian cradle of D9.

The x-ray scattering experiment was performed at the BM28 beam line (XMaS) at the ESRF, Grenoble. This instrument is optimised for single-crystal diffraction measurements and has an incident energy range of 2.3 keV to 15 keV. For our purposes, we "tuned" to the vanadium K-edge, which is the electron binding energy of a 1s electron. Its nominal value for the natural form of the element is $E = 5.465$ KeV. A $GdVO_3$ single crystal with a mosaic spread of $\sim 0.07°$ was glued with (thermally) conducting silverpaint on a Cu base. This was in contact with a closed-cycle cryostat ($10\ \text{K} < T < 300\ \text{K}$), with the top of the system covered by a semi-spherical beryllium cap, in order to produce an insulating vacuum but also to allow for x-rays to reach the sample. The whole configuration was mounted directly on the phi circle of the Huber diffractometer of the instrument, allowing for orientations in any direction (see figure below). The linear polarisation analysis was performed with a PG crystal analyser. For the energy needed ($E = 5.465$ KeV), the (004) plane of PG was used, giving a diffraction condition with θ_{Bragg} close to 45° for the PA arm. The geometry used, allowed the selection of $\sigma - \sigma$ and $\sigma - \pi$ photon polarisations, by simply rotating the PA arm by 90°. The crystal, cut and polished along the (011) face (in $Pbnm$), was mounted so that it could be rotated around the scattering vector $\boldsymbol{Q}$ by changing the azimuthal angle phi of the Huber diffractometer.

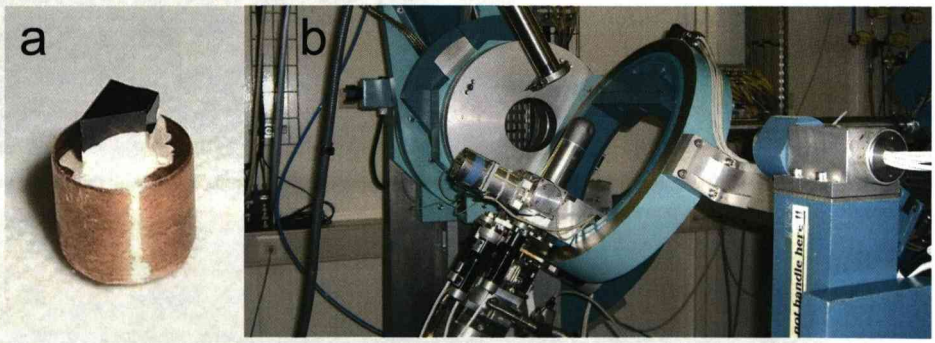

Figure 4.8: For the resonant x-ray experiment on $GdVO_3$, (a) the crystal was glued with silverpaint on a Cu cylinder and then (b) placed in a closed-cycle cryostat with a Be cap, on the Huber diffractometer at XMaS.

4.3 Results

4.3.1 Neutron diffraction measurements

The perovskite structure class has attracted considerable attention, beginning with the discovery of the magnetic properties in the rare-earth orthoferrite series in the 50's. Because of the great variety of possible elements, a huge number of these compounds are know, most of which are TMO and fluorides. They have a distorted perovskite structure, with the majority of them adopting the orthorhombic arrangement first found in $GdFeO_3$. The revival of interest in these compounds due to the discovery of high T_c superconductivity in Ba-doped La_2CuO_4, as well as orbital and magnetic ordering phenomena, brought about systematic reexaminations of these structures [121, 123].

Neutron diffraction offers some advantages over x-ray methods with regard to the determination of the oxygen parameters in the $GdVO_3$ structure. Furthermore, the greatly improved reflection-resolving power of single-crystal neutron diffraction makes it the preferred technique. Measurements were taken at 4 different temperatures (295, 150, 50 and 2 K), in order to examine all phases of $GdVO_3$. The crystal structure refinements were carried out by Garry McIntyre, using the least-squares refinement Cambridge Crystallography Subroutine Library (CCSL) package [133]. To reduce the strong absorption of the natural Gd we used the short neutron wavelength $\lambda = 0.5138(2)$ Å, refined by using reflections of a high-quality Ge crystal. In general b_{Gd} is complex, given by $b_{0,Gd} + b'_{Gd} + ib''_{Gd}$, where $b_{0,Gd}$ is the potential scattering term and b'_{Gd}, b''_{Gd} are the wavelength-dependent anomalous terms. However, it turns out that for centrosymmetric structures and around this wavelength, the term involving b''_{Gd} can be ignored [134, 135]. The refinement of the Gd scattering length gave $b_{Gd} = b_{0,Gd} + b'_{Gd} = 1.142(9) \times 10^{-12}$ cm^{-1} which is consistent with other determinations near this wavelength [134, 136]. The effect of absorption on integrated intensities was corrected by using the attenuation

	295 K *Pbnm*	150 K $P2_1/b$	50 K $P2_1/b$	2 K *Pbnm*	2 K $P2_1/b$
a [Å]	5.3484(6)	5.3380(7)	5.3417(5)	5.3371(7)	5.3371(7)
b [Å]	5.6252(7)	5.6412(8)	5.6465(7)	5.6501(8)	5.6501(8)
c [Å]	7.6428(8)	7.6110(10)	7.5963(9)	7.5967(10)	7.5967(10)
α [deg]	90	90	90	90	90
Gd					
x	0.98320(14)	0.98244(10)	0.98207(10)	0.98181(11)	0.98184(11)
y	0.06354(13)	0.06465(12)	0.06508(13)	0.06558(10)	0.06537(11)
z	0.25	0.25042(17)	0.25034(19)	0.25	0.25053(27)
$B_{11}/B_{\rm is}$	0.316(26)	0.1506(84)	0.0716(93)	0.0562(88)	0.0606(88)
B_{22}	0.273(23)				
B_{33}	0.305(22)				
B_{12}	-0.040(18)				
V1					
(x, y, z)	$(0, 1/2, 0)$	$(0, 1/2, 0)$	$(0, 1/2, 0)$	$(0, 1/2, 0)$	$(0, 1/2, 0)$
$B_{\rm is}$	0.30	0.15	0.15	0.30	0.15
V2					
(x, y, z)		$(0, 0, 1/2)$	$(0, 0, 1/2)$		$(0, 0, 1/2)$
$B_{\rm is}$		0.15	0.15		0.15
O1					
x	0.10031(29)	0.10076(20)	0.10064(21)	0.10067(22)	0.10080(22)
y	0.46791(27)	0.46795(24)	0.46831(27)	0.46849(20)	0.46834(24)
z	0.25	0.25119(35)	0.25037(41)	0.25	0.25057(61)
$B_{11}/B_{\rm is}$	0.494(47)	0.310(29)	0.217(30)	0.215(15)	0.228(15)
B_{22}	0.552(50)	0.413(43)	0.340(50)		
B_{33}	0.319(38)	0.157(35)	0.191(41)		
B_{23}		0.021(80)	-0.012(98)		
B_{13}		-0.092(55)	-0.008(65)		
B_{12}	-0.046(37)	-0.012(29)	-0.027(32)		
O2					
x	0.69585(18)	0.70010(37)	0.70093(35)	0.69533(15)	0.70001(53)
y	0.30034(17)	0.30596(40)	0.30632(45)	0.30070(14)	0.30591(43)
z	0.05118(14)	0.05134(26)	0.05299(32)	0.05285(11)	0.05104(41)
$B_{11}/B_{\rm is}$	0.420(33)	0.310(45)	0.162(46)	0.243(11)	0.212(30)
B_{22}	0.365(33)	0.290(58)	0.254(69)		
B_{33}	0.571(30)	0.300(58)	0.321(68)		
B_{23}	-0.065(27)	-0.189(57)	-0.262(68)		
B_{13}	0.061(25)	-0.002(41)	0.021(46)		
B_{12}	-0.069(24)	-0.075(42)	-0.078(48)		
O3					
x		0.30957(37)	0.31041(36)		0.30929(53)
y		0.70426(41)	0.70572(46)		0.70410(44)
z		0.55223(27)	0.55063(30)		0.55332(42)
$B_{11}/B_{\rm is}$		0.264(45)	0.220(44)		0.219(31)
B_{22}		0.328(60)	0.261(69)		
B_{33}		0.250(56)	0.274(69)		
B_{23}		-0.088(57)	-0.146(69)		
B_{13}		-0.090(42)	0.028(48)		
B_{12}		-0.069(41)	-0.095(47)		
Popul. of		0.7481	0.7275		0.6480
Domains.		0.2519	0.2725		0.3520
R_W	5.381	5.215	5.558	4.921	5.019
Observat.	610	842	1116	676	676
Basic Var.	24	34	34	12	19

Table 4.1: Structural refinement results for $GdVO_3$. The room temperature and 150, 50 K data were refined in the *Pbnm* and $P2_1/b$ spacegroups respectively. At 2 K, no significant difference in the fit quality is observed between the two spacegroup refinements.

coefficient $\mu = 0.74$ mm^{-1}.

Refinements of the diffraction patterns at room temperature (295 K) were performed in the orthorhombic space group *Pbnm* (standard setting *Pnma*). At 150 and 50 K, best agreement is obtained by using the $P2_1/b$ monoclinic spacegroup, with the angle α fixed at 90°. As we will see in the next section, this spacegroup choice is crucial in giving the correct theoretical energy lineshape calculations for measured RXS spectra. At 2 K, it is not conclusive whether one should use the *Pbnm* or $P2_1/b$ settings, since both refinements yield very similar residuals. Under these circumstances, a crystallographer is inclined to use the simplest cell, i.e. the one with the higher symmetry. All of these results are summarised in table 4.1. Note that due to the small scattering power of the vanadium atoms, an isotropic thermal parameter $B_{\rm is}$ was fixed, and it was not allowed to vary during the refinements. The anisotropic thermal parameters B_{ij} (in Å^2) have the form $e^{-h^2B_{11}/4a^2 \ldots - 2hlB_{13}/4ac \ldots}$, with B_{13} and B_{23} for the Gd and O1 atoms in *Pbnm* equal to zero for symmetry reasons [123]. The weighted R factor is defined as $R_W(F) = (\sum[1/\sigma^2(F_o)](F_o - F_c)^2 / \sum[1/\sigma^2(F_o)]F_o^2)^{1/2}$, where F_o and F_c are the observed and calculated structure factors. For the *Pbnm* spacegroup (standard notation *Pnma*, No. 62), the general equivalent Wyckoff position is 8*d*, given by: $\pm(x, y, z)$, $\pm(1/2 + x, 1/2 - y, -z)$, $\pm(1/2 - x, 1/2 + y, 1/2 - z)$ and $\pm(-x, -y, 1/2 + z)$. In $P2_1/b$ ($P2_1/b$ 1 1, standard notation $P2_1/c$, No. 14), the general position is on 4*e*: $\pm(x, y, z)$ and $\pm(1/2 + x, 1/2 - y, -z)$.

The 295 K results are in excellent agreement with the x-ray scattering determinations of Pickardt *et al.* [137], who investigated this system's structure at room temperature. For the $P2_1/b$ refinements, we allowed for twinning, i.e. rotations around the *b*- or *c*-axes (for this spacegroup). A variable domain proportion gave significant improvement, however the similarity to a domain proportion 3/4 : 1/4 is striking and puzzling. Unless some external force favours the population of one domain we should have an approximate 1:1 ratio of domain populations after the

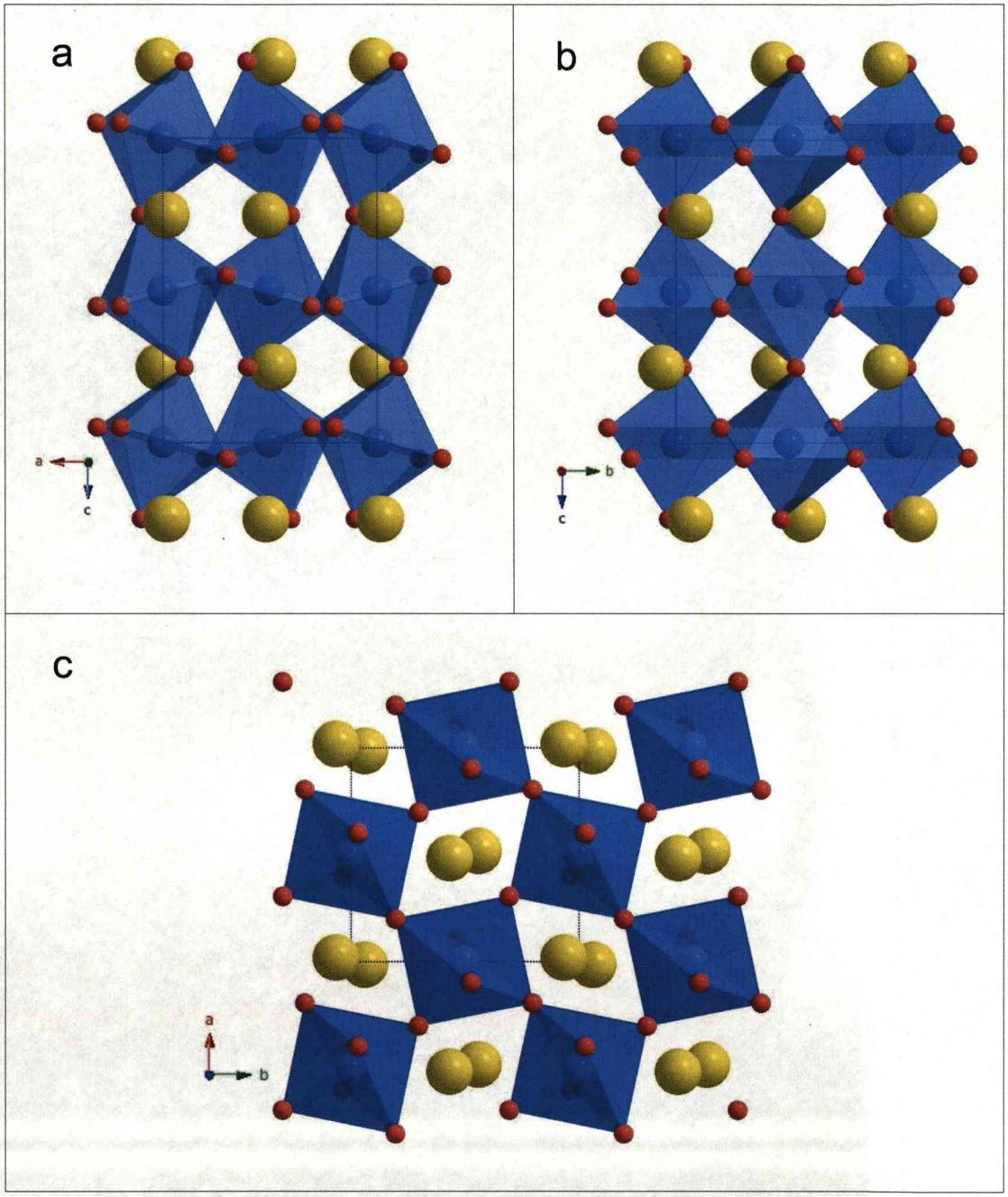

Figure 4.9: Crystal structure of $GdVO_3$ at room temperature. The three different views show the V octahedra (in blue) surrounded by 6 corner-shared O ions (in red). The ionic radii of V and Gd (in yellow) differ, giving rise to the so-called $GdFeO_3$-type distortions. An orthorhombic spacegroup (*Pbnm*) is needed to describe this structure.

transition from orthorhombic to monoclinic.

Three projections of the $GdVO_3$ crystal structure at room temperature are shown in fig. 4.9, where one can observe the $GdFeO_3$-type distortions (cf. with the ideal cubic perovskite structure, fig. 1.1(a)). The vanadium cations are octahedrally coordinated by six oxygen anions building a three-dimensional network of corner-sharing VO_6-octahedra. The vanadium octahedra are tilted, as a result of the "ionic size effect", i.e. the influence of the relative ionic sizes. At room temperature, this is the principal cause of the deviations from the ideal perovskite structure.

Finally, some temperature dependencies of selected reflection intensities are presented in fig. 4.10. The $(\overline{3}\ 0\ 0)$ structurally forbidden reflection (part a), indicates a Néel temperature, or T_{SO}, at $\sim$ 118 K. The intensity of this forbidden peak gradually increases below T_{SO}, and is associated with ordering of the V^{3+} ions. Furthermore, its wave vector corresponds to a C-type magnetic structure. This fact was used in the modelling of the RXS experimental data, as we shall see. The $(\overline{3}\ 0\ 0)$ magnetic reflection approaches zero below $T_M \sim 8$ K, while the structurally forbidden (0 1 3), shown in part (b), appears to rise very rapidly and strongly below 8 K. At this temperature, the Gd ion moments become ordered. Our measurements showed that the magnetic scattering at 2 K is concentrated in satellite reflections, and the magnetic structure is in fact incommensurate. Unfortunately, due to this unexpected behaviour, it turns out that more data collection is needed for full magnetic refinements. Fig. 4.10(c) shows the (0 2 0) reflection, as an example of a structural peak which remains unaffected for the whole temperature range. The structural change from $Pbnm$ to $P2_1/b$ spacegroup at $\sim$ 199 K appears to have an effect on the (1 4 6) structural peak, shown in fig. 4.10(d). All these neutron results are in accordance with bulk thermodynamic measurements [119, 125].

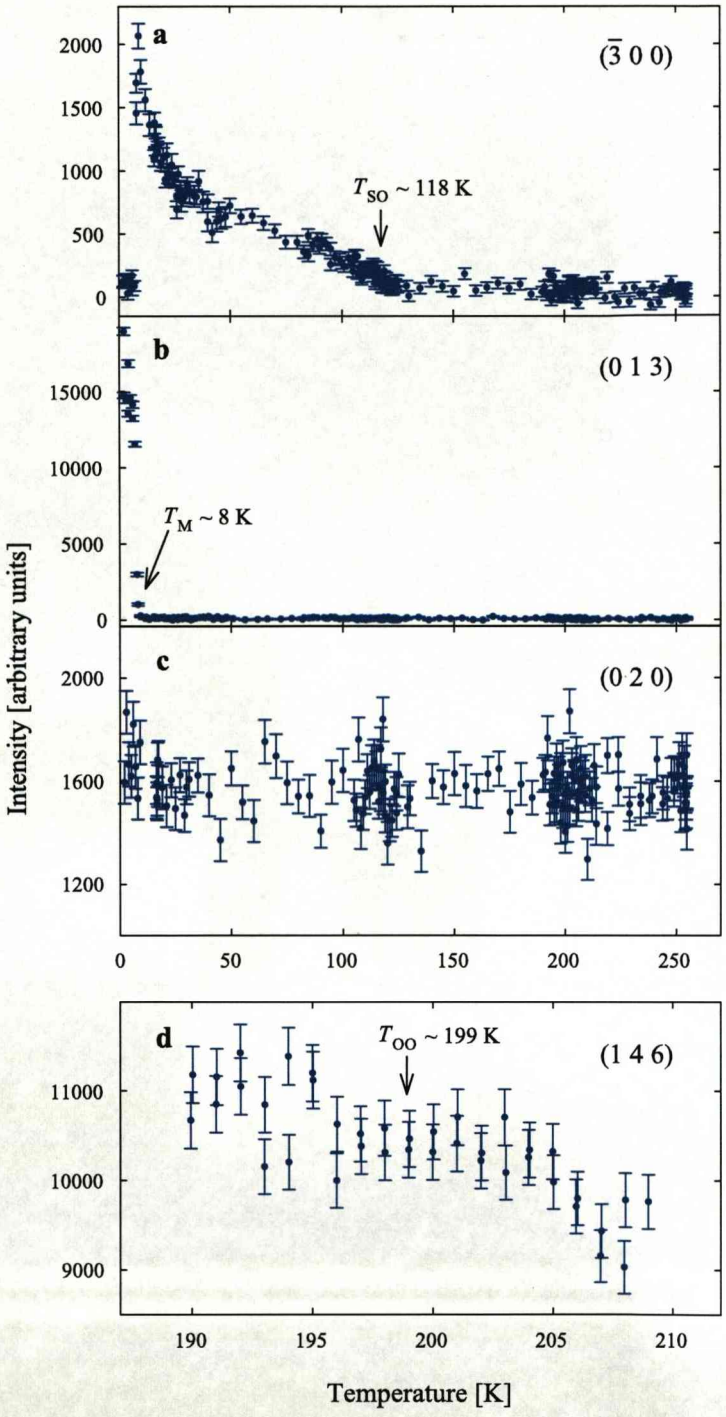

Figure 4.10: Temperature dependencies of selected reflections of $GdVO_3$. The magnetic ordering of V ($\sim$ 118 K) and Gd ($\sim$ 8 K) ions give rise to the structurally forbidden ($\overline{3}$ 0 0) and (0 1 3) peaks. The ($\overline{3}$ 0 0) wave vector corresponds to C-type SO. The (0 2 0) reflection shows no sign of alteration in this temperature range, while the (1 4 6) structural peak indicates the $Pbnm$ to $P2_1/b$ spacegroup transformation at approximately 199 K.

4.3.2 Resonant x-ray measurements

In section 4.1 we saw that $GdVO_3$ is an $S = 1$ Mott system with orbital degrees of freedom arising from the electrons' energy levels. By tuning the incident x-ray energy to the V K-edge we were able to deduce information about this "orbital ordering" in a different way to the neutron experiment at D9.

Figure 4.11(a) shows the absorption spectrum (XANES) of $GdVO_3$. The rising of the XANES near 5.482 keV is due to the V^{3+} K main edge (in agreement with [35]), which corresponds to the threshold energy of the $1s$-$4p$ intra-atomic dipole transition. The pre-edge ($1s$-$3d$ threshold energy) appears as a small peak at 5.474 keV, while the oscillations above the edge relate to the specific structure of the sample. The red line is a first-principles XANES calculation from the *FDMNES* package [11], in very good agreement with the data. See Appendix A for details of the *FDMNES* calculations.

In addition, scattering intensity with flipping of the polarisation plane of the incident radiation ($\sigma - \pi$ channel) was observed around the structurally forbidden (011) reflection of the crystal. Figure 4.11(b) shows the energy dependence of the intensity of this reflection corresponding to the propagation vector for G-type orbital ordering for this structure (fig. 4.6b). This scan features a resonance around the V^{3+} K main edge ($E = 5.482$ keV) and a small pre-edge feature seen as almost a 'shoulder' of the main peak ($E = 5.474$ keV, as in the fluorescence). Furthermore, a peak above the edge, at an energy $E = 5.494$ keV is observed, related to the particular structure of the compound. All of these experimentally measured characteristics are in perfect agreement with YVO_3 measurements [35]. The *FDMNES* calculation, shown as the red curve on the plot, is in good qualitative agreement with the experimental results, see Appendix A. Note that this is an *ab initio* calculation, and additionally it has no free parameters.

Let us now describe the origin of the resonant signal for the (011) reflection. The general mechanism for RXS is the virtual absorption of an incoming photon by

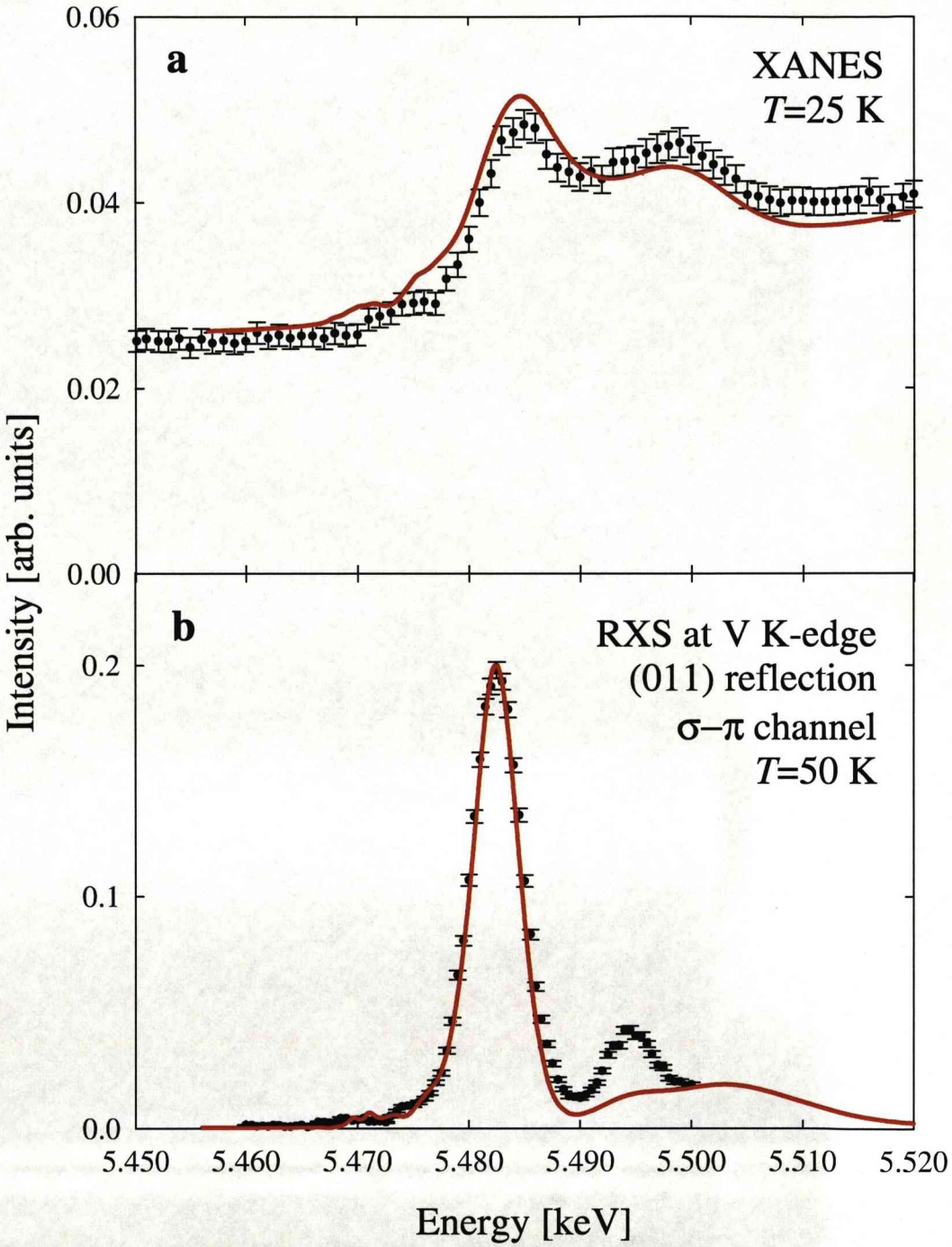

Figure 4.11: (a) Absorption spectrum (fluorescence) of $GdVO_3$ at 25 K, indicating the edge position ($\sim$ 5.482 keV). (b) Energy dependence of the (011) structurally forbidden reflection at 50 K in the $\sigma - \pi$ polarisation channel. Red curves are first-principles calculations from the *FDMNES* package [11]. Convergence was reached for a spherical cluster with a radius of 7 Å (see Appendix A). No parameters are allowed to freely vary in these *ab initio* calculations.

a core electron to promote an empty intermediate excited state. This subsequently decays to the same core hole emitting a second photon with the same energy as the incoming one (see section 2.1.3 for more details). The excited electron is sensitive to any anisotropy of the environment, and this is the key characteristic that is used to extract useful information from this process. For $GdVO_3$, the excitation of the V photoelectron from the $1s$ state to empty $4p$ states (split in their y and x, z components by an energy Δ due to some interaction with the surroundings [6, 10]) gives rise to the resonant scattered intensity observed here. This intensity is proportional to Δ^2 at the forbidden reflections and is sensitive to the difference between the atomic anomalous scattering factors (ASF) of the two orbitally ordered sublattices (with reference to fig. 4.6). By analogy with calculations for V_2O_3 [8], the origin of the splitting Δ is due to some coherent Jahn-Teller distortion of the oxygen octahedra surrounding the V atoms that accompanies the orbital ordering.

The temperature dependence of the order parameter of the orbital ordering, as measured by the intensity of the (011) reflection at the the V^{3+} K main edge ($E = 5.482$ keV) normalised to the (022) structural reflection, is shown in fig. 4.12. Note that the secondary peak above the edge ($E = 5.494$ keV) follows exactly the same T dependence (not shown), i.e. the ratio between the main and secondary peaks is constant as a function of temperature. The red curve of the figure is a power-law fit to the data, yielding $T_{OO} \sim (200 \pm 7)$ K, in agreement with heat capacity measurements [125]. There is a small remnant background above this temperature of unknown origin, but constant in magnitude. However, the main (secondary) peak shifts by +2 eV (-2 eV) sharply above T_{OO} and stays at this energy for temperatures up to 290 K. This might be suggesting that this background is of different origin to the RXS signal measured below T_{OO}. Furthermore, the orbital ordering transition is accompanied by an increase in the intensity of the fundamental (022) reflection by a factor of ~ 1.7 above T_{OO}. This reflects

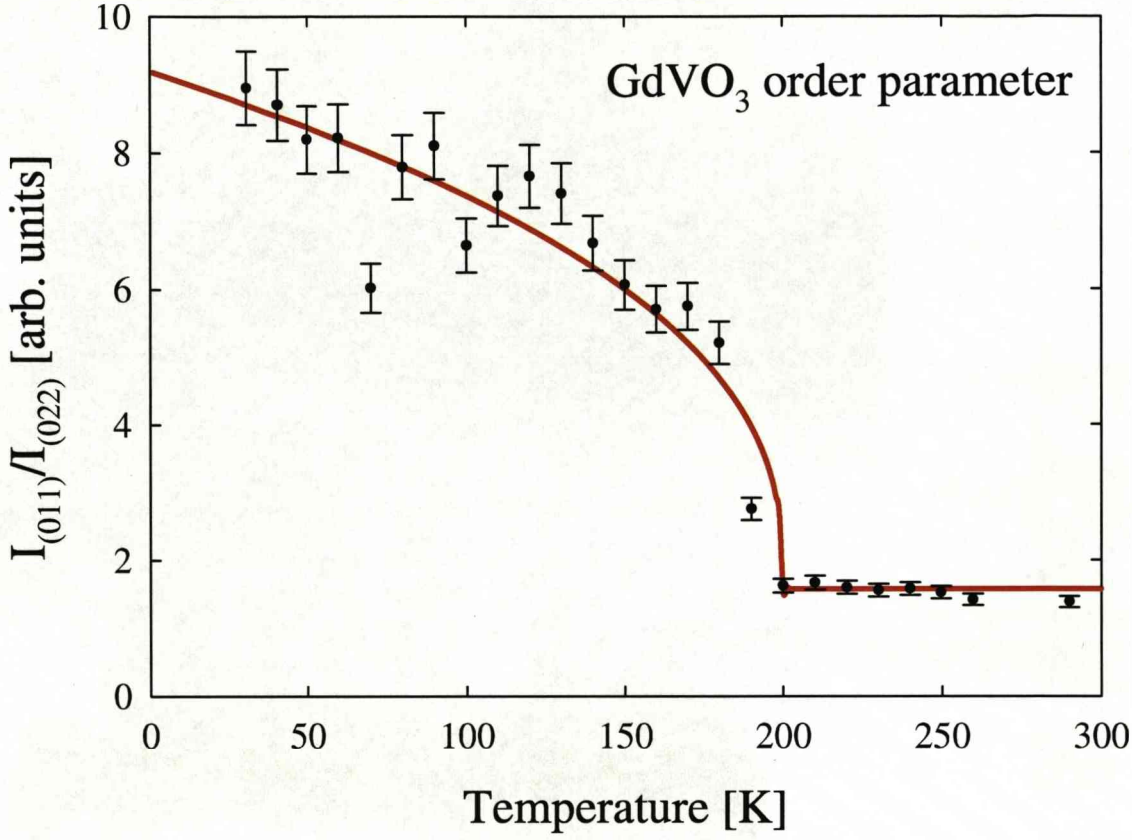

Figure 4.12: Temperature dependence of the normalised intensity of the orbital ordering reflection (011) of $GdVO_3$ at the vanadium K main edge. The red curve is a power-law fit to the data, yielding $T_{OO} \sim 200$ K. Measurements were performed in the $\sigma - \pi$ channel.

the structural phase transition from $P2_1/b$ to $Pbnm$ space groups, as observed in the neutron experiment. Besides the enhancement, resonant scattering from orbital ordering - being anisotropic (tensorial) scattering arising from the structure - is expected to exhibit another characteristic feature, related to the azimuthal angle ϕ of the crystal. Conventional x-ray scattering intensity, not being related to anisotropic electronic structures, does not depend on this angle. Since the synchrotron radiation is linearly polarised, the azimuthal angle ϕ, denoting the rotation of the sample around the scattering vector, determines the direction of the electric vector of the incident beam, $\boldsymbol{E}_i$, in the crystallographic co-ordinates.

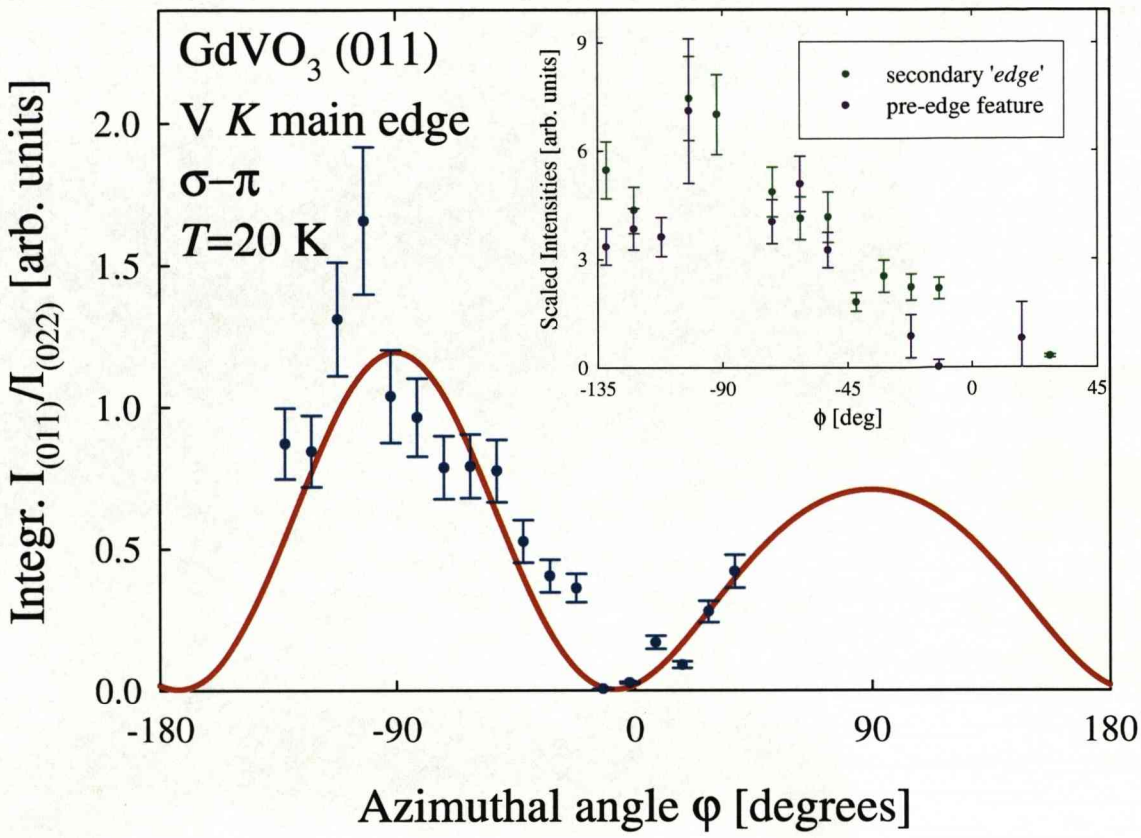

Figure 4.13: Azimuthal-angle dependence of the orbital ordering reflection (011) of $GdVO_3$, normalised by the fundamental reflection (022). Main edge is at $E = 5.482$ keV, with the red curve being the $FDMNES$ calculation. The inset shows the secondary ($E = 5.494$ keV) and pre-edge ($E = 5.474$ keV) peaks, which follow the same ϕ-dependence as the main edge.

The dependence of the resonant scattering with respect to these symmetry considerations is shown in fig. 4.13. This plot is again for the (011) reflection at $\sigma - \pi$, measured at the V^{3+} K main edge ($E = 5.482$ keV) and at 20 K. The integrated intensity has been normalised with the intensity of the fundamental structural (022) reflection in order to correct for small variations due to the sample shape and location as it is rotated around ϕ. The azimuthal angle $\phi = 0°$ corresponds to the configuration in which the a-axis [(100) reflection] points towards the incident beam. The resonant scattering characteristic oscillation of the (011) peak

for $GdVO_3$ approaches zero near $\phi = 0°$. It is important to note that the pre-edge feature at $E = 5.474$ keV as well as the secondary peak at $E = 5.494$ keV follow exactly the same azimuthal dependence, shown in the inset of fig. 4.13. This is a strong indication that all these resonant peaks, including the pre-edge, are of the same type of transitions. The solid red curve on the main data of fig. 4.13 is a theoretical calculation by *FDMNES*, in excellent agreement with the experiment. The lineshape in fig. 4.13 arises from dipolar transitions. Quadrupolar transitions would give a different azimuthal dependence. In fact, we have calculated the quadrupolar contribution using *FDMNES*, and it is found to give a negligible contribution at all energies.

Finally, we performed high $\boldsymbol{Q}$-resolution measurements in order to investigate the extent (domain size) of the ordered orbitals in comparison to the structure. Radial scans of the (011) and (022) reflections give the same width in $\boldsymbol{Q}$. Correlation lengths ξ were obtained from the full-widths at half-maximum (FWHM) using the formula $\xi = 2\pi/\text{FWHM}$. The orbital order correlation length is found to be $\xi_{orbital} \sim 600$ Å at 50 K. In other cases, such as $Pr_{1-x}Ca_xMnO_3$, the orbital correlation length is shorter than the structural and charge ordering [7].

4.4 Discussion: RXS technique and data interpretation

Resonant x-ray scattering mechanisms in orbitally ordered systems

One of the main issues for RXS as a probe to detect the orbital ordering, is the mechanism of scattering from the orbitally ordered state, i.e. the mechanism for the anisotropic tensor elements of the atomic anomalous scattering factor $f' + \mathrm{i}f''$. For vanadates, the incident x-ray is usually tuned around the V K-edge causing dipole transitions (virtual excitations) from the initial $1s$ to the intermediate $4p$ orbitals which contribute to, and under certain circumstances dominate, the scattering cross section. An enhanced sensitivity to the charge anisotropic distribution around the resonant ion gives access to orbital (and charge) degrees of freedom. However, the transition itself does not have direct access to the $3d$ states which are responsible for the orbital ordering. A mechanism is therefore needed that brings an anisotropy to the anomalous scattering factor in the orbitally ordered phase, and this is where the debate starts. A possible scenario for RXS in orbitally ordered $3d$ TMO is the **Coulomb mechanism** [138, 139]. A direct Coulomb interaction between the ordered $3d$ and the conduction band $4p$ states of the transition ion would split the degenerate p orbital levels, bringing an anisotropy to the ASF. The second mechanism, which seems to be more and more popular, is the **coherent Jahn-Teller distortion** of the oxygen octahedra surrounding the transition ions that accompanies the orbital ordering [10, 140, 141]. In any case, it is believed that the $4p$ states are split by an energy Δ (also known as *orbital parameter*), due to orbital ordering. As a result, virtual excitations give resonant scattered intensity proportional to Δ^2 at forbidden reflections, which is sensitive to the difference between the ASF of the two orbitally ordered sublattices [6, 10]. Linear dichroism is an essential element in the scattering process, and in fact the beam polarisation needs to be coupled with the different polarisations of the

orbitals in order to get RXS signal. Note that in absorption spectra (XANES), one measures the sum of the scattering from different atomic sites (and not the difference as in RXS), so linear dichroism is supressed.

Another way of looking at the problem is that one cannot easily separate the orbital ordering from the lattice distortions, as it seems that these effects occur concomitantly. In other words, there is no need to emphasise the distinction between *direct* and *indirect* observations of the orbital ordering, in terms of whether one looks at the orbitals themselves or the JT distortions. Whatever the mechanism of the p splitting might be, it is generally agreed that these RXS experiments do measure the correct orbital parameter. However, theoretical *ab initio* calculations can be used to give information on the relative sizes of the two effects, namely the Jahn-Teller distortions and the direct Coulomb interactions. It has been shown that for manganites, the resonant diffracted intensities due to the two mechanisms differ by a factor of ~ 2 orders of magnitude, in favour of the JT distortions [10].

Goodenough-Kanamori classical picture

Neutron diffraction data yielded a C-type magnetic structure for the V lattice of $GdVO_3$, with a Néel temperature of ~ 118 K (fig. 4.10(a)). Furthermore, the (011) RXS orbital reflection, whose order parameter is shown in fig. 4.12, arises from a G-type orbitally ordered structure, stable below ~ 200 K. Hence, the standard "Goodenough-Kanamori" empirical rules are found to hold below the Néel temperature of this oxide (and above $T_M \sim 8$ K). According to this classical picture, the orbitals and spins are static, as shown in fig. 4.6(b).

Relative importance of energy lineshapes and azimuthal dependencies - *FDMNES* calculations

The experimental signs of orbital ordering are strong reflections from forbidden Bragg peaks (magnetic RXS will generally be much weaker), azimuthal dependence and polarisation dependence (distinctively in the $\sigma - \pi$ channel). Generally, the orientational alignment of the orbitals yields a different periodicity in the crystal, which is twice the fundamental structural periodicity for the case of alternating orbitals along an axis. RXS is sensitive to that, and is able to distinguish between the two inequivalent sites. Furthermore, because of the tensorial character of the ASF, the scattered x-ray has both σ- and π-polarised components, which are separated by the analyser crystal. Thomson scattering has no azimuthal dependence and also does not rotate the incident beam's polarisation.

Conditions limiting possible reflections (extinction rules) listed in the *International Tables for Crystallography* apply only to point scalar scatterers placed at the atomic positions or to atoms with spherically symmetric electron-density distributions. However, distortions of the electronic states by neighbouring atoms can lead to nonzero structure amplitudes of the 'forbidden' reflections [142]. A known example is the 222-type reflection in the diamond structure, which is excited by chemical bonding distortions or by anharmonic thermal motion. Non-spherical parts of the atomic electron density can be considered as small 'pseudo-atoms' in general positions, hence violating standard extinction rules. Other such examples of Bragg-forbidden reflections are supplied by pure magnetic scattering or orbital ordering. All of these effects will exhibit an azimuthal dependence and so one should not draw particular emphasis on the ϕ-dependence as a unique characteristic of an orbital ordering peak. Hence, **an azimuthal dependence reflects purely the space group symmetry of a crystal** and could arise due to various reasons. Now, in resonant conditions, it becomes possible to detect Bragg-forbidden reflections, that are extinct off-resonance because of the pres-

ence, in the space group, of non-symmorphic symmetry elements (glide plane, screw axis). The reason for this extinction violation is that near an edge (where electrons cannot be considered as free), a scalar description of the x-ray interaction with matter is not adequate, instead one deals with anisotropies described by a tensorial ASF. Consequently, the ASF tensor changes the orientation of its principal axes under the glide-plane and screw-axis symmetry operations of the space group so that the ASF tensors of different (though symmetry-related) atoms in the unit cell cannot compensate each other. Hence, such reflections depend on the difference between the atomic scattering amplitudes on the ions linked by these non-symmorphic symmetry elements. As the Thomson factors f^0 cancel out in this way, such Bragg-forbidden reflections are sensitive just to the changes of the ASF, that depend on the anisotropies in the electronic and magnetic distributions. Orbital and charge ordering phenomena occur due to these kind of reflections [8,142]. This is the exact point where one can appreciate the results of powerful *ab initio* calculations such as ones from the $FDMNES$ package [11,143]. This is because experimentalists, backed-up with theory, can distinguish between different signals and decide which contributions are most important by performing test calculations. Energy lineshapes turn out to be possibly the most crucial elements in the investigation of $GdVO_3$, and related compounds. The reason for that is that by running the $FDMNES$ code with different settings, we always observed the same basic energy pattern: a dipole resonant peak at the edge and a pre-edge feature, whose intensity is at least 1-2 orders of magnitude smaller. Our calculations for YVO_3 and those performed for V_2O_3 [8], showed exactly the same qualitative result. Furthermore, for the case of YVO_3, our calculations agree with the Noguchi *et al.* experimental data [35]. It is worth mentioning that this group measured exactly the same energy dependence (qualitatively) for YVO_3 as we did for $GdVO_3$, so it is not surprising that the same answer was found after modelling both datasets. The secondary peak above the edge (see fig. 4.11(b)) is

seen in both YVO_3 and $GdVO_3$ and is believed to arise from the particular details of the band structure. Hence, it is expected that for other materials more peaks might appear after the edge (or perhaps none). The pre-edge feature is generally believed to arise from quadrupole-quadrupole or even mixed dipole-quadrupole effects [142]. This would, in our case, imply that one probes the d states, through quadrupolar $1s \rightleftharpoons 3d$ transitions. The beauty of $FDMNES$ is that it allows the user to choose between dipolar, quadrupolar or mixed spectra calculations. It turns out that for $GdVO_3$, even the pre-edge peak is of dipolar origin (with negligible quadrupolar contributions). This can happen in a crystal that does not have a centre of symmetry (or loses it under for example a structural phase transition). In this case, one can measure the p states because they overlap with the d ones ($3d - 4p$ hybridisation). In other words, some p states are in the same energy as the d states would normally be. To summarise, a very important result obtained from theoretical analysis of $GdVO_3$ RXS, is that all of the signal in the energy scans is of dipolar origin. This agrees with the fact that the ϕ-dependences of the main, secondary and pre-edge peaks are the same (fig. 4.13). Indeed, the tensor elements of the quadrupolar term will be different to those of the dipolar, hence the azimuthal dependencies will have different periodicities. In addition, **energy scans are more powerful in distinguishing orbital ordering**, as azimuthal dependencies can often be misleading, especially if not theoretically simulated. Another interesting result is that the pre-edge is only a very small fraction of the main edge peak, in accordance with our simulations. This is in agreement with an extensive amount of work done on manganites [6,144–149], where the observed lineshapes are very similar to those of $GdVO_3$. However, experimental findings on V_2O_3 [5,150] disagree with the above picture. In these references, it is claimed that a pre-edge feature is seen as a sharp intense peak, and is attributed to a quadrupolar transition, hence direct evidence of orbital ordering. Furthermore, the dipole component at the edge position, which should be orders of magnitude

stronger, is not observed at all. The origin of this V_2O_3 signal was theoretically investigated with *ab initio* calculations which demonstrated that it could not be due to any kind of orbital ordering or charge anisotropy, but is magnetic [8].

To conclude, we emphasise that theoretical calculations are always important in interpreting data. The remarkable fit of the RXS signal of fig. 4.11(b) from *ab initio* calculations with no degrees of freedom, is such a case. These results agree with YVO_3 measurements [35], both experimentally and theoretically.

Chapter 5

Spin dynamics and orbital fluctuations in $LuVO_3$

5.1 Quantum effects in orbitally degenerate systems

In a classical approach to orbital physics, one usually assumes that long-range coherence of the orbital polarisation sets in below the cooperative orbital/Jahn-Teller transition temperature, and that the spin-exchange interactions on every bond are fixed by the Goodenough-Kanamori rules [105, 118, 126] (basic concepts given in section 4.1). Implicit to this picture is that the orbital splittings are large enough so that we can consider orbital populations as classical numbers. Such a classical treatment of static (fully ordered) orbitals is certainly justified when orbital order is driven by strong cooperative lattice distortions that lead to a large splitting of the - initially degenerate - orbital levels. In this limit, the orbital excitations are more or less localised high-energy quadrupole moment (or crystal-field) transitions, and therefore they effectively just renormalise the spin degrees of freedom. Other than that, they do not have much effect on the physical

properties of the system at low energy scales [1].

Quantum effects, however, might start to dominate the ground state properties and elementary excitations, when classical order is frustrated by some interaction that opposes the tendency of the orbitals to order. This *orbital frustration* is a very general property of t_{2g} and e_g cubic perovskite compounds. Specifically for t_{2g} systems, the electron-lattice interactions or oxygen octahedra distortions are weaker compared to e_g systems which have elongated orbitals along the V-O bonds. Suppressed t_{2g} Jahn-Teller distortions can often give rise to different and more interesting physics to the vanadates and titanates compared to manganites and cuprates, with e_g occupied orbitals. Another crucial point to make is that orbital frustration and related quantum effects are more pronounced because of the large, threefold degeneracy of t_{2g} levels, which enhances quantum effects. In addition to the frustration that is present in e_g systems, there also exists the possibility to form quantum singlets among t_{2g} orbitals. Therefore, quantum tunneling between different local orbital configurations may occur. For the high spin cubic vanadium oxides ($S = 1$) the spin-orbital frustration is thought to be resolved in the orbital sector with the help of low-dimensional orbital fluctuations [1]. G. Khaliullin, P. Horsch, A.M. Oleś *et al.* have developed an impressively sophisticated and complex theory for cubic TMO, where both spin and orbital degrees of freedom are incorporated [1,120,151,152]. It accounts very well for the exotic measured properties of YVO_3, and also, as we shall see, for our experimental results on $LuVO_3$. An attempt is made here to describe this theory, giving particular emphasis to high spin t_{2g} orbitally degenerate systems (cubic vanadates).

The origin of the orbital frustration is quite different from that in a conventional geometrically frustrated spin system without orbital degeneracy. In the latter case, spin interactions are of the same form for all bonds and it is a special lattice geometry that brings about spin frustration. A typical example of such a highly degenerate classical system is one with a triangular lattice spin configura-

tion. The distinct feature of the orbitally degenerate models is that frustration occurs for conventional, e.g. simple cubic, lattices. The reason is that the very form of the orbital interaction depends on the bond direction in the crystal. In that respect, this is similar to the square lattice vanadates studied in chapter 3, where cross-bond magnetic exchange is found to be stronger than the nearest-neighbour one. For these systems, there seems to be a preference for the superexchange to be stronger when orbitals lie approximately in a line and not at 90° to each other. However, it is still a two-dimensional case of frustration. For distorted perovskites, the driving mechanism is the spatial anisotropy of the orbital wavefunctions. Interactions on different bonds require the population of different orbital states and hence compete. A bond directionality of the interactions is a special feature of orbital models which leads to a large degeneracy of the low energy states and pronounced quantum effects. In this way, the orbital degeneracy provides a new root for frustrated quantum models in three dimensions [1].

The model for high spin (two electrons forming $S = 1$) t_{2g} orbital systems - applied here on $LuVO_3$ - includes formation of quasi-one-dimensional orbital chains along the c-axis of the structure, as well as dimerisation of the spin-orbital chains due to an *orbital Peierls effect*. These give rise to a dimerised C-type spin order with fluctuating orbitals at an intermediate temperature regime, 84 K $< T <$ 107 K for $LuVO_3$. At lower temperatures, $T <$ 84 K, an interplay between these spin-orbit superexchange effects and the $GdFeO_3$-type distortions (lattice effects) gives rise to a G-type spin order, with orbitals ferro-aligned along the c-axis [1,108]. **The important point to take away is that the underlying orbital fluctuations have important consequences on spin interactions which control spinwave dispersions. These can be experimentally measured, unlike orbital excitations (so far), and provide tests to theories.**

5.1.1 Formation of one-dimensional orbital chains

The superexchange interactions between the $S = 1$ spins of V^{3+} ions arise from the virtual charge excitations $d_i^2 d_j^2 \rightleftharpoons d_i^3 d_j^1$ on a given bond $\langle ij \rangle$, with the hopping t allowed only between *two out of three* t_{2g} orbitals, termed as *active* and shown in fig. 1.4 [3, 120, 152]. By neglecting Hund's splitting for the excited states, i.e. for the limiting case of

$$\eta = \frac{J_{\mathrm{H}}}{U} \to 0 \tag{5.1}$$

the system Hamiltonian becomes [1, 108, 120]:

$$\mathscr{H}_0 = J \sum_{\langle ij \rangle \| \gamma} \frac{1}{2}(\boldsymbol{S}_i \cdot \boldsymbol{S}_j + 1) \left(\boldsymbol{\tau}_i \cdot \boldsymbol{\tau}_j + \frac{1}{4} n_i n_j \right)^{(\gamma)} \tag{5.2}$$

where $J = 4t^2/U$ represents an overall superexchange energy scale, with t and U being the hopping integral and on-site Coulomb repulsion in the Hubbard model respectively. A constant nonmagnetic energy term of $-2J$ per V^{3+} ion is neglected. The spin-exchange interaction depends on the orbital occupation, as specified by the index γ which gives the orientation of the bond $\langle ij \rangle$ relative to the cubic axes a, b and c. Since each t_{2g} orbital is orthogonal to one cubic axis, yz, zx and xy orbitals can be alternatively labelled as a, b and c respectively. The operators $\boldsymbol{\tau}_i = \{\tau_i^x, \tau_i^y, \tau_i^z\}$ are defined in the orbital pseudospin subspace spanned by two orbital flavours which are active along a given direction γ. For instance, in the c direction the interactions follow from the electron hopping between the pairs of a and b orbitals (the active ones). The electron (or *orbiton*) densities at V^{3+} ions satisfy the local constraint $n_{ia} + n_{ib} + n_{ic} = 2$, where n_i denotes the number operator for constrained particles a_i, b_i, c_i (orbitons). The main feature of this model - as suggested by its Hamiltonian (5.2) - is the strong interplay between spin and orbital degrees of freedom. For example, the classical Néel state in (5.2) where $\langle \boldsymbol{S}_i \cdot \boldsymbol{S}_j \rangle = -1$ is infinitely degenerate in the orbital sector, thus strongly

frustrating the orbital order. A mechanism must lift this extra degeneracy. This is in contrast to the classical Goodenough-Kanamori picture, where the orbital and spin sectors are separated. There, the mutual coupling of the two sectors is treated as a static interplay between spin and orbital order parameters.

Let us now focus on possible quantum effects, by firstly considering a single bond along the c-axis. A crucial observation is that the lowest energy of $-J/2$ is obtained when the spins are ferromagnetic, and the orbitals a and b form a singlet, with $\langle \boldsymbol{\tau}_i \cdot \boldsymbol{\tau}_j \rangle^{(c)} = -\frac{3}{4}$. Thus, one finds a novel mechanism by which to obtain ferromagnetic interactions that works due to local fluctuations (orbital singlets) of a and b orbitals. In order to form ab orbital singlets along the c-axis, the condition $n_i^{(c)} = n_j^{(c)} = 1$ must be fulfilled, otherwise no $\boldsymbol{\tau}^{(c)}$ pseudospin can be formed. This implies that the second electron on both sites has to go to an *inactive* (xy) orbital. Thus, we arrive at the following picture for the superexchange bond along c:

- spins are aligned ferromagnetically
- one electron at each site occupies either an a or b orbital forming orbital pseudospins that bind into an orbital singlet
- the c (or xy) orbital has a stabilisation energy of about $-J/2$ - the energy that is required to break an ab orbital singlet - and accomodates the remaining second electron

Generally, an orbital that is inactive in a particular direction induces an AF coupling in the other two directions, due to the conventional Pauli principle mechanism operating even in the absence of orbital degeneracy. Thus, spin interactions are strongly FM (supported by orbital singlets) along c, while the other bonds are AF. Now, all directions are equivalent in cubic perovskites, resulting in a frustration. This can be resolved, and the cubic degeneracy is lifted by gaining quantum energy mainly from the orbital sector. A particular classical spin configuration maximises the energy gain from orbital fluctuations and is preferred.

Indeed, orbital singlets with $n_{ia} + n_{ib} = 1$ may form on bonds parallel to the c-axis, with the second electron occupying the third t_{2g} orbital ($n_{ic} = 1$) thereby controlling the spin interactions in the ab-planes. In this way one arrives at spin order of the C-type, with FM chains along the c-axis that stagger within ab-planes. This mixes both the FM (driven by the orbital singlets) and AF (induced by the electron residing on the static inactive orbital) interactions [1, 108].

Given this spontaneous cubic symmetry breaking with fluctuating a, b orbitals and a stable c orbital at a lower energy (giving rise to a C-type spin structure), the superexchange Hamiltonian can be simplified. The quantum dynamics of the system are dominated by the $\tau = \frac{1}{2}$ orbital pseudospins rather than the larger, more classical $S = 1$ spins. In the orbital sector we get [1, 108]:

$$\mathscr{H}_{\rm orb} = J_{\rm orb} \sum_{\langle ij \rangle \| c} (\boldsymbol{\tau}_i \cdot \boldsymbol{\tau}_j) + J^{\perp}_{\rm orb} \sum_{\langle ij \rangle \| (a,b)} (\tau^z_i \tau^z_j). \tag{5.3}$$

For realistic values of the parameter $\eta = J_{\rm H}/U$ for vanadates, $J^{\perp}_{\rm orb}/J_{\rm orb} < 0.1$. Hence, one-dimensional orbital pseudospin chains are only weakly coupled to each other (quasi-one-dimensional orbital chains). Orbital excitations of the model propagate mostly along the c-chain direction.

Spin interactions, and hence spinwave dispersions, depend upon the orbital fluctuations. In the spin sector we obtain interactions $J_c(\boldsymbol{S}_i \boldsymbol{S}_j)$ and $J_{ab}(\boldsymbol{S}_i \boldsymbol{S}_j)$ on c- and (a, b)- bonds respectively. The results involve orbital pseudospin correlations, given in [1, 152], where one observes that the ferromagnetic coupling along the c-axis is strongly enhanced by orbital fluctuations.

Comparing all coupling constants in both spin and orbital sectors, one finds that the dominant one is the Heisenberg-like $J_{\rm orb}$ term of eq. (5.3). Cubic frustration is resolved by the formation of orbital chains with Heisenberg dynamics for which a large quantum energy is gained. C-type spin ordering and one-dimensional pseudospin formation are intimately connected and support each other.

5.1.2 Entropy driven spin - orbital dimerisation

It was shown above that C-type spin order results in quasi-one-dimensional orbital chains which accumulate a large quantum energy, thereby stabilising the state. In addition, orbitals show weak three-dimensional staggered ordering driven by small interchain couplings in the orbital Hamiltonian (5.3). It is well known that the Heisenberg chain may show another kind of ordering - *Peierls order* - where the chain dimerises, breaking the translational symmetry*. For spin systems showing a *spin-Peierls transition*, the driving force of the intrinsic lattice instability is the magnetoelastic coupling between the one-dimensional electronic structure and the three-dimensional lattice vibrations. A distortion of the lattice influences the magnetic energy, and dimerisation gives rise to two unequal alternating exchange couplings. The chain possesses an energy **gap** between the **singlet** ground state and the lowest lying band of **triplet** excited states [1, 72].

However, it turns out that the spin-orbital coupling may induce dimerisation of the spin-orbital system even *without* electron-phonon coupling. This is known as an *orbital Peierls effect*, and is contrasted to the normal (electronic) or spin-Peierls distortions that usually require an extra degree of freedom (e.g. phonons) to couple with electrons or spins respectively and trigger the dimerisation instability [1]. For the one-dimensional model of section 5.1.1, orbital singlets were the minimum energy solutions (ground state). The first excited state is given by a spin singlet/orbital triplet and is separated by a gap of $J/4$. Therefore, a strong orbital dimerisation in the ground state is expected, leading to alternating FM-AF spin-exchange couplings. In this *orbital valence bond* (OVB) state, the orbital singlets and uncorrelated bonds along c alternate. The driving force of this effect

*Normally, the dimerisation of a one-dimensional chain of atoms can occur spontaneously because the electronic energy saved by opening up a **gap** in the energy spectrum near the **Fermi surface** can outweigh the elastic energy cost of the dimerisation. This is the *Peierls instability* of electrons in a band, accompanied by a metal-insulator transition. The corresponding real space distortion is known as *Peierls distortion*. A one-dimensional electron gas is unstable with respect to this electronic Peierls instability [72].

is gain in orbital quantum energy. Note that in this model, Hund's coupling $J_{\rm H}$ (or η) is zero, and perfect dimerisation is expected. On the other hand, for sufficiently large values of η (greater than ~ 0.15), a FM spin order along the c-axis will be stabilised, and the C-type spin state with weak orbital ordering will be restored (uniform or pure ferrochain). This also results in an isotropic Heisenberg antiferro-coupling of the orbitals. Clearly, there will be a competition between a pure ferrochain (i.e. C-type spin structure at large η) and the spin/orbital dimer phase (at smaller η). Theoretical calculations give η_c, the critical coupling for the zero temperature phase transition, somewhere in the range $0.10-0.11$. This is just slightly below realistic values for vanadium oxides, with estimated $\eta \sim 0.12-0.13$ for cubic vanadates. Since Hund's coupling parameter in these systems is close to the critical value, there is strong competition between uniform (C) and dimerised (OVB solid consisting of decoupled orbital dimers with total spin 2) states. The two phases are very close in energy, and this may affect thermodynamic properties for entropy reasons. The gain of spin entropy due to the dimerisation lowers the free energy $F = \langle H \rangle - TS$ and may stabilise a dimer state with alternating weak and strong ferro-bonds along the c-axis. Dimerisation of the spin-orbital chains occurs due to the *orbital Peierls effect*, in which thermal spin fluctuations along c play the role of lattice degrees of freedom, while the critical behaviour of the Heisenberg-like orbital chains is a driving force. The effect is dynamical in this one-dimensional case. However, a weak but finite coupling between the spin-orbital dimers on different c-chains is present in real crystals. Dimers on different chains will therefore correlate and may form a coherent dimer crystal. Doubling of the magnetic unit cell along the c-axis is then expected [1, 108, 120, 151, 153].

We may conclude that the t_{2g} spin-orbital model with high spin values shows an intrinsic tendency towards the formation of weakly coupled orbital chains followed by dimerisation of these low dimensional spin-orbital structures. The dimerisation is driven by a critical behaviour of the orbital sector, according to the orbital

Peierls effect, in which thermal spin fluctuations trigger the dimerisation instability in the spin-orbital system. This theory was firstly used in explaining the exotic properties of YVO_3, and is applied here on $LuVO_3$ spin excitations.

5.2 Experimental procedure

A $LuVO_3$ single crystal of mass $m \sim 4$ g was grown by L.D. Tung at the University of Warwick, by means of the floating zone technique, as briefly descibed in section 4.2. Figure 5.1 shows the $LuVO_3$ crystal used, with some indexed directions (in the *Pbnm* space group) from Laue diffraction.

The inelastic neutron scattering experiment was performed at the thermal neutron three-axis spectrometer IN8 at the ILL, with a Si(111) monochromator and a PG(002) analyser. This instrument has a high neutron flux and is optimised for inelastic single crystal measurements over a wide range of energy and momentum tranfers. The sample was covered with Al foil and tied with Al wires in an holder made from an Al grid that could be bent to the desired shape. GE varnish - effective down to very low temperatures - was used to glue the crystal on the sides of the mount for further stability. The triple-axis instrument was used in a constant k_f mode, with final wavevectors $k_f = 2.662$ Å^{-1} and 4.1 Å^{-1}. The instrumental energy resolution at the elastic position is $\sim$ 1 meV and $\sim$ 3 meV respectively. Note that as energy transfer increases the resolution becomes worse, reaching about 10-15% of ΔE. The spectrometer was used in the W configuration, as this focuses the resolution ellipsoid giving good resolution in desired directions. A single ^{3}He detector was used for the data collection and a closed-circuit refrigerator (displex), with 10 K $< T <$ 300 K was used to measure the spin excitations at 50 K and 95 K. PA is not possible on this instrument, so measurements were also performed at 160 K (paramagnetic phase) in order to distinguish the magnetic signal. Magnons disappear above T_N, while phonons increase with T.

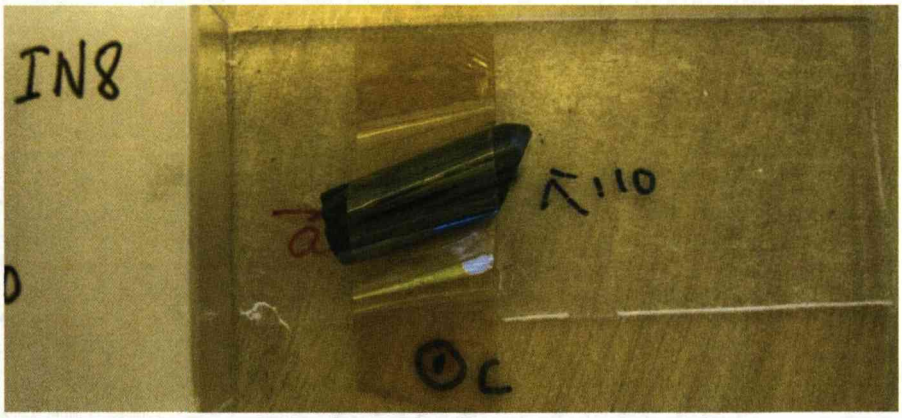

Figure 5.1: The $LuVO_3$ single crystal used for the IN8 spin-excitation measurements.

5.3 Results: spinwave dispersions in *G*- and *C*-phases

The room temperature crystal structure of $LuVO_3$ is described by the orthorhombic space group *Pbnm* with lattice parameters $a = 5.2172(1)$ Å, $b = 5.5433(1)$ Å and $c = 7.5113(2)$ Å [122]. However, the vanadium atoms in this distorted perovskite compound are situated in an almost cubic lattice, the *pseudocubic subcell*, with lattice parameters $a/\sqrt{2} \sim b/\sqrt{2} \sim c/2$. For simplicity, in aligning the crystal at the experiment and in analysing the data we used this latter simple 'cubic' cell. As mentioned in section 5.1, $LuVO_3$ exhibits two different magnetic phases, a low temperature G-type spin phase and an intermediate temperature C-type spin ordered phase (see fig. 4.2). These transitions have been seen in SQUID magnetometry as well as in neutron diffraction measurements [154] with temperature ranges $T < 84$ K for the G-type spin ordering and 84 K $< T <$ 107 K for the dimerised C-type spin phase. Furthermore, heat capacity measurements suggest an orbitally ordered phase below $T_{OO} \sim 180$ K [154].

Our single crystal inelastic measurements were taken at 50 K and 95 K, in order to extract the exchange couplings from magnetic excitations in both phases.

G-AF phase magnons

Excitations in the low temperature magnetic phase of the $LuVO_3$ single crystal were measured at 50 K, where the sample is known to adopt a G-type spin ordering, shown in fig. 4.2. Figure 5.2 shows a representative energy scan at $\boldsymbol{Q}$ = (0.5 0.5 1.4). This phase turned out to give strong intensity magnons, so it was not essential to subtract any higher temperature measurements (above the magnetic phases) in order to get the correct energy positions in the absence of polarisation analysis. Energy scans were taken at various positions in $\boldsymbol{Q}$, along the high symmetry (0.5 0.5 L) and (H H H) directions. The spinwave dispersion extracted from the energy positions of these data sets is shown in fig. 5.3. The magnons in this low temperature phase follow a simple anisotropic Heisenberg model, derived in [152] using linear spinwave theory.

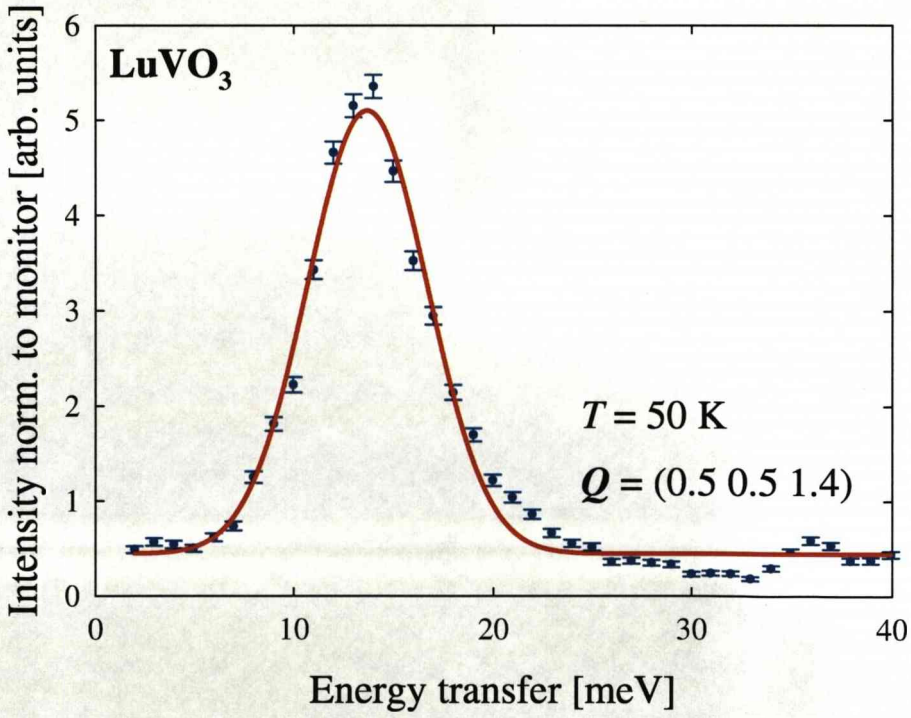

Figure 5.2: A typical inelastic neutron scattering profile in the low temperature phase of $LuVO_3$, at $\boldsymbol{Q}$ = (0.5 0.5 1.4). Note that $L = 1$ is equivalent to $L = 0$ and so on.

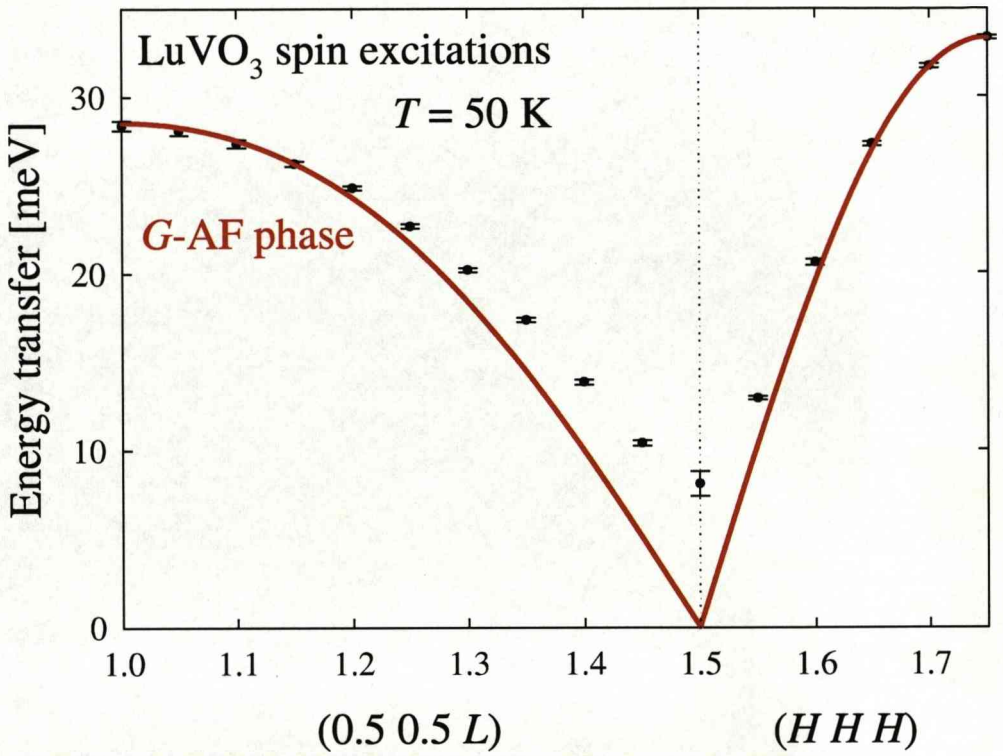

Figure 5.3: Magnon dispersion in the G-type spin phase of $LuVO_3$, at 50 K and along (0.5 0.5 L) & (H H H). The fit yields antiferromagnetic exchange couplings $J_{ab} \sim 6.32$ meV and $J_c \sim 4.02$ meV in the ab-plane and along the c-axis respectively. A zone-centre gap due to a single-ion anisotropy is not modelled here.

For the G-AF phase one finds the following dispersion law [152]:

$$\omega_G(\boldsymbol{Q}) = 2\{[2J_{ab} + J_c]^2 - [2J_{ab}\gamma(\boldsymbol{Q}) + J_c \cos(2\pi L)]^2\}^{1/2} \tag{5.4}$$

where

$$\gamma(\boldsymbol{Q}) = \frac{1}{2}[\cos(2\pi H) + \cos(2\pi K)] \tag{5.5}$$

and H, K, L are the Miller indices of the pseudocubic cell. The red model on fig. 5.3 is a fit for $J_{ab} = 6.32$ meV and $J_c = 4.02$ meV, both exchange couplings being antiferromagnetic (as required by a G-AF structure). The zone-centre gap is attributed to a single-ion anisotropy [151] and is not taken into account here.

C-AF phase magnons

The intermediate dimerised C-type magnetic phase of $LuVO_3$ (84 K $< T <$ 107 K) is of unusual nature, and can be explained according to the theory of G. Khaliullin, P. Horsch, A.M. Oleś *et al.* as described in sec. 5.1. Indeed, we were

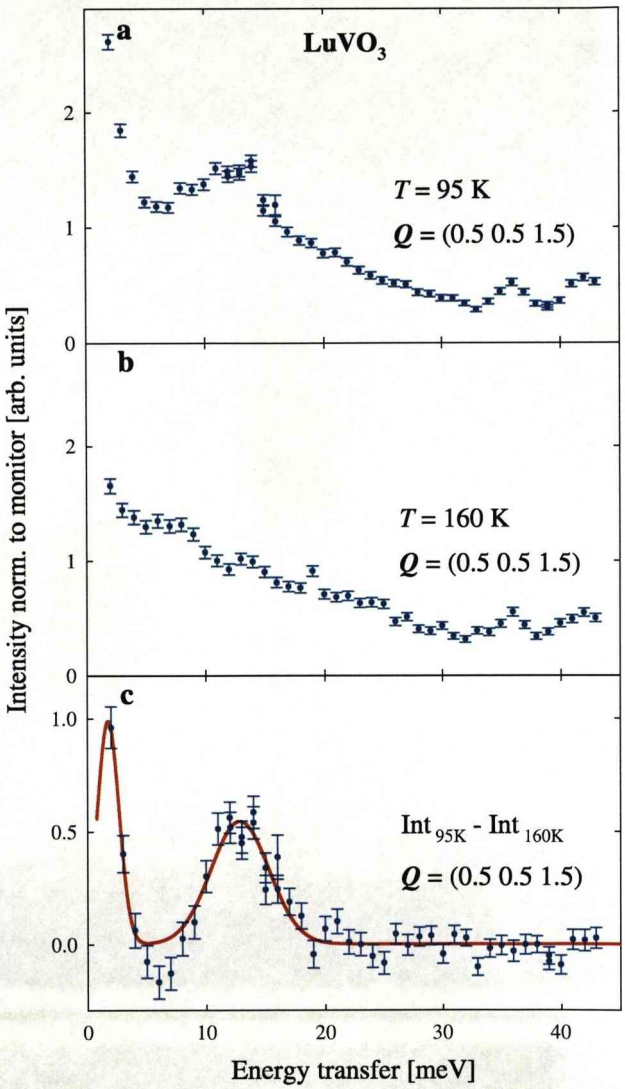

Figure 5.4: Typical dataset used for extracting the dispersion relation in the C-AF phase of $LuVO_3$. In part (a), the magnon contribution at 95 K is found to be weak, and a background (part (b), 160 K) has to be subtracted. Their difference, of magnetic origin, is shown in part (c) with the two peaks corresponding to acoustic and optical magnon branches.

able to model the spinwave dispersion again in the context of this model, as has been done previously for YVO_3 [151]. Excitations were measured at 95 K, with typical scans shown in fig. 5.4(a). No polarisation analysis was available, so it was necessary to measure any other signal that contributes to the weak magnetic scattering at that temperature. In order to do so, measurements were taken at 160 K, a temperature well into the paramagnetic phase but below $T_{OO} \sim 180$ K, to avoid possible structural transitions there. A representative scan is shown in fig. 5.4(b), where one can see that indeed the signal is comparable in magnitude with that at 95 K and had to be subtracted, resulting in fig. 5.4(c). Acoustic and optical magnon branches can be seen, something not compatible with a pure C-AF phase, suggesting a dimerisation of the quasi-one-dimensional orbital chains. Energy scans were taken along the (0.5 0.5 L) and (H H 1) reciprocal cubic lattice directions ($L = 1$ corresponds to $L = 0$ etc.), giving the spin excitations of figure 5.5. The spectrum is split into optical and acoustic magnons with a small gap of $\sim$ 1.5 meV between the branches. This splitting can be described by assuming two different ferromagnetic exchange bonds that alternate along the c-direction. The dispersion law in the dimerised C-AF phase, neglecting the single-ion and symmetric superexchange anisotropies, has been calculated in [152] according to linear spinwave theory:

$$\omega_{C\pm}(\boldsymbol{Q}) = 2\{[2J_{ab} + |J_c| \pm J_c(\cos^2(2\pi L) + \delta_s^2 \sin^2(2\pi L))^{1/2}]^2 - [2J_{ab}\gamma(\boldsymbol{Q})]^2\}^{1/2} \tag{5.6}$$

with $\gamma(\boldsymbol{Q})$ given by eq. (5.5), and the $\pm$ sign generating the two magnon branches. The spinwave dispersion is split by the anisotropy δ_s, giving rise to alternate FM exchange coupling constants $J_c^{1,2}$ in the c-direction with respect to the average value J_c, according to $J_c^{1,2} = J_c(1 \pm \delta_s)$. The fit of this dimerised C-AF model for $LuVO_3$ (shown as the red curves in fig. 5.5) yields $J_{ab} \sim 2.5$ meV (AF), $J_c \sim -1.7$ meV (FM) and the dimensionless spin anisotropy $\delta_s \sim 0.15$.

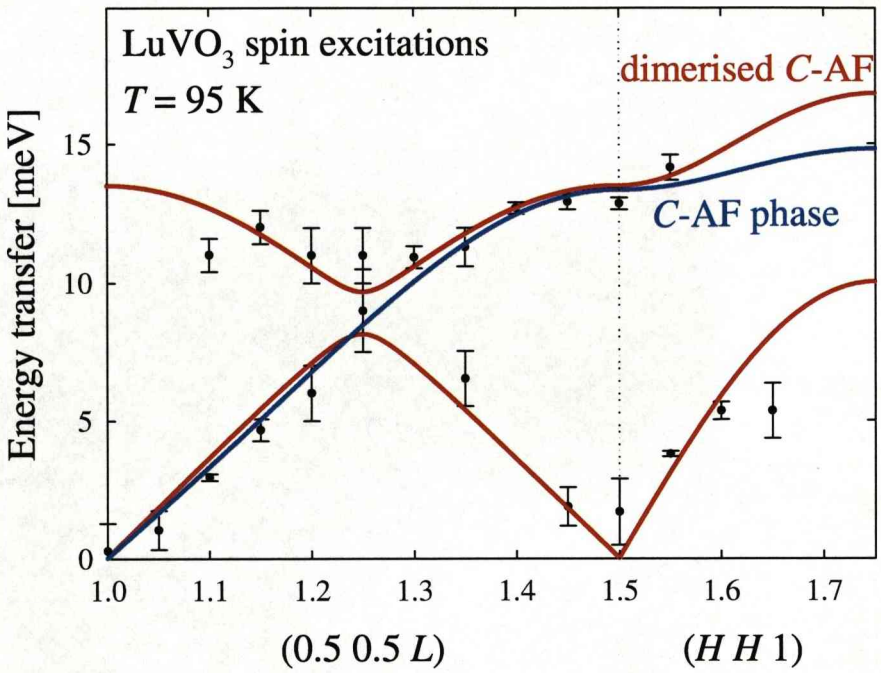

Figure 5.5: Spinwave dispersion of the intermediate dimerised C-AF phase of $LuVO_3$. The solid red curve corresponds to a fit with $J_{ab} \sim 2.5$ meV (AF), $J_c \sim -1.7$ meV (FM) and $\delta_s \sim 0.15$, according to eq. (5.6). Alternating stronger and weaker FM bonds across the c-axis are essential here. For comparison, the uniform FM C-AF model (solid blue curve) is also shown.

The spinwave dispersion for a pure C-AF type with uniform FM interactions J_c is given by [152]:

$$\omega_C^{(0)}(\boldsymbol{Q}) = 2\{[2J_{ab} + |J_c|(1 + \cos(2\pi L))]^2 - [2J_{ab}\gamma(\boldsymbol{Q})]^2\}^{1/2}. \qquad (5.7)$$

This result corresponds to an idealised structure where the observed alternation of stronger and weaker FM interactions along the c-axis is ignored. A fit for $J_{ab} = 1.6$ meV (AF) and $J_c = -2.1$ meV (FM) is shown as the blue curve of fig. 5.5 for comparison. Clearly, this does not correspond to the measured dispersion but only agrees with a fraction of the datapoints. The intermediate phase of $LuVO_3$ seems to be more complicated than a pure C-AF phase, violating the standard Goodenough-Kanamori rules.

5.4 Discussion: picturing physical processes in $LuVO_3$

The Mott-Hubbard model for t_{2g} electrons in cubic vanadates with large intraorbital Coulomb exchange interaction $U \sim 5$ eV and a smaller effective hopping element $t \sim 0.2$ eV (i.e. $U \gg t$) gives, to a first approximation, localised d electrons in a t_{2g}^2 configuration of a Mott insulator. However, in a second-order perturbative appoach, charge fluctuations $d_i^2 d_j^2 \rightleftharpoons d_i^3 d_j^1$ are present, although supressed. The kinetic energy term $\mathscr{H}_t$ of the spin-orbital Hamiltonian $\mathscr{H}$ arises from these hoppings, through the oxygen's $2p$ orbital path across V-O-V bonds. Two electrons at every V site are in the high-spin ${}^3T_2$ triplet ($S = 1$) state, stabilised by Hund's exchange $J_{\rm H} \sim 0.64$. Since $t \ll J_{\rm H}$, $\mathscr{H}_t$ can only contribute in virtual excitation processes which are responsible for the superexchange interactions [120].

Everything so far has been described within the superexchange context, neglecting effective orbital interactions induced by the oxygen distortions. These are particularly important, since in t_{2g} systems, **lattice effects** can compete with the **superexchange**, giving exotic transitions between C- and G-AF phases. Indeed, theoretical analysis within the charge-transfer model has shown that the two phases are energetically close [155], and one may thus expect that small changes of the thermodynamic potential could induce a first-order phase transition. VO_6 octahedra distortions are of two types: the $GdFeO_3$-type distortions that favour repeated orbitals along the c-axis and the alternating orbital order in the ab-planes favoured by a weak Jahn-Teller effect. Therefore, in addition to the superexchange $\mathscr{H}$, given by eq. (5.2) for $J_{\rm H} = 0$, two effective orbital interaction terms $\{V_c, V_a\}$ need to be included [152]:

$$\mathscr{H}'_{\rm orb} = -V_c \sum_{\langle ij \rangle \| c} (\tau_i^z \tau_j^z) + V_a \sum_{\langle ij \rangle \| (a,b)} (\tau_i^z \tau_j^z), \tag{5.8}$$

where $\tau_i^z \equiv \frac{1}{2}(n_{ia} - n_{ib})$ and both $\{V_c, V_a\}$ parameters are positive. These terms, when sufficiently large, induce the C-type orbital order, in the G-AF spin phase below $T_{\rm N2} \sim 84$ K for $LuVO_3$. The classical energy of the G-AF phase is lowered by the energy $-\frac{1}{4}(V_c + 2V_a)$ gained per site when the C-type orbital order sets in. In fact, the C-type OO enforces here the G-AF phase, showing a close interrelation of spin and orbital intersite correlations (Goodenough-Kanamori rules) [152]. We point out again that the first $GdFeO_3$-type term of eq. (5.8) describes a ferro-orbital coupling ($V_c > 0$) which competes with the orbital-Heisenberg $J_{\rm orb}$-term in the Hamiltonian (5.3). Furthermore, one expects that the $GdFeO_3$-like distortions are responsible for stronger orbital interactions along the c-axis, and the parameter V_c plays a more important role than V_a (quantifying the weak t_{2g} JT effect) in stabilising the C-type OO. In that respect, $LuVO_3$ is an important case, since the Lu ion has the smallest radius of the whole RVO_3 series and hence the associated $GdFeO_3$-type distortions are maximised for this compound. $LuVO_3$, like YVO_3, is believed to have η and $V_{c,a}$ parameters very close to a tricritical point in the (η, V) phase diagram [108, 152], hence there is a fine balance that can be easily tipped changing completely both the magnetic and orbital orders. For sufficiently large V, the G-AF phase is stable, while at larger values of η (and suppressed V's) the C-AF phase takes over. The OVB phase, with alternating strong FM bonds stabilised by orbital singlets and weak AF bonds, is stable for small values of $\{\eta, V\}$, but has not been experimentally observed yet.

Figure 5.6 summarises the various phases of $LuVO_3$ in terms of t_{2g} energy levels. At room temperature the V^{3+} environment is cubic, giving a triplet of degenerate orbital levels. As the temperature is decreased, at around $T_{\rm OO}$ or $T_{\rm str} \sim 180$ K, the crystal field induced by the structural transition lifts the degeneracy and breaks the cubic symmetry in the orbital space. The *inactive* xy orbitals are favoured below $T_{\rm str}$, while the remaining *active* yz and zx orbitals are nearly degenerate, leading to $n_{ic} \simeq 1$, $n_{ia} + n_{ib} \simeq 1$. In other words, the c orbitals

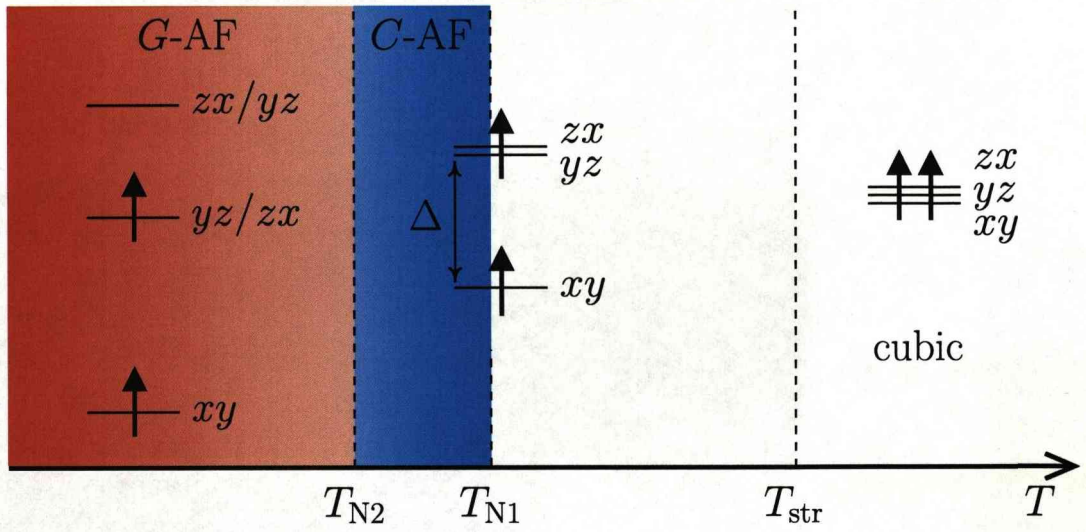

Figure 5.6: Energy splittings between t_{2g} orbitals in $LuVO_3$ for different phases across temperature. An orbital splitting Δ occurs below T_{str}, stabilising xy orbitals in the C-AF phase but also allowing for weak orbital fluctuations, an important element of the theory. Such fluctuations are quenched in the more classical G-AF phase, where $GdFeO_3$-type distortions become important [152].

are "condensed" while the other two represent the remaining t_{2g} orbital degree of freedom at every site. In this exotic phase, orbital ordering is not rigid, and the static Goodenough-Kanamori picture does not provide us with a good enough description. Instead, orbital fluctuations are needed to describe experimentally measured spinwave dispersions. One-dimensional orbital chains are formed here, minimising the system's energy, although they are intrinsically unstable towards *orbital Peierls* dimerisation. As a consequence, spin correlations alternate between stronger and weaker FM bonds in a dimerised C-AF phase, stable in the intermediate temperature range $T_{N2} < T < T_{N1}$. Large orbital entropy due to fluctuations in the C-AF phase can be released at T_{N2} and trigger another phase transition. The $GdFeO_3$-type distortions, which are very significant for $LuVO_3$, can further split the yz, zx doublet and favour a more classical G-AF structure. Spins are aligned AF across all axes, in a stabilised C-type OO pattern, according to the standard Goodenough-Kanamori rules.

Let us now discuss some unusual properties of $LuVO_3$, giving particular emphasis to the C-AF phase. Calculations for magnetic exchange constants in this phase [152] yield values that are larger by a factor of 2 compared to experimental ones. This puzzling feature can be explained in terms of the structural transition $T_{\rm str}$ as follows: the splitting Δ induced between the xy orbitals and the yz/zx doublet is not anticipated to be large enough to impose strict freezing of charge in the xy orbitals. Hence, some xy orbital fluctuations should still be present in the temperature regime $T_{\rm N2} < T < T_{\rm str}$. These fluctuations lead to local FM (AF) contributions in the ab-planes (along the c-axis), resulting in an effective reduction of the magnetic exchange constants [152].

According to the Goodenough-Kanamori rules (see RVO_3 section in 4.1), AF exchange is comparatively stronger than FM, which is weaker by a factor of $J_{\rm H}/U$ [105], i.e. an order of magnitude in the present case. However, from the spinwave results of $LuVO_3$, we deduced $J_{ab} \sim 2.5$ meV (AF) and average $J_c \sim -1.7$ meV (FM), violating the standard Goodenough-Kanamori rules. Furthermore, a gap in the spinwave dispersion of the C-AF phase is not a classically expected result, arising from the orbital chain dimerisation. The observed gap between optical and acoustic branches in $LuVO_3$ is smaller, ~ 1.5 meV, compared to the value of ~ 5 meV for YVO_3 [151]. In addition, the spinwave excitation spectrum of $LuVO_3$ in the G-AF phase (fig. 5.3) shows an asymmetry, with $J_{ab} > J_c$ (6.32 and 4.02 meV respectively), while the experimentally obtained values of YVO_3 are isotropic, with $J_{ab} \simeq J_c \simeq 5.7$ meV. This may help to tie down parameters in the theory [108, 120, 152]. The total energy scale of these systems in the low temperature phase is $J \sim 40$ meV for both compounds [120, 151, 156].

The ordering process of the intermediate phase in the orbital sector - the stabilisation of the xy orbital which absorbs one electron, and lifting the remaining degeneracy of xz/yz-doublet via quantum fluctuations - occurs as we saw cooperatively with the evolution of the C-type magnetic order. This picture would

break down *if* the JT coupling dominates, and nothing but a conventional 3D-classical ordering of xz/yz-doublets at some $T_{\rm str}$, independent of spin correlations, would take place in that case. The JT picture has also been applied to the problem [157, 158], although it contradicts optical conductivity spectra measurements [159] which show strong polarisation dependences. Large JT binding energies would give large orbital splittings which would in turn suppress the quantum nature of the orbitals. As a result, uniform spectral weights would be expected, not depending along the a, b, c crystal directions. The optical experiments [159] clearly indicate that the JT coupling is very weak and thus not sufficient to lock-in the orbitals [108].

To summarise, quantum fluctuations of orbital degrees of freedom in TMO are important and have to be taken into account in the explanation of various properties of these systems. Here, we were able to measure $LuVO_3$ spin excitations in both magnetic phases of the compound and model the C-AF structure in terms of a spin-orbital dimerisation and underlying spin fluctuations that control the magnetic exchange constants.

Chapter 6

Conclusions and future outlook

This thesis focusses on essentially two different classes of materials, studied microscopically with neutron and x-ray scattering techniques. All systems are specified by (pseudo)spin-$\frac{1}{2}$ operators, and hence quantum effects are expected to be highly active. Indeed, most of the properties measured are described in terms of frustration, as a result of enhanced quantum fluctuations.

The experimental success of the neutron investigations is primarily attributed to recent upgrades on D7, IN20, IN8 and D9, where data can be collected much faster and in a well-controlled sample environment. Specifically for D7, the recent increase by a factor of ~ 70 in the instrument's efficiency was crucial in measuring short-range spin correlations of weak ($S = \frac{1}{2}$) and dilute (1:14 atoms is magnetic) frustrated ferromagnets. For the resonant x-ray experiment, XMaS turned out to be an optimised and reliable instrument for studies of orbital ordering. A combination of high synchrotron-x-ray intensities, polarisation analysis, and a very stable & well-controlled environment were the key elements.

Theoretical input was of equal importance, especially in getting the best possible information from Y. Joly's spectroscopic *FDMNES* calculations [11]. Recently developed theories in spin-orbital models [1, 108, 120, 152], as well as the $J_1 - J_2$ compounds [74] were used and verified in the analysis procedure.

6.1 Frustrated square lattices

The vanadium oxides $Pb_2VO(PO_4)_2$, $SrZnVO(PO_4)_2$ and Li_2VOSiO_4 are quasi-two-dimensional magnets, well described by the spin-$\frac{1}{2}$ Heisenberg model on the square lattice with first (J_1) and second (J_2) neighbour interactions (eq. 3.1). Properties of these model magnetic systems were studied using neutron scattering techniques on powdered samples. In particular, the fact that these are low energy systems made it possible to integrate over energy transfer and measure the scattering function $S(Q)$.

The ground states of all compounds (measured at 1.5 K) were found to be collinear antiferromagnetic. The ordered moments were approximately 0.55, 0.5 and 0.42 μ_B for the Li_2VOSiO_4, $Pb_2VO(PO_4)_2$ and $SrZnVO(PO_4)_2$ compounds respectively. These low moments, characteristic of quantum disordered spin systems, are in line with the diffuse background coexisting 'below' the sharp magnetic Bragg reflections. Indeed, the substantial diffuse scattering intensity at low temperatures shows that there is considerable disorder. More specifically, the $Pb_2VO(PO_4)_2$ and especially the $SrZnVO(PO_4)_2$ phosphates have higher diffuse scattering component levels, and consequently higher degrees of frustration, compared to the Li_2VOSiO_4 (which has the highest $\mu_{ord.}$).

Magnetic coupling interactions are ususally determined from single crystal excitation measurements from the ordered phase. In the absence of single crystals, we obtained information on the magnetic exchange interactions from the spin correlations in the paramagnetic phase of powders. In order to do so, we measured quasielastic diffuse scattering of polarised neutrons, integrated over the particular energy transfers of our systems, at temperatures much higher than T_N but well below room temperature. For $Pb_2VO(PO_4)_2$ $(J_1, J_2) \simeq (-2, 6.5)$ K, whereas for $SrZnVO(PO_4)_2$ $(J_1, J_2) \simeq (-4, 5.5)$ K. Thus the NNN AF exchange is comparable to, and even stronger than, the NN FM exchange. One can see that in such a case, the ground state will indeed be the CAF - as measured - and not the more

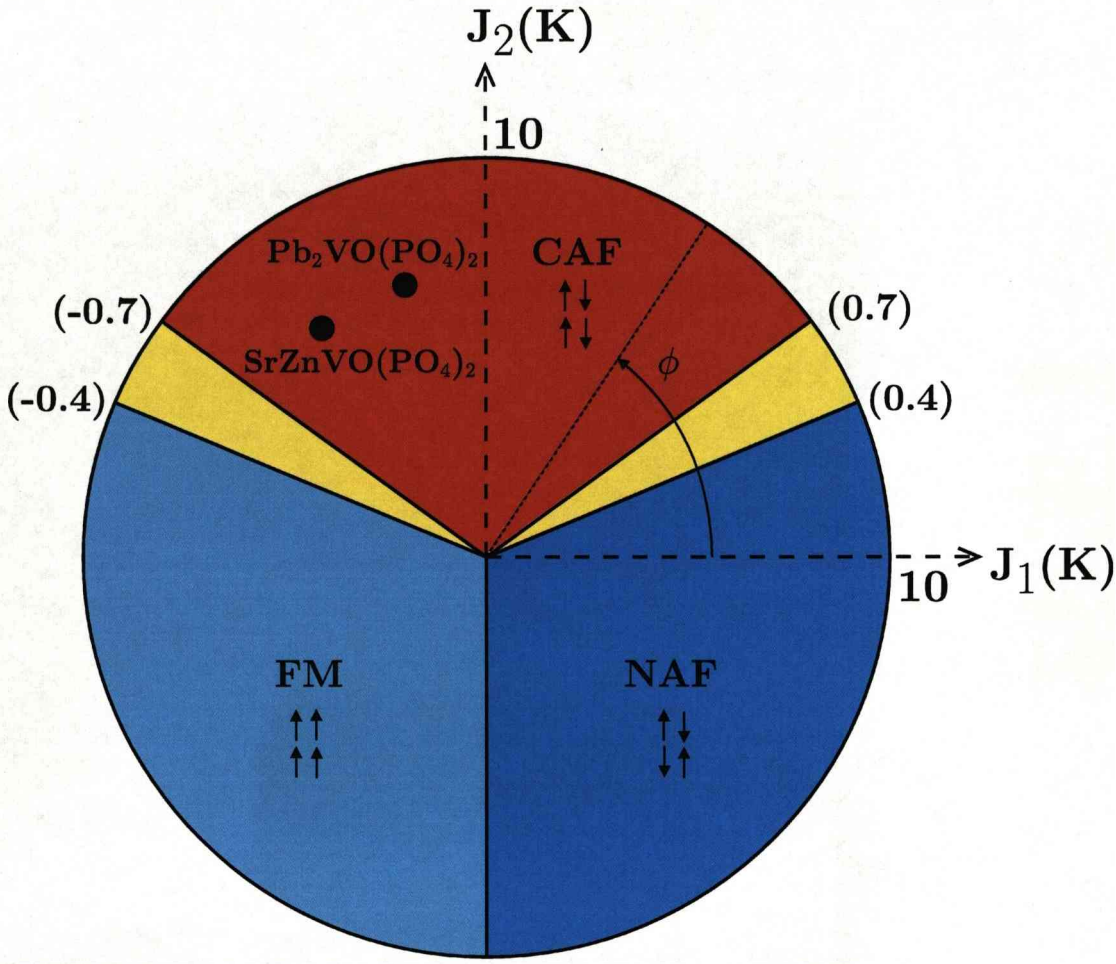

Figure 6.1: Phase diagram for the general $J_1 - J_2$ model of square lattices [74], locating $Pb_2VO(PO_4)_2$ and $SrZnVO(PO_4)_2$. The latter is closer to the yellow theoretically predicted spin-liquid regime.

usual NAF characteristic of systems dominated by AF NN exchange.

We are investigating a new region of the phase diagram for the square-lattice AF, with FM NN interactions and AF NNN interactions. The measured compounds $Pb_2VO(PO_4)_2$ and $SrZnVO(PO_4)_2$ are shown within the $J_1 - J_2$ phase diagram of fig. 6.1, where one can see that they approach a quantum disordered spin-liquid region.

An obvious extension of this work would be to study large single crystals of

$Pb_2VO(PO_4)_2$ and $SrZnVO(PO_4)_2$, using inelastic neutron scattering. The measured spinwave dispersions would give further information on the exhange, and the proximity of the quantum disordered region may lead to novel excitations. Some theoretical predictions with regards to this have already been made [74]. It would, of course, be possible to get more from the spin correlations in the paramagnetic phase with single-crystal samples. Short-range spin correlation in the paramagnetic region have been calculated for both single crystal and polycrystalline materials using HTSE and are contrasted in fig. 6.2. In part (a) we assume only nearest-neighbour interactions ($J_1 = -2$ K), while in part (b) we have included next-nearest neighbour interactions ($J_1 = -2$ K and $J_2 = 6.5$ K, values taken from $Pb_2VO(PO_4)_2$). It is clear from powder averaged calculations (shown on the right) that we have some sensitivity in extracting J_1 and J_2. However, information in $\boldsymbol{Q}$ is lost, as shown in the single crystal calculations on the left of the figure. These more detailed experiments would yield more accurate results for the properties of these novel quantum magnets and would provide theorists with further input in exploring this new area.

The single-crystal experiments would apply for Li_2VOSiO_4, the most theoretically studied case due to the *order-by-disorder* phenomenon. At the limit of $J_1 \to 0$, there are two decoupled Néel sublattices, which may be rotated continuously. The CAF order is believed to be selected because the energy gain due to quantum fluctuations is maximised when the two sublattices are parallel. Experiments, requiring non-absorbing Li isotopes, can give insights to theorists on establishing the exact nature of the mechanism.

The coexistence of quantum fluctuation and frustration may produce a novel ground state in the frustrated region ($\alpha \equiv J_2/J_1 \simeq \pm 0.5$), which is expected to be related to the mechanism of high-temperature superconductivity [71]. Consequently, different ways of tuning systems closer to this quantum disordered phase are sought. The interlayer region between the two-dimensional magnetic square

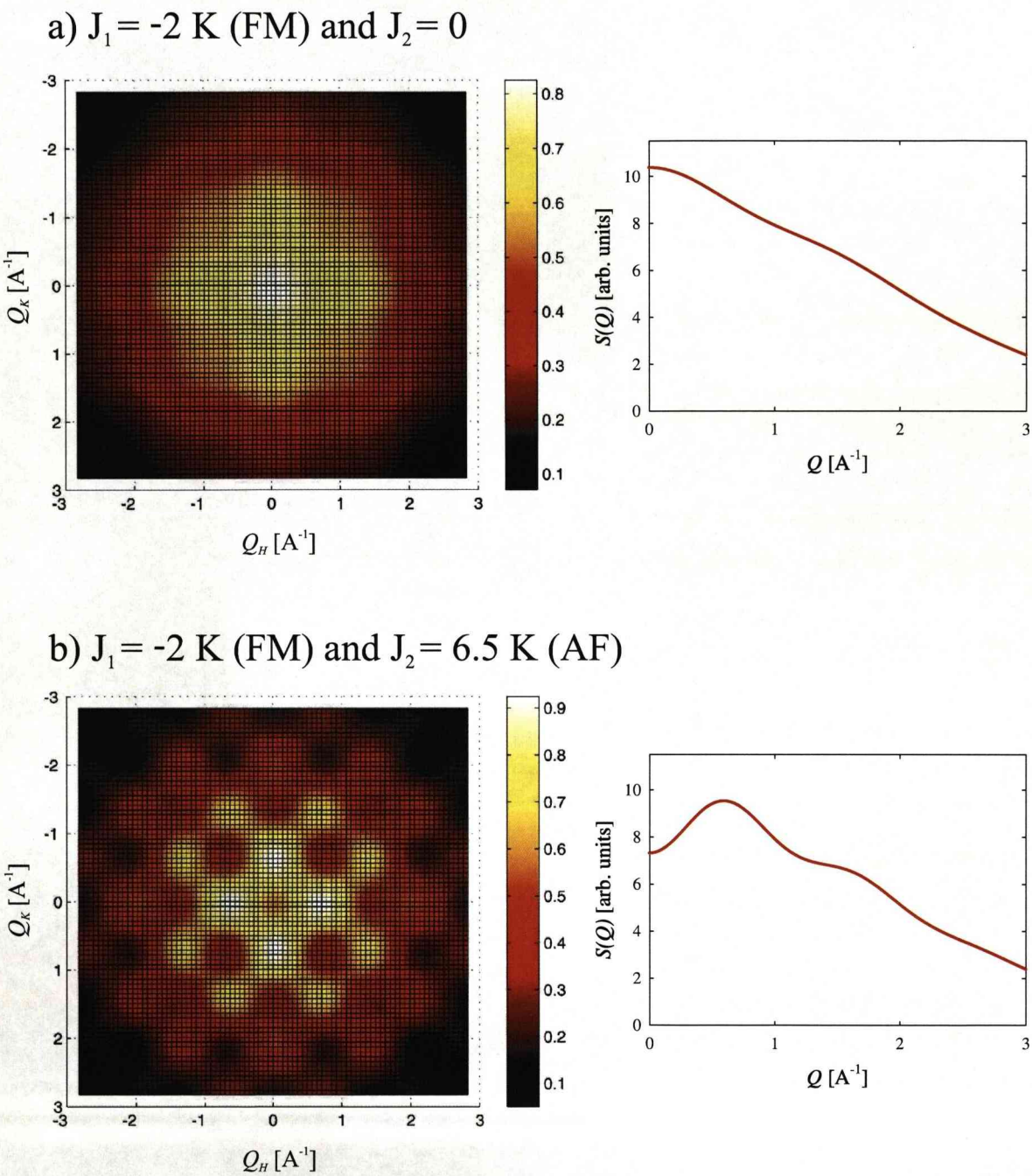

Figure 6.2: Short-range spin correlations of frustrated 2D ferromagnets on the square lattice, calculated at $T = 20$ K. Part (a) is for $J_1 = -2$ K (FM) and part (b) for $J_1 = -2$ K (FM) and $J_2 = 6.5$ K (AF). The left side is for a single crystal, while the right is for a powder where information in $\boldsymbol{Q}$ collapses in one dimension.

lattices affects the structure, and seems to offer a way of tuning these systems to different areas of the J_1-J_2 phase diagram, as seen in fig. 6.1. Pb, Sr and Zn can be substituted for Ba or Cd, giving for instance $BaZnVO(PO_4)_2$ or $BaCdVO(PO_4)_2$. It might also be possible to tune the exchange to be closer to the quantum disordered region by other chemical substitutions. Doping with appropriate elements (such as sulphur) can alter structural and electronic properties, and could be helpful in testing theory. Another parameter that one could try is pressure, which would have an effect on the structure and, in turn, the magnetic properties. Once the zero-field phase is established, one would like to do experiments in an applied magnetic field [160]. This would be especially suited to these low energy systems.

6.2 Transition metal oxides with spin and orbital degrees of freedom

The $GdVO_3$ and $LuVO_3$ single crystals studied here are Mott insulators described by the Hubbard model. Different aspects of their physics were investigated, however this does not exclude the possibility that properties measured on one can be found on the other (especially since they both have a C-type magnetic phase).

Combined neutron diffraction and resonant x-ray scattering techniques for $GdVO_3$ yielded C-type magnetic and G-type orbitally ordered structures, in accordance with the standard Goodenough-Kanamori rules [126]. Particularly for the RXS experiment, we were able to model the XANES spectrum, energy lineshapes and azimuthal dependencies with *ab initio* simulations from the $FDMNES$ package [11]. These theoretical calculations gave us the option to control parameters, and allowed us to conclude that the transitions involved are almost exclusively of dipolar nature (including the pre-edge feature). Hence, $1s \rightleftharpoons 4p$ resonant transitions give rise to large Bragg peaks at forbidden reflections, associated with orbital order. The resonant intensity is proportional to the orbital order parameter Δ

squared, hence one measures the appropriate correlation function on resonance. For our system, the splitting Δ is caused by coherent Jahn-Teller distortions. It is interesting to note here that the *FDMNES* RXS calculations are extremely sensitive to the local environment around the V ions (i.e. the V-O bond lengths) and not so much to the precise C-AF structure (i.e. do not crucially depend on moment direction etc.). Furthermore, we emphasise the combination of a resonant energy spectrum and its theoretical calculation in such experiments, rather than simply relying on the azimuthal dependence. The reason for that is that orbital ordering seems to be a more subtle effect compared to say magnetic ordering (which can usually be straight-forwardly backed up by neutron measurements).

The other $R\mathrm{VO_3}$ perovskite studied is $\mathrm{LuVO_3}$, which has a C-AF structure in the temperature range 84 K $< T <$ 107 K (intermediate temperature phase) and a G-AF structure below that (low temperature phase). Spinwave dispersions were measured in both regimes, which are energetically close according to theoretical calculations [155]. In the C-AF exotic phase, two magnon branches appear, with a gap between them. This is not a classically expected result for a three-dimensional system. Indeed, in order to fit these branches, one needs a spin-orbital model [1, 108, 120, 152] in which quasi-one-dimensional orbital chains appear. An additional *orbital Peierls* dimerisation of these chains can account for the observed gap between the two magnon modes. The values of the exchange and gap parameters in both phases of $\mathrm{LuVO_3}$ can possibly help refine the existing theory. In the low temperature phase we deduced $(J_{ab}, J_c) \simeq (6.32, 4.02)$ meV while in the intermediate exotic regime we found $(J_{ab}, J_c) \simeq (2.5, -1.7)$ meV and a gap $\delta_s \sim 0.15$. This picture contradicts the classical Goodenough-Kanamori rules with static spin and orbitally ordered structures. Here, quantum fluctuations in the orbital sector have important consequences on spin interactions, and these in turn are reflected in spinwave dispersions. In other words, both spin and orbital degrees of freedom need to be taken into account.

The similarities of RXS $GdVO_3$ results and inelastic $LuVO_3$ measurements with the more extensively studied YVO_3 compound [35,151] point to the direction of more comprehensive measurements for the former oxides. It would be interesting to see if spinwave dispersions in the C-AF phase of $GdVO_3$ will indeed reveal a dimerised orbital structure. In that case orbital fluctuations will be part of the model, like in $LuVO_3$ and YVO_3, and the orbitals will not be rigid. This information is not accessible (at the moment) with x-rays. The orbital dimerisation can in principle show up in the crystal structure of all of these compounds, although it has never been possible to detect any signs of it. A very high resolution x-ray scattering experiment could perhaps give some indications and justifications to both theorists and experimentalists. A natural thing to do, from an experimental point of view, would of course be to try and measure magnons in $GdVO_3$ below 8 K, where the Gd ions order. In this low temperature phase, SQUID measurements reveal unique magnetic phase transitions and memory effects for $GdVO_3$ [125] among all other RVO_3 compounds. Neutron field-dependent experiments in this phase are already under way. Resonant x-ray scattering under magnetic field would involve a complicated setup, but one could try it in the future. The reverse ideas apply to $LuVO_3$. It would be crucial to fully characterise its exact structural and magnetic transitions in a diffraction experiment. Following that, an RXS experiment could give information on the orbital ordering/fluctuations of this system in both phases. The exact structural/magnetic refinement results would form the input to the *FDMNES* package, calculating the XANES and RXS spectra, as well as the azimuthal dependencies. The fact that RXS gives very strong intensities means that, in addition to investigating the orbital parameter, one could also look at critical fluctuations just above the phase transition. This might give an insight in what is driving phase transitions. As already noted, the energy difference between G- and C- type spin orderings is very small, therefore they can interchange upon small perturbations. For instance, pressure may

reduce the $GdFeO_3$ distortions and hence trigger the first-order phase transition from G to C-AF SO. Injection of charge carriers is yet another possibility, where one expects the C-AF phase to be energetically favourable again. Charge carriers strongly favour the spin-C phase, as they can freely move along the ferromagnetic spin chains in the c direction, while a hole-motion is frustrated in the spin-G phase in all three directions [108]. The "fine" phase-selection of these strongly correlated electron systems by small changes in temperature, distortions, doping, pressure and magnetic fields is a consequence of the different interactions and degrees of freedom that are inevitably in competition.

Ideally one should study the orbital waves directly. It may be possible in the future to perform inelastic x-ray scattering studies of orbital dispersions. X-ray spectrometers at synchrotrons already have sufficient energy resolution. A key ingredient will again be the need to compare directly with theory.

Appendix A

FDMNES calculations

A number of spectroscopies are related to the transition process of a core electron to some upper empty level. The success of such spectroscopies is due to the fact that the photoelectron is an efficient localised probe around a specific atom. Due to the final state selection rules, these spectroscopies selectively probe the empty valence states allowing analysis of electronic as well as crystallographic structures. In particular, spectroscopies near an ionisation edge are important because it is at these energies that the signal is very sensitive to the three-dimensional crystallographic, electronic and magnetic structures [11].

The *FDMNES* program is a first-principles method of calculating spectra of different spectroscopies related to the real or virtual absorption of x-rays in materials. This sophisticated software has been developed by Yves Joly at CNRS, Grenoble during the past 10 years. It gives the absorption cross sections of photons around the ionisation edge (extending up to around 50 eV above the threshold), that is in the energy range of XANES (X-ray Absorption Near-Edge Structure) in the EXAFS (Extended X-ray Absorption Fine Structure). Calculations can be performed with linear ($\sigma - \sigma$ and $\sigma - \pi$) or circular photon polarisations. At the same time, it can calculate structure factors and intensities of the anomalous or resonant diffraction spectra DAFS, DANES and RXS (Diffraction Anomalous

Fine Structure, Diffraction Anomalous Near-Edge Structure and Resonant X-ray Scattering). *FDMNES* also allows the comparison of the simulated spectra to experimental data with the help of objective criteria [143].

This code, starting from the atomic positions and an associated electronic density, solves the Schrödinger equation to determine the intermediate states probed by the photoelectron. The resulting structure factors can be evaluated by taking into account the different excitation-deexcitation channels in the crystal, including dipole and/or quadrupole transitions. *FDMNES* uses two techniques of mono-electronic calculations. The first one is based on the Green formalism (multiple scattering) on a muffin-tin potential. The important approximation employed here is a spherical averaging of the potential needed for the expansion of the wave functions. The second technique uses the Finite Difference Method (FDM) to solve Schrödinger's equation using the local density approximation. In that way, the shape of the potential is free and in particular the muffin-tin approximation is avoided. This approach can be more precise but is slower, since FDM requires significant computing power. The program is partially symmetrised, with automatically calculated symmetry operations [11, 143].

Let us now describe some practical aspects of running the program and particularly creating an 'indata' file for calculating general absorption and RXS spectra. The general trend of *FDMNES* is writing a "*keyword*" and directly below it specify a value (or values) for it.

An electronic configuration is used by default for all atoms. That can be modified under the keyword "*atom*", where atoms are identified by their atomic numbers. Every input line of an electronic configuration under "*atom*" is automatically indexed by an integer number, starting from 1 (the "atom type number"). Under "*crystal*" one inputs the lattice constants & angles (in Å & degrees) and unit cell fractional coordinates of all atoms. The magnetic structure (if any) can be entered here too by simply typing a '+' or '−' in front of the line with the

fractional coordinates of an atom, suggesting a spin 'up' or 'down' configuration. Directly after this sign one must put the "atom type number". By default, the calculated spectra correspond to the sum of the scattering produced by all the atoms with the same atomic number as the first one in the list under "*crystal*". For example, in the case of a vanadate with the V $3d^2 4s^2$ configuration one has:

```
Atom
   23   2   3 2 2.0 0.0   4 0 1.0 1.0
Crystal
   1.9  1.9  1.9     90.  90.  90.
   -1   0.0  0.5  0.0
```

where 23 is the atomic number of V (and it is taken as atom type number '1' by the software) and 2 signifies the number of valence orbitals (n, l, up population, down population). In this example we have 2 up $3d$ electrons and a $4s$ orbital with 1 up and 1 down electron. The hypothetical crystal is cubic with a lattice constant of 1.9 Å, and the vanadium atom here has a spin down (due to the minus sign; the 1 is the atom type number) and fractional coordinates (0 1/2 0).

The final states are calculated inside a sphere (cluster), whose radius is defined with the keyword "*radius*", with typical values ranging between 3 and 7 Å.

The energy range (keyword "*range*") is -5 to 60 eV with a 0.5 eV step by default. That can be changed by the user, even with a variable step size. The zero is set arbitrarily by the software with no real physical meaning. However, it turns out that in most cases the Fermi level E_F (specified by "*Efermi*") is around -5 eV. That can be checked by a calculation of the density of states (d.o.s., keyword "*Density*"). To get E_F one needs to look at the integrated d.o.s. of the total spin up+spin down sum. E_F corresponds to the energy at which this d.o.s. integral equals to the total number of electrons in the outer shell of the absorbing atom.

For employing the multiple scattering mode, the keyword "*green*" can be used. Then the potential is automatically a muffin-tin one, with much faster calculations

than in the finite difference method.

Quadrupole-quadrupole and dipole-quadrupole terms can be calculated by introducing the keyword "*quadrupole*". With "*nondipole*" one can avoid calculating the dipolar-dipolar component, for example in order to investigate the purely quadrupolar signal (since it is usually extremely small).

Resonant scattering of a specific reflection for a particular polarisation and azimuthal angle can be calculated by the keyword "*rxs*". In order to calculate the (011) reflection in $\sigma - \pi$ ($\sigma = 1$ and $\pi = 2$) at 90° type:

```
rxs
  0 1 1   1 2   90
```

Azimuthal scans are calculated by the keyword "*scan*", followed by appropriate input and output filenames. The origin of the azimuth can be chosen by using "*Zero_azim*" and the specific vector one wants in the direct crystal lattice.

In order to have a magnetic calculation one needs the keyword "*spinorbit*" or "*magnetism*" (this does not include spin-orbit interaction) and a magnetic structure in the input file. Note that apart from indicating the spin directions of the magnetic atoms, a non-equal population of up and down electrons within an orbital is required in order to get some magnetism in the crystal. The spin axis is by default along (001) but can be oriented along any direction by "*axe_spin*"

The program runs in two steps: (i) the main calculation of the XANES spectra and RXS/DAFS amplitudes and (ii) their convolution with other parameters (widths, energy shifts...), so that calculations can be compared with actual experiments. For example, one can include a finite energy transition width (broadening of a δ-function related to the lifetime of a decay) with the "*arc*" keyword. This specifies an 'arctangent' shape for the broadening. The above mentioned "*Efermi*" and "*scan*" instructions are also performed in the convolution part, i.e. in the second step of the calculation.

For more information on how to create an input file for a specific experiment,

one can refer to [143], the *FDMNES* User's Guide, which includes much more detail for the expert user.

Bibliography

[1] S. Maekawa, T. Tohyama, S.E. Barnes, S. Ishihara, W. Koshibae and G. Khaliullin. *"Physics of Transition Metal Oxides"*. Springer Series in Solid-State Sciences, vol. 144, (Springer-Verlag, Berlin, 2004).

[2] J. Emsley. *"The Elements"*. Clarendon Press, Oxford, 1989.

[3] G. Khaliullin. "Order from disorder: Quantum spin gap in magnon spectra of $LaTiO_3$". *Phys. Rev. B* **64**, 212405, (2001).

[4] Y. Murakami, H. Kawada, H. Kawata, M. Tanaka, T. Arima, H. Moritomo and Y. Tokura. "Direct Observation of Charge and Orbital Ordering in $La_{0.5}Sr_{1.5}MnO_4$". *Phys. Rev. Lett.* **80**, 1932, (1998).

[5] L. Paolasini, C. Vettier, F. de Bergevin, F. Yakhou, D. Mannix, A. Stunault, W. Neubeck, M. Altarelli, M. Fabrizio, P.A. Metcalf, and J.M. Honig. "Orbital Occupancy Order in V_2O_3: Resonant X-Ray Scattering Results". *Phys. Rev. Lett.* **82**, 4719, (1999).

[6] Y. Murakami, J.P. Hill, D. Gibbs, M. Blume, I. Koyama, M. Tanaka, H. Kawata, T. Arima, Y. Tokura, K. Hirota and Y. Endoh. "Resonant X-Ray Scattering from Orbital Ordering in $LaMnO_3$". *Phys. Rev. Lett.* **81**, 582, (1998).

[7] M.v. Zimmermann, J.P. Hill, D. Gibbs, M. Blume, D. Casa, B. Keimer, Y. Murakami, Y. Tomioka and Y. Tokura. "Interplay between Charge, Orbital, and Magnetic Order in $Pr_{1-x}Ca_xMnO_3$". *Phys. Rev. Lett.* **83**, 4872, (1999).

[8] Y. Joly, S. Di Matteo and C.R. Natoli. "Ab initio simulations of resonant x-ray scattering on the insulating phase of V_2O_3 compared with recent experiments". *Phys. Rev. B* **69**, 224401, (2004).

[9] S. Di Matteo, Y. Joly and C.R. Natoli. "Critical reexamination of the nonreciprocal x-ray gyrotropy in V_2O_3". *Phys. Rev. B* **67**, 195105, (2003).

[10] M. Benfatto, Y. Joly and C.R. Natoli. "Critical Reexamination of the Experimental Evidence of Orbital Ordering in $LaMnO_3$ and $La_{0.5}Sr_{1.5}MnO_4$". *Phys. Rev. Lett.* **83**, 636, (1999).

[11] Y. Joly. "X-ray absorption near-edge structure calculations beyond the muffin-tin approximation". *Phys. Rev. B* **63**, 125120, (2001).

[12] J.M. Carpenter and W.B. Yelon. *"Methods of Experimental Physics (Vol. 23, Part A)"*, chapter 2: Neutron Sources, edited by K. Sköld and D.L. Price. Academic Press, Inc., 1986.

[13] Jens Als-Nielsen and Des McMorrow. *"Elements of Modern X-Ray Physics"*. John Wiley, 2001.

[14] P. Normile. *"Neutron and Resonant X-ray Magnetic Scattering Studies of Single-Crystal $U_{1-x}Pu_xSb$"*. PhD Thesis, Department of Physics, University of Liverpool, 2001.

[15] C. Kittel. *"Introduction to Solid State Physics"*. John Wiley, 1986.

[16] P. Normile. *Private Communication.*

[17] J. Rossat-Mignod. *"Methods of Experimental Physics (Vol. 23, Part C)"*, chapter 19: Magnetic Structures, edited by K. Sköld and D.L. Price. Academic Press, Inc., 1987.

[18] G.L. Squires. *"Introduction to the Theory of Thermal Neutron Scattering"*. Dover Publications, Inc., 1996.

[19] G. Shirane, S.M. Shapiro and J.M. Tranquada. *"Neutron Scattering with a Triple-Axis Spectrometer"*. Cambridge University Press, 2002.

[20] G.E. Bacon. *"Neutron Diffraction"*. Oxford University Press, 1962.

[21] J.P. Goff. *"Neutron Scattering Studies of Fluorite Compounds"*. PhD Thesis, University of Oxford, Oxford, 1992.

[22] P. Böni. *"Polarised Neutrons", in Magnetic Neutron Scattering.* Edited by A. Furrer (World Scientific, 1995).

[23] R. Stewart. *"Polarized Neutrons"*. Oxford Summer School lecture, 2005.

[24] R.M. Moon, T. Riste and W.C. Koehler. "Polarization Analysis of Thermal-Neutron Scattering". *Phys. Rev.* **181**, 920, (2003).

[25] O. Schärpf and H. Capellmann. "The *XYZ*-Difference Method with Polarized Neutrons and the Separation of Coherent, Spin Incoherent, and Magnetic Scattering Cross Sections in a Multidetector". *Phys. Stat. Sol.* **A135**, 359, (1993).

[26] F. Tasset, P.J. Brown, E. Lelièvre-Berna, T. Roberts, S. Pujol, J. Allibon and E. Bourgeat-Lami. "Spherical neutron polarimentry with Cryopad-II". *Physica B* **267-268**, 69, (1999).

[27] C. Brouder. "Angular dependence of x-ray absorption spectra". *J. Phys.: Condens. Matter* **2**, 701, (1990).

[28] D.H. Templeton and L.K. Templeton. "X-ray Dichroism and Polarized Anomalous Scattering of the Uranyl Ion". *Phys. Rev. Lett.* A**38**, 62, (1982).

[29] K. Namikawa, M. Ando, T. Nakajima and H. Kawata. "X-Ray Resonance Magnetic Scattering". *J. Phys. Soc. Jpn.* **54**, 4099, (1985).

[30] Doon Gibbs, D.R. Harshman, E.D. Isaacs, B.B. McWhan, D. Mills and C. Vettier. "Polarization and Resonance Properties of Magnetic X-Ray Scattering in Holmium". *Phys. Rev. Lett.* **61**, 1241, (1988).

[31] J.P. Hannon, G.T. Trammell, M. Blume and Doon Gibbs. "X-Ray Resonance Exchange Scattering". *Phys. Rev. Lett.* **61**, 1245, (1988).

[32] M. Blume and Doon Gibbs. "Polarization dependence of magnetic x-ray scattering". *Phys. Rev. B* **37**, 1779, (1988).

[33] J.P. Hill and D.F. McMorrow. "X-Ray Resonant Exchange Scattering: polarization Dependence and Correlation Functions". *Acta Cryst.* **A52**, 236, (1996).

[34] M. Blume. "Magnetic scattering of x rays". *J. Appl. Phys.* **57**, 3615, (1985).

[35] M. Noguchi, A. Nakazawa, S. Oka, T. Arima, Y. Wakabayashi, H. Nakao and Y. Murakami. "Synchrotron x-ray-diffraction study of orbital ordering in YVO_3". *Phys. Rev. B* **62**, R9271, (2000).

[36] S. Ishihara and S. Maekawa. "Resonant x-ray scattering in manganites: study of the orbital degree of freedom". *Rep. Prog. Phys.* **65**, 561, (2002).

[37] http://www.ill.fr/instruments/.

[38] J.R. Stewart. *"The D7 Manual"*. ILL Report # ILL01ST14T, 2001.

[39] M.E. Gallagher. *"In-situ Synchrotron X-ray Scattering Studies of the Electrode/Electrolyte Interface"*. PhD Thesis, Department of Physics, University of Liverpool, 2005.

[40] S.D. Brown, L. Bouchenoire, D. Bowyer, J. Kervin, D. Laundy, M.J. Longfield, D. Mannix, D.F. Paul, A. Stunault, P. Thompson, M.J. Cooper, C.A. Lucas and W.G. Stirling. "The XMaS beamline at ESRF: instru-mental developments and high resolution diffraction studies". *J. Synch. Rad.* **8**, 1172, (2001).

[41] P. Millet and C. Satto. "Synthesis and structures of the layered vanadyl(IV) silico-germanates $Li_2VO(Si_{1-x}Ge_x)O_4$ (x = 0, 0.5, 1)". *Materials Research Bulletin* **33**, 1339, (1998).

[42] R. Melzi, P. Carretta, A. Lascialfari, M. Mambrini, M. Troyer, P. Millet and F. Mila. "$Li_2VO(Si, Ge)O_4$, a prototype of a two-dimensional frustrated quantum Heisenberg antiferromagnet". *Phys. Rev. Lett.* **85**, 1318, (2000).

[43] R. Melzi, S. Aldrovandi, F. Tedoldi, P. Carretta, P. Millet, F. Mila. "Magnetic and thermodynamic properties of Li_2VOSiO_4: a two-dimensional $\mathbf{S} = 1/2$ frustrated antiferromagnet on a square lattice". *Phys. Rev. B* **64**, 024409, (2001).

[44] P. Carretta, R. Melzi, N. Papinutto, F. Mila. "Very-low-frequency excitations in frustrated two-dimensional $\mathbf{S} = 1/2$ Heisenberg antiferromagnets". *Phys. Rev. Lett.* **88**, 047601, (2002).

[45] G. Misguich, B. Bernu, L. Pierre. "Determination of the exchange energies in Li_2VOSiO_4 from a high-temperature series analysis of the square-lattice $J_1 - J_2$ Heisenberg model". *Phys. Rev. B* **68**, 113409, (2003).

[46] H. Rosner, R.R.P. Singh, W.H. Zheng, J. Oitmaa and W.E. Pickett. "High-temperature expansions for the $J_1 - J_2$ Heisenberg models: applications to *ab initio* calculated models for Li_2VOSiO_4 and Li_2VOGeO_4". *Phys. Rev. B* **67**, 014416, (2003).

[47] H. Rosner, R.R.P. Singh, W.H. Zheng, J. Oitmaa, S.-L. Drechsler and W.E. Pickett. "Realization of a large J_2 quasi-2D spin-half Heisenberg system: Li_2VOSiO_4". *Phys. Rev. Lett.* **88**, 186405, (2002).

[48] G. Misguich and C. Lhuillier. *"Frustrated Spin Systems"*. Edited by H.T. Diep (World Scientific, Singapore, 2004).

[49] P.W. Anderson. "Resonating valence bonds: a new kind of insulator?". *Materials Research Bulletin* **8**, 153, (1973), Pergamon Press, Inc.

[50] P.W. Anderson. "The resonating valence bond state in La_2CuO_4 and superconductivity". *Science* **235**, 1196, (1987).

[51] P.W. Anderson, G. Baskaran, Z. Zou and T. Hsu. "Resonating-valence-bond theory of phase transitions and superconductivity in La_2CuO_4-based compounds". *Phys. Rev. Lett.* **58**, 2790, (1987).

[52] E. Manousakis. "The spin-$\frac{1}{2}$ Heisenberg antiferromagnet on a square lattice and its applications to the cuprous oxides". *Rev. Mod. Phys.* **63**, 1, (1991).

[53] J. Villain, R. Bidaux, J.-P. Carton and R. Conte. "Order as an effect of disorder". *J. Physique* **41**, 1263, (1980).

[54] P. Chandra, P. Coleman and A.I. Larkin. "Ising transition in frustrated Heisenberg models". *Phys. Rev. Lett.* **64**, 88, (1990).

[55] E.F. Shender. "Antiferromagnetic garnets with fluctuationally interacting sublattices". *Sov. Phys. JETP* **56(1)**, 178, (1982).

[56] Th. Brückel, C. Paulsen, K. Hinrichs, W. Prandl. "Ordering due to disorder in an antiferromagnet with continuously degenerate Néel ground state: a combined neutron diffraction and magnetization study of $(Fe_xGa_{1-x})_2Ca_3Ge_3O_{12}$". *Z. Phys. B* **97**, 391, (1995).

[57] Th. Brueckel, B. Dorner, A.G. Gukasov, V.P. Plakhty, W. Prandl, E.F. Shender and O.P. Smirnow. "Dynamical interaction of antiferromagnetic subsystems: a neutron scattering study of the spinwave spectrum of the garnet $Fe_2Ca_3(GeO_4)_3$". *Z. Phys. B Condensed Matter* **72**, 477, (1988).

[58] Th. Brückel, B. Dorner, A.G. Gukasov, V.P. Plakhty, W. Prandl, E.F. Shender and O.P. Smirnov. "Dynamical sublattice interaction in the antiferromagnetic garnet $Fe_2Ca_3(GeO_4)_3$ as studied by neutron scattering". *Z. Phys. B* **156 & 157**, 308, (1989).

[59] Christopher L. Henley. "Ordering due to disorder in a frustrated vector antiferromagnet". *Phys. Rev. Lett.* **62**, 2056, (1989).

[60] N.B. Ivanov and P.Ch. Ivanov. "Frustrated two-dimensional quantum Heisenberg antiferromagnet at low temperatures". *Phys. Rev. B* **46**, 8206, (1992).

[61] Valeri N. Kotov, J. Oitmaa, Oleg P. Sushkov and Zheng Weihong. "Low-energy singlet and triplet excitations in the spin-liquid phase of the two-dimensional $J_1 - J_2$ model". *Phys. Rev. B* **60**, 14613, (1999).

[62] M. Mambrini, A. Läuchli, D. Poilblanc and F. Mila. "Plaquette valence-bond crystal in the frustrated Heisenberg quantum antiferromagnet on the square lattice". *Phys. Rev. B* **74**, 144422, (2006).

[63] P. Sindzingre. "Spin-1/2 frustrated antiferromagnet on a spatially anisotropic square lattice: contribution of exact diagonalizations". *Phys. Rev. B* **69**, 094418, (2004).

[64] Martin P. Gelfand. "Series investigations of magnetically disordered ground states in two-dimensional frustrated quantum antiferromagnets". *Phys. Rev. B* **42**, 8206, (1990).

[65] Martin P. Gelfand, Rajiv R.P. Singh and David A. Huse. "Zero-temperature ordering in two-dimensional frustrated quantum Heisenberg antiferromagnets". *Phys. Rev. B* **40**, 10801, (1989).

[66] J. Oitmaa and Zheng Weihong. "Series expansion for the $J_1 - J_2$ Heisenberg antiferromagnet on a square lattice". *Phys. Rev. B* **54**, 3022, (1996).

[67] Rajiv R.P. Singh, Zheng Weihong, C.J. Hamer and J. Oitmaa. "Dimer order with striped correlations in the $J_1 - J_2$ Heisenberg model". *Phys. Rev. B* **60**, 7278, (1999).

[68] N. Read and S. Sachdev. "Large-N expansion for frustrated quantum antiferromagnets". *Phys. Rev. Lett.* **66**, 1773, (1991).

[69] T. Nakamura and N. Hatano. "Quantum Monte Carlo calculation of the $J_1 - J_2$ model". *J. Phys. Soc. Jpn.* **62**, 3062, (1993).

[70] S. Miyazawa and S. Homma. "Monte Carlo calculation of the quantum $J_1 - J_2$ model on the square lattice". *Physics Letters A* **193**, 370, (1994).

[71] Y. Nonomura and M. Suzuki. "Cluster-effective-field study on the ground-state phase diagram of the $J_1 - J_2$ model". *J. Phys. Soc. Jpn.* **63**, 1273, (1994).

[72] Stephen Blundell. *"Magnetism in Condensed Matter"*. Oxford Master Series in Condensed Matter Physics, 2001.

[73] O.P. Sushkov, J. Oitmaa and Zheng Weihong. "Quantum phase transitions in the two-dimensional $J_1 - J_2$ model". *Phys. Rev. B* **63**, 104420, (2001).

[74] N. Shannon, B. Schmidt, K. Penc and P. Thalmeier. "Finite temperature properties and frustrated ferromagnetism in a square lattice Heisenberg model". *Eur. Phys. J. B* **38**, 599, (2004).

[75] N. Shannon, T. Momoi and P. Sindzingre. "Nematic order in square lattice frustrated ferromagnets". *Phys. Rev. Lett.* **96**, 027213, (2006).

[76] E. Kaul. *"Experimental Investigation of New Low-Dimensional Spin Systems in Vanadium Oxides"*. PhD Thesis, Technische Universität Dresden, Dresden, 2005.

[77] MPMS *XL*. Hardware & Software Reference Manuals, Quantum Design.

[78] R.V. Shpanchenko, E.E. Kaul, C. Geibel and E.V. Antipov. "The new lead vanadylphosphate $Pb_2VO(PO_4)_2$". *Acta Cryst. Sec. C, Crystal Structure Communications* **62**, i88, (2006).

[79] J.-K. Kim and M. Troyer. "Low temperature behavior and crossovers of the square lattice quantum Heisenberg antiferromagnet". *Phys. Rev. Lett.* **80**, 2705, (1998).

[80] C. Domb and A.R. Miedema. *"Magnetic Transitions"*. Progress in Low Temperature Physics, vol. 4, edited by C.J. Gorter (North Holland, Amsterdam, 1964).

[81] F.J. Morin. "Oxides which show a metal-to-insulator transition at the Néel temperature". *Phys. Rev. Lett.* **3**, 34, (1959).

[82] S. Minomura and H. Nagasaki. "The effect of pressure on the metal-to-insulator transition in V_2O_4 and V_2O_3". *J. Phys. Soc. Jpn.* **19**, 131, (1964).

[83] K.V.K. Rao, S.V.N. Naidu and L. Iyengar. "Thermal expansion of tetragonal phase of VO_2". *J. Phys. Soc. Jpn.* **23**, 1380, (1967).

[84] M. Marezio, P.D. Dernier, D.B. McWhan and J.P. Remeika. "X-ray diffraction studies of the metal insulator transitions in Ti_4O_7, V_4O_7 and VO_2". *Materials Research Bulletin* **5**, 1015, (1970), Pergamon Press, Inc.

[85] C.J. Hearn. "The c/a ratio of VO_2 crystals with the rutile structure". *Solid State Commun.* **12**, 53, (1973), Pergamon Press.

[86] D. Adler. "Mechanisms for metal-nonmetal transitions in transition metal oxides and sulfides". *Rev. Mod. Phys.* **40**, 714, (1968).

[87] P.J. Brown. *Magnetic Form Factors in "International Tables for Crystallography (Vol. C)"*, page 391. A.J.C. Wilson, ed., 1999.

[88] S. Meyer, B. Mertens and Hk. Müller-Buschbaum. "$SrZnVO(PO_4)_2$ and $BaCdVO(PO_4)_2$: Vanadylphosphates related but not isotypic to the $BaZnVO(PO_4)_2$ type". *Zeitschrift für Naturforschung* **52b**, 985, (1997).

[89] Ramesh Nath. *Private Communication.*

[90] H. Nyman, M. O'Keeffe and J.-O. Bovin. "Sodium Titanium Silicate, Na_2TiSiO_5". *Acta Cryst. Sec. B* **34**, 905, (1978).

[91] A. Ziadi, G. Thiele and B. Elouadi. "The Crystal Structure of Li_2TiSiO_5". *J. Solid State Chem.* **109**, 112, (1994).

[92] A. Bombardi, J. Rodriguez-Carvajal, S. Di Matteo, F. de Bergevin, L. Paolasini, P. Carretta, P. Millet and R. Caciuffo. "Direct Determination of the Magnetic Ground State in the Square Lattice $S = 1/2$ Antiferromagnet Li_2VOSiO_4". *Phys. Rev. Lett.* **93**, 027202, (2004).

[93] B. Bleaney. "Paramagnetic Resonance in the Solid State". *J. Phys. Chem.* **57**, 508, (1953).

[94] J. Owen. "Paramagnetic Resonance Measurements of Exchange Interactions". *J. Appl. Phys. Suppl. to vol.* **32**, 213S, (1961).

[95] B.A. Coles, J.W. Orton and J. Owen. "Antiferromagnetic exchange interactions between Mn^{2+} ions in MgO". *Phys. Rev. Lett.* **4**, 116, (1960).

[96] M.R. Brown, B.A. Coles, J. Owen and R.W.H. Stevenson. "Ferromagnetic exchange interaction between Mn^{2+} ions in Mn,ZnF_2". *Phys. Rev. Lett.* **7**, 246, (1961).

[97] P. Carretta, N. Papinutto, C.B. Azzoni, M.C. Mozzati and E. Pavarini. "Frustration-driven structural distortion in $VOMoO_4$". *Phys. Rev. B* **66**, 094420, (2002).

[98] Ikuyo Shiozaki. "Magnetic property of vanadium-molybdenum oxides". *J. Magn. Magn. Mater.* **177-181**, 261, (1998).

[99] Ikuyo Shiozaki. "One-dimensional magnetism and the phase transition in $VOMoO_4$". *J. Phys.: Condens. Matter* **10**, 9813, (1998).

[100] A. Bombardi, L.C. Chapon, I. Margiolaki, C. Mazzoli, S. Gonthier, F. Duc and P.G. Radaelli. "Magnetic order and lattice anomalies in the $J_1 - J_2$ model system $VOMoO_4$". *Phys. Rev. B* **71**, 220406(R), (2005).

[101] F. Mila. "Quantum Frustrated Magnets: From Theory to Experiments". *Int. J. Mod. Phys. B* **17**, 5021, (2003).

[102] S. Meyer and Hk. Müller-Buschbaum. "Synthese und Kristallstruktur eines Barium-Vanadylphosphats $BaZnVO(PO_4)_2$ mit $[(VO)PO_4]$-Schichten". *Zeitschrift für Naturforschung* **52b**, 367, (1997).

[103] Y. Tokura and N. Nagaosa. "Orbital Physics in Transition-Metal Oxides". *Science* **288**, 462, (2000).

[104] J.B. Goodenough. "Electronic and ionic transport properties and other physical aspects of perovskites". *Rep. Prog. Phys.* **67**, 1915, (2004).

[105] K.I. Kugel' and D.I. Khomskiĭ. "The Jahn-Teller effect and magnetism: transition metal compounds". *Sov. Phys. Usp.* **25**, 231, (1982).

[106] J.B. Goodenough and J.-S. Zhou. "Orbital ordering in orthorhombic perovskites". *J. Mater. Chem.* **17**, 2394, (2007).

[107] Z. Fang and K. Terakura. "Structural distortion and magnetism in transition metal oxides: crucial roles of orbital degrees of freedom". *J. Phys.: Condens. Matter* **14**, 3001, (2002).

[108] Giniyat Khaliullin. "Orbital Order and Fluctuations in Mott Insulators". *Progr. Theor. Phys. Suppl.* **160**, 155, (2005).

[109] H.A. Jahn and E. Teller. "Stability of Polyatomic Molecules in Degenerate Electronic States: I - Orbital Degeneracy". *Proc. R. Soc.* **A161**, 220, (1937).

[110] H.A. Jahn. "Stability of Polyatomic Molecules in Degenerate Electronic States: II - Spin Degeneracy". *Proc. R. Soc.* **A164**, 117, (1938).

[111] J. Kanamori. "Crystal Distortion in Magnetic Compounds". *J. Appl. Phys. Suppl. to vol.* **31**, 14S, (1960).

[112] M.-H. Whangbo and H.-J. Koo. "Orbital interaction analysis of cooperative Jahn-Teller distortion, orbital ordering, spin ordering, and spin exchange interactions in magnetic solids". *Solid State Sciences.* **4**, 335, (2002).

[113] K.I. Kugel' and D.I. Khomskiĭ. "Crystal structure and magnetic properties of substances with orbital degeneracy". *Sov. Phys. JETP* **37**, 725, (1973).

[114] M. Cyrot and C. Lyon-Caen. "Orbital superlattice in the degenerate Hubbard model". *J. Physique* **36**, 253, (1975).

[115] V.L. Pokrovskiĭ and G.V. Uĭmin. "Magnetic configurations due to the orbital angular problem". *Sov. Phys. JETP* **34**, 457, (1972).

[116] L.M. Roth. "Simple Narrow-Band Model of Ferromagnetism Due to Intra-Atomic Exchange". *Phys. Rev.* **149**, 306, (1966).

[117] P. Thalmeier and L.M. Falicov. "Intra-atomic correlation energies in cubic metals with canonical *d* bands". *Phys. Rev. B* **20**, 4637, (1979).

[118] J. Kanamori. "Superexchange interaction and symmetry properties of electron orbitals". *J. Phys. Chem. Solids* **10**, 87, (1959).

[119] S. Miyasaka, Y. Okimoto, M. Iwama and Y. Tokura. "Spin-orbital phase diagram of perovskite-type RVO$_3$ (R=rare-earth ion or Y)". *Phys. Rev. B* **68**, 100406(R), (2003).

[120] G. Khaliullin, P. Horsch and A.M. Oleś. "Spin Order due to Orbital Fluctuations: Cubic Vanadates". *Phys. Rev. Lett.* **86**, 3879, (2001).

[121] P. Bordet, C. Chaillout, M. Marezio, Q. Huang, A. Santoro, S-W. Cheong, H. Takagi, C.S. Oblesby and B. Batlogg. "Structural Aspects of the Crystallographic-Magnetic Transition in LaVO$_3$ around 140 K". *J. Solid State Chem.* **106**, 253, (1993).

[122] A. Muñoz, J.A. Alonso, M.T. Casais, M.J. Martínez-Lope, J.L. Martínez and M.T. Fernández-Díaz. "Thermal Evolution of the Crystallographic and Magnetic Structure in LuVO$_3$: A Neutron Diffraction Study". *Chem. Mater.* **16**, 1544, (2004).

[123] M. Reehuis, C. Ulrich, P. Pattison, B. Ouladdiaf, M.C. Rheinstädter, M. Ohl, L.P. Regnault, M. Miyasaka, Y. Tokura and B. Keimer. "Neutron diffraction study of YVO$_3$, NdVO$_3$ and TbVO$_3$". *Phys. Rev. B* **73**, 094440, (2006).

[124] L.D. Tung, M.R. Lees, G. Balakrishnan and D. McK. Paul. "Magnetization reversal in orthovanadate RVO$_3$ compounds (R=La, Nd, Sm, Gd, Er, and Y): Inhomogeneities caused by defects in the orbital sector of quasi-one-dimensional orbital systems". *Phys. Rev. B* **75**, 104404, (2007).

[125] L.D. Tung. "Tunable temperature-induced magnetization jump in a GdVO$_3$ single crystal". *Phys. Rev. B* **73**, 024428, (2006).

[126] John B. Goodenough. *"Magnetism and the Chemical Bond"*. Interscience Monographs on Chemistry, New York, 1963.

[127] Y. Ren, A.A. Nugroho, A.A. Menovsky, J. Strempfer, U. Rütt, F. Iga, T. Takabatake and C.W. Kimball. "Orbital-ordering-induced phase transition in LaVO$_3$ and CeVO$_3$". *Phys. Rev. B* **67**, 014107, (2003).

[128] N. Shirakawa and M. Ishikawa. "Anomalous diamagnetism of a Perovskite LaVO$_3$". *Jap. J. Appl. Phys.* **30**, L755, (1991).

[129] Y. Ren, T.T.M. Palstra, D.I. Khomskiĭ, E. Pellegrin, A.A. Nugroho, A.A. Menovsky and G.A. Sawatzky. "Temperature-induced magnetization reversal in a YVO$_3$ single crystal". *Nature* **396**, 441, (1998).

[130] Y. Kimishima, Y. Ichiyanagi, K. Shimizu and T. Mizuno. "N-type ferrimagnetism of SmVO$_3$". *J. Magn. Magn. Mater.* **210**, 244, (2000).

[131] H.C. Nguyen and J.B. Goodenough. "Magnetic studies of some orthovanadates". *Phys. Rev. B* **52**, 324, (1995).

[132] J.-Q. Yan, J.-S. Zhou and J.B. Goodenough. "Opposing spin-canting mechanism in single-crystal $LuVO_3$ and YVO_3". *Phys. Rev. B* **72**, 094412, (2005).

[133] http://typo.ill.fr/fileadmin/users_files/Other_Sites/Dif/ccsl/mk4man/manual.html.

[134] G.J. McIntyre and Z. Barnea. "Some consequences of the presence of antisymmetric atomic features in noncentrosymmetric structures". *Acta Cryst.* A**35**, 260, (1979).

[135] T. Chattopadhyay, G.J. McIntyre and U. Köbler. "Antiferromagnetic Phase Transition in GdAg". *Solid State Commun.* **100**, 117, (1996).

[136] J.S. Abell, J.X. Boucherle, R. Osborn, B.D. Rainford and J. Schweizer. "Polarized neutron study of the intermetallic compound $GdAl_2$". *J. Magn. Magn. Mater.* **31-34**, 247, (1983).

[137] J. Pickardt, Th. Schendler und M. Kolm. "X-Ray Structure Analysis of Single Crystals of Ternary Rare Earth Vanadium(III) Oxides $LnVO_3$ (Ln = Gd, Dy, Er)". *Z. anorg. allg. Chem.* **560**, 153, (1988).

[138] S. Ishihara and S. Maekawa. "Theory of Anomalous X-Ray Scattering in Orbital-Ordered Manganites". *Phys. Rev. Lett.* **80**, 3799, (1998).

[139] S. Ishihara and S. Maekawa. "Orbital ordering and resonant x-ray scattering in layered manganites". *Phys. Rev. B* **62**, 5690, (2000).

[140] I.S. Elfimov, V.I. Anisimov and G.A. Sawatzky. "Orbital Ordering, Jahn-Teller Distortion, and Anomalous X-Ray Scattering in Manganates". *Phys. Rev. Lett.* **82**, 4264, (1999).

[141] M. Takahashi, J. Igarashi and Peter Fulde. "Anomalous X-Ray Scattering in $LaMnO_3$". *J. Phys. Soc. Jpn.* **68**, 2530, (1999).

[142] V.E. Dmitrienko, K. Ishida, A. Kirfel and E.N. Ovchinnikova. "Polarization anisotropy of X-ray atomic factors and 'forbidden' resonant reflections". *Acta Cryst.* A**61**, 481, (2005).

[143] Yves Joly. *"FDMNES User's Guide"*. Centre National de la Recherche Scientifique, 2006.

[144] M.v. Zimmermann, C.S. Nelson, J.P. Hill, D. Gibbs, M. Blume, D. Casa, B. Keimer, Y. Murakami, C.-C. Kao, C. Venkataraman, T. Gog, Y. Tomioka, and Y. Tokura. " X-ray resonant scattering studies of orbital and charge ordering in $Pr_{1-x}Ca_xMnO_3$". *Phys. Rev. B* **64**, 195133, (2001).

[145] K.J. Thomas, J.P. Hill, S. Grenier, Y-J. Kim, P. Abbamonte, L. Venema, A. Rusydi, Y. Tomioka, Y. Tokura, D.F. McMorrow, G. Sawatzky and M. van Veenendaal. " Soft X-Ray Resonant Diffraction Study of Magnetic and Orbital Correlations in a Manganite Near Half Doping". *Phys. Rev. Lett.* **92**, 237204, (2004).

[146] S. Grenier, J.P. Hill, D. Gibbs, K.J. Thomas, M.v. Zimmermann, C.S. Nelson, V. Kiryukhin, Y. Tokura, Y. Tomioka, D. Casa, T. Gog, and C. Venkataraman. " Resonant x-ray diffraction of the magnetoresistant perovskite $Pr_{0.6}Ca_{0.4}MnO_3$". *Phys. Rev. B* **69**, 134419, (2004).

[147] M.v. Zimmermann, C.S. Nelson, Y.-J. Kim, J.P. Hill, D. Gibbs, H. Nakao, Y. Wakabayashi, Y. Murakami, Y. Tokura, Y. Tomioka, T. Arima, C.-C. Kao, D. Casa, C. Venkataraman, and Th. Gog. "Resonant x-ray-scattering study of octahedral tilt ordering in $LaMnO_3$ and $Pr_{1-x}Ca_xMnO_3$". *Phys. Rev. B* **64**, 064411, (2001).

[148] S. Grenier, K.J. Thomas, Y.-J. Kim, J.P. Hill, D. Gibbs, V. Kiryukhin, Y. Tokura, Y. Tomioka, D. Casa, T. Gog and C. Venkataraman. "Resonant X-ray scattering as a probe of the valence and magnetic ground state and excitations in $Pr_{0.6}Ca_{0.4}MnO_3$". *Physica B* **345**, 6, (2004).

[149] S. Di Matteo, T. Chatterji, Y. Joly, A. Stunault, J.A. Paixao, R. Suryanarayanan, G. Dhalenne, and A. Revcolevschi. "Resonant x-ray scattering from $LaSr_2Mn_2O_7$ at the Mn K edge". *Phys. Rev. B* **68**, 024414, (2003).

[150] L. Paolasini, S. Di Matteo, C. Vettier, F. de Bergevin, A. Sollier, W. Neubeck, F. Yakhou, P.A. Metcalf, J.M. Honig. "Interplay between orbital and magnetic long range order by resonant X-ray scattering in $(V_{1-x}Cr_x)_2O_3$". *J. Electron Spectrosc. Relat. Phenom.* **120**, 1, (2001).

[151] C. Ulrich, G. Khaliullin, J. Sirker, M. Reehuis, M. Ohl, S. Miyasaka, Y. Tokura and B. Keimer. "Magnetic Neutron Scattering Study of YVO_3: Evidence for an Orbital Peierls State". *Phys. Rev. Lett.* **91**, 257202, (2003).

[152] A.M. Oleś, P. Horsch and G. Khaliullin. "One-dimensional orbital fluctuations and the erotic magnetic properties of YVO_3". *Phys. Rev. B* **75**, 184434, (2007).

[153] J. Sirker and G. Khaliullin. "Entropy driven dimerization in a one-dimensional spin-orbital model". *Phys. Rev. B* **67**, 100408(R), (2003).

[154] L.D. Tung. *SQUID & heat capacity measurements; unpublished neutron data from TriCS, PSI.*

[155] T. Mizokawa, D.I. Khomskii and G.A. Sawatzky. "Interplay between orbital ordering and lattice distortions in $LaMnO_3$, YVO_3, and $YTiO_3$". *Phys. Rev. B* **60**, 7309, (1999).

[156] P. Horsch, G. Khaliullin and A.M. Oleś. "Dimerization versus Orbital-Moment Ordering in a Mott Insulator YVO_3". *Phys. Rev. Lett.* **91**, 257203, (2003).

[157] Y. Motome, H. Seo, Z. Fang and N. Nagaosa. "One-Dimensional Confinement and Enhanced Jahn-Teller Instability in $LaVO_3$". *Phys. Rev. Lett.* **90**, 146602, (2003).

[158] Z. Fang and N. Nagaosa. "Quantum Versus Jahn-Teller Orbital Physics in YVO_3 and $LaVO_3$". *Phys. Rev. Lett.* **93**, 176404, (2004).

[159] S. Miyasaka, Y. Okimoto and Y. Tokura. "Anisotropy of Mott-Hubbard Gap Transitions due to Spin and Orbital Ordering in $LaVO_3$ and YVO_3". *J. Phys. Soc. Jpn.* **71**, 2086, (2002).

[160] B. Schmidt, N. Shannon and P. Thalmeier. "The frustrated $J_1 - J_2$ model in high magnetic fields". *J. Phys.: Condens. Matter* **19**, 145211, (2007).

Index